

Ultrafast Optical and X-ray Absorption Studies of Solvations Dynamics

THÈSE N° 4607 (2010)

PRÉSENTÉE LE 12 FÉVRIER 2010

À LA FACULTÉ SCIENCES DE BASE

LABORATOIRE DE SPECTROSCOPIE ULTRARAPIDE

PROGRAMME DOCTORAL EN PHYSIQUE

ÉCOLE POLYTECHNIQUE FÉDÉRALE DE LAUSANNE

POUR L'OBTENTION DU GRADE DE DOCTEUR ÈS SCIENCES

PAR

Van Thai PHAM

acceptée sur proposition du jury:

Prof. G. Gremaud, président du jury
Prof. M. Chergui, Prof. C. Bressler, directeurs de thèse
Prof. P. D'Angelo, rapporteur
Prof. L. Helm, rapporteur
Prof. A. Laubereau, rapporteur



ÉCOLE POLYTECHNIQUE
FÉDÉRALE DE LAUSANNE

Suisse
2010

Ultrafast Optical and X-ray Absorption Studies of Solvation Dynamics

Ph.D Thesis

Van-Thai Pham

*Laboratoire de Spectroscopie Ultrarapide
Institut des Sciences et Ingénierie Chimiques Faculté des Sciences de Base – EPFL
CH-1015 Dorigny-Lausanne*

Abstract

Solvation dynamics, the process of solvent reorganization upon electronic excitation of a solute, is central to our understanding chemical reactions in liquid phase. Ultrafast optical studies of solvation dynamics have so far been carried out on polyatomic molecules, which have internal degrees of freedom. This property does not allow the unambiguous extraction dynamics of the solvent shell. Because of their atomic character (i.e. lacking internal degrees of freedom) and of their solvent sensitive absorption bands (the so-called CTTS or charge-transfer-to-solvent bands), atomic halides represent ideal systems for the study of electronic solvation dynamics. Although these systems have received detailed attention in femtosecond optical studies, very little has been learned about the response of the caging solvent, which results from the fact that optical tools do not extract structural movement in a direct fashion. In this thesis, we combined ultrafast laser and structure-sensitive X-ray spectroscopies to probe in real-time the formation and decay of a nascent iodine atom created by photodetachment of a valence electron from the parent iodide anion.

Optical pump-probe experiments are used to assess the photoproduct concentrations on time scales ranging from femtoseconds to nanoseconds. We also carried out detailed optical studies employing 1- and multiphoton detachment of the valence $5p$ electron from iodide, and confirmed an ultrafast thermal heating of the entire sample on a ps time scale.

Static L_1 and L_3 -edge X-ray absorption spectra of aqueous iodide have been recorded and analysed in terms of simulations based on classical, quantum mechanical molecular mechanics (QMMM) and density functional theory (DFT) molecular dynamics. QMMM yields the solvent shell structure that best fits the EXAFS spectrum. Picosecond X-ray absorption near edge structure (XANES) spectra were recorded from 50 ps up to several tens of nanoseconds. They were analyzed with respect to the different photoproducts observed on these time scales, delivering for the first time new spectra for the intermediate reaction products, I^0 and I_2^- . By analyzing the transient extended x-ray absorption fine structure (EXAFS) data of the iodine atoms, we derived a dramatic expansion of ~ 0.6 Å of the solvent shell with respect to that of iodide.

Femtosecond XANES studies reveal an increase in the binding energies of the $5p$ and $2s$, with respect to those at 50 ps. An increase in the $2s \rightarrow 5p$ transition probability is consistent with the increase of the ionization energy of $2s$ electron of iodine atom at 300 fs, as compared to 50 ps. The $2s \rightarrow 5p$ transition probability is found to decrease by ~ 1.1 times from 300 fs to 50 ps.

Keywords: X-ray Absorption Spectroscopy, XAS, EXAFS, XANES, Solvation Dynamics, Aqueous Iodide, Femtosecond X-ray, Synchrotron Radiation, Femtosecond Laser, Pump-Probe Experiment, CTTS, Solvated Electron.

Étude de la dynamique de solvation par absorption ultrarapide optique et de rayons X

Thèse de Doctorat

Van-Thai Pham

*Laboratoire de Spectroscopie Ultrarapide
Institut des Sciences et Ingénierie Chimiques Faculté des Sciences de Base – EPFL*

CH-1015 Dorigny-Lausanne

Résumé

La dynamique de solvation est le processus de réorganisation du solvant suite à une excitation électronique du soluté, et est un phénomène crucial pour la description des réactions chimiques en phase liquide. Jusqu'à ce jour, les études de solvation dynamique ont été effectuées par des méthodes optiques sur des molécules polyatomiques, qui contiennent des degrés de liberté internes. De plus, ces études ne permettent pas d'obtenir la structure de la couche de solvation. Compte tenu de leur nature atomique (sans degrés internes de liberté) et de leur bandes d'absorption très sensible à la nature du solvant (les bandes CTTS, ou charge-transfer-to-solvent bands), les halogénures sont des candidats idéaux pour les études de solvation dynamique. Dans cette thèse, nous combinons des méthodes de spectroscopie ultrarapide dans le domaine optique et X pour suivre en temps réel la formation et le déclin des atomes d'iode générés par photo détachement de l'électron suite à l'excitation des bandes CTTS.

Les spectres statiques aux seuils L_1 and L_3 de l'ion I^- aqueux ont été et analysés en fonction de simulations basées sur la dynamique moléculaire classique, par méthodes hybrides quantique/classique (quantum mechanics/molecular mechanics, QM/MM), et purement quantique (density functional theory, DFT). La couche de solvation obtenues à partir des simulations QMMM reproduit au mieux le spectres EXAFS au seuil L_3 . Les spectres

d'absorption XANES picoseconde ont été obtenus entre 50 ps et plusieurs dizaines de nanosecondes. Ils ont été analysés de manière consistante en fonction des différents photo produits attendus sur ces échelles de temps, en particulier, I^0 and I_2 . Ces spectres nous permettent d'analyser les spectres EXAFS au seuil L_3 et d'en extraire la structure de la couche de solvation autour de l'atome I^0 , laquelle couche a un rayon augmenté de ~ 0.6 Å comparé à celui de l'iodure.

Des mesures XANES femtoseconde ont aussi été effectuées et montrent une augmentation, entre 300 fs et 50 ps, de l'énergie de liaison des orbitales $5p$ et $2s$ ainsi que de la probabilité de transition $2s \rightarrow 5p$. Ceci est en accord avec le changement de la section efficace obtenue sur les traces cinétiques.

Mot-Clés : Spectroscopie d'Absorption X, XAS, EXAFS, XANES, Dynamique Solvation, Iodure aqueuse, Femtosecond rayons X, Synchrotron Radiation, Femtosecond Laser, Expérience Pump-Sonde, CTTS, Electron Solvate.

Contents

Chapter 1 Introduction.....	1
1.1 Motivation.....	1
1.2 Charge transfer to solvent states and photodetachment mechanism	1
1.3 The solvent shell of aqueous iodide	5
1.4 Outline.....	9
Chapter 2 X-ray Absorption Spectroscopy Theory	11
2.1 Introduction to X-ray Absorption Spectroscopy	11
2.1.1 XANES spectrum.....	14
2.1.2 EXAFS spectrum	17
2.1.3 EXAFS analysis for liquid	21
2.2 Basic Principles of Multiple Scattering Theory.....	24
2.2.1 Understanding XAS Phenomenon within MS Theory	24
2.3 Conclusions	27
Chapter 3 Experimental Method.....	30
3.1 Synchrotron Radiation Source	30
3.2 Bend Magnet and Undulator Radiation.	33
3.2.1 Bend Magnet.....	33
3.2.2 Undulator and wiggler radiation	36
3.3 Temporal Structure of Synchrotron Radiation.....	39
3.4 Static XAS measurement and microXAS beamline flux curve.....	43
3.5 Femtosecond x-ray generation using the synchrotron-based laser-electron slicing technique	47
3.5.1 Laser system.....	49
3.5.2 Insertion devices: modulator and radiator	50
3.6 Picosecond- resolved XAS setup	54
3.7 Femtosecond-resolved X-ray Absorption	57
3.8 Femtosecond All Optical Pump-Probe Setup.....	61
3.8.1 400 nm pump white light continuum and 800 nm probe.....	61
3.8.2 400 nm pump 211 nm probe	64
3.8.3 400 nm pump 240 nm probe	64
3.8.4 240 nm pump 800 nm probe	64
Chapter 4 Structural Analysis of Iodide Static Solvation Shell	67

4.1 Data reduction	67
4.2 Refinement of radial distribution function	68
4.3 Results and discussion	70
4.4 Conclusions	72
Chapter 5 Femtosecond Optical Transient Absorption of aqueous iodide.....	89
5.1 Introduction	89
5.2 Single photon excitation	90
5.3 Multiphoton excitation	101
5.3.1 Ultrafast kinetics of electron generated by multiphoton excitation in water	101
5.3.2 Ultrafast kinetics of electron generated by multiphoton excitation in aqueous iodide	102
5.3.3 Transient bleach of aqueous iodide	106
5.4 Conclusions	112
Chapter 6 Picosecond-resolved x-ray absorption spectroscopy	114
6.1 Introduction	114
6.2 Electronic properties	114
6.2.1 Transient XANES around the Iodine L_1 edge	114
6.2.2 Simple fit procedure for determining the XANES of atomic iodine	120
6.2.3 Fitting the temporal evolution of the Iodine L_1 pre-edge peak	122
6.2.4 Kinetics of the photoproducts	129
6.3 Transient Structure of Aqueous Iodine Atoms	131
6.4 Conclusions	137
Chapter 7 Femtosecond XANES study of aqueous iodide.....	138
7.1 Introduction	138
7.2 Iodine XANES spectrum	138
7.3 Conclusions	143
Chapter 8 Conclusions and Outlook.....	145
8.1 Conclusions	145
8.2 Outlooks	146
Appendix A Determination for uncertainties of the parameters of iodide static solvation shell	148
Appendix B Determination for uncertainties of iodine solvation shell at 50 ps.....	154
Acknowledgements.....	156

Curriculum vitae.....	158
Bibliography.....	166

Chapter 1 Introduction

1.1 Motivation

Most chemical and biological reactions occur in liquids (e.g., in water). Since the discovery of the so called “cage effect” by Franck and Rabinowitch^{1,2} the interaction of molecules in condensed phase environments have stimulated numerous studies, aiming at elucidating the different behavior they exhibit in such media. The basic idea behind the cage effect is that molecules undergo different reaction pathways than the same molecules when isolated in the gas phase. The text book example for the cage effect concerns the hampered dissociation of a diatomic molecule undergoing a simple photodissociation reaction, which would readily separate in the gas phase. This triggered many studies aiming to understand the reactivity of chemicals in condensed phases.

Among these, knowledge of the solvation dynamics is at the core for our understanding of chemical reactivity. However, it is inherently difficult to distinguish between solvation dynamic processes and e.g. internal vibrational relaxation (IVR) of the reacting molecule. Aqueous halides represent ideal candidates for this purpose due to their lack of internal degrees of freedom. These systems are subject to photoexcited electronic charge-transfer-to-solvent (CTTS) states, which are accompanied by the reorganization of solvent in the complete absence of IVR processes.

In this thesis, we combine ultrafast laser studies with X-ray spectroscopic experiments on the picoseconds and femtosecond time scale to trace the formation and decay of nascent iodine atoms, along with the transient structure of the caging solvent molecules following impulsive photodetachment of an electron from reactant iodide ions.

1.2 Charge transfer to solvent states and photodetachment mechanism

The absorption spectrum of anions in solutions is characterized by the so-called charge-transfer-to-solvent (CTTS) bands, which is absent in the isolated gas phase ion. The CTTS states are regarded as bound, delocalized states of the electron, centered around the atom, and

stabilized by the overall pre-existing solvent polarization to the ground state ion^{3,4}. The CTTS band of aqueous iodide appears as two bands in UV range (Fig. 1.1). The bands are assigned to two different spin-orbit states of the neutral iodine core $I(^2P_{3/2})$ and $I(^2P_{1/2})$, both final states in the optical transitions have a diffuse CTTS electron. The first band is centered at 5.5 eV while the second is blue-shifted by 0.94 eV, the spin-orbit splitting energy⁵. The smaller halide anions such as Br^- , Cl^- have the CTTS bands in the deeper UV. It was found that the CTTS bands exhibit a red-shift as the solvent temperature increases. In bulk solution, the hydration of the ground state iodide leads to strong stabilization. For cluster, experiment⁶ and theory⁷ show that the vertical binding energy of the iodide cluster $I(H_2O)_n$ rapidly increases as n is increased, eg. 3.1, 5.1 and 6.6 eV for $n=0$, 6, and 60, respectively. The CTTS absorption bands are considerably lower than the

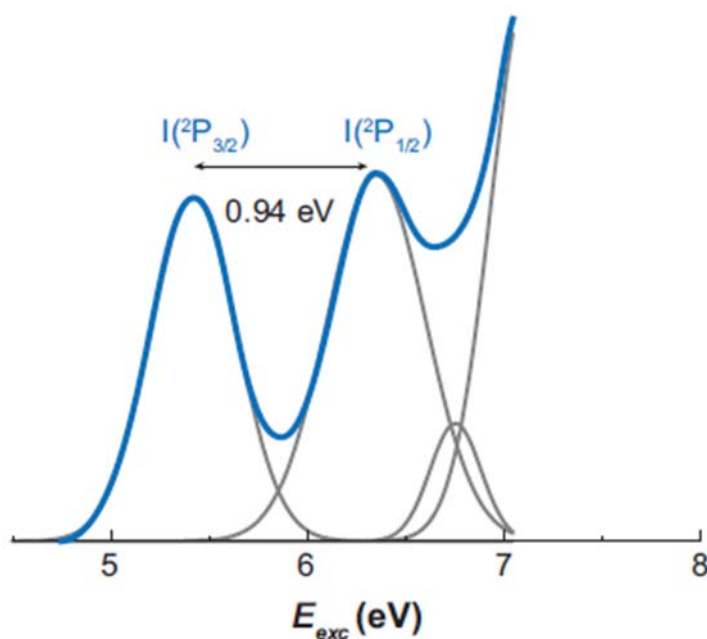


Fig. 1.1: Aqueous iodide absorption spectrum (blue curve). The gray lines show individual CTTS bands decomposed by log-normal analysis⁵. The first two bands correspond to two different spin-orbit states of the neutral iodine core (see text). Source: ¹²³

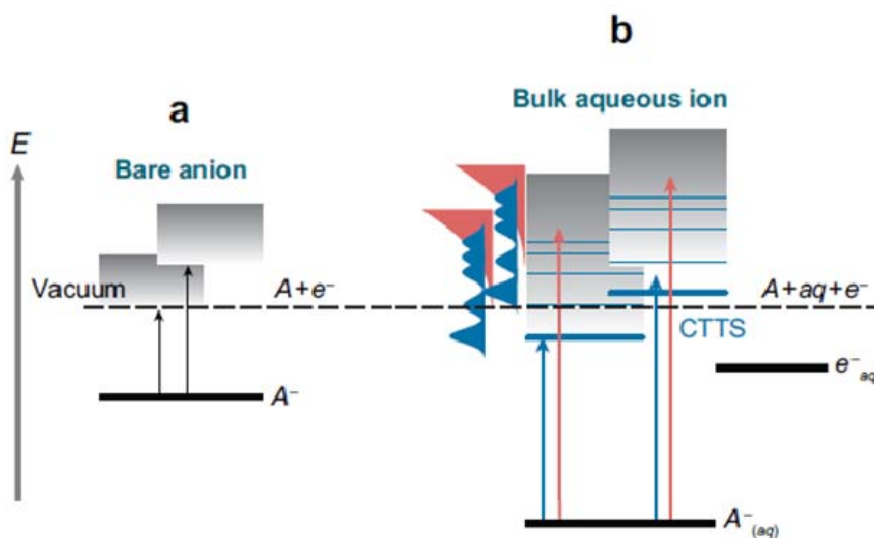


Fig. 1.2: Energy diagram for a halide anion in the gas (a) and aqueous phase (b). In both cases, the two continua correspond to two different final states of the detached iodide. CTTS transitions (blue) contribute discrete (though broad) bands to the electronic absorption spectrum of the aqueous halide. Direct transition into the water conduction band occurs at higher energy (red). Source: ¹²³.

vertical energy to reach the water conduction band which is 7.7 eV for $I^-(aq)$ ^{8,9} (red arrows in Fig. 1.2b).

The CTTS states are the doorway states to electron detachment. Because iodide has the lowest lying CTTS states among halide anions, it has been one of the most studied systems. First principles simulations by Rossky and coworkers ¹⁰, based on non-adiabatic quantum dynamics of a one-electron system with classical molecular dynamics for the solvent molecules showed that the CTTS absorption bands are a complex structure of several overlapping sub-bands, with an overall line shape resulting from the interplay between the separate response of each sub-band to the field exerted by the solvent surrounding the ionic cavity ¹⁰. Thus each electronic state is in principle characterized upon excitation by a specific angular distribution, which may influence the fate of the nascent electron in a different way. Indeed, in their work Rossky and co-workers also investigated the dynamical evolution of CTTS states and predicted the transient absorption and emission spectra which would result from such changes. Their simulations predicted two channels for the formation of the solvated electron after population of a high-lying CTTS-state of the iodide: a direct non-adiabatic electron separation (within 50

fs) and a delayed detachment of the electron after fast relaxation within the CTTS manifold to the lowest state (time constant of 450 fs) and subsequent adiabatic separation of the electron from iodine. A complex was predicted consisting of a water molecule between the detached electron and the parent atom. The structure displays the spectral features similar to that of a hydrated electron since the first solvation shell of the charge is solely occupied by water molecules. Geminate recombination of the complex was predicted to occur within a few picoseconds, whereas the release of the electron appeared to be unlikely in the computations. This result, however, is not consistent with the large yield observed experimentally of the photogenerated solvated electrons^{11,12}. These simulations were motivated by earlier experimental studies of Eisinger *et al*¹³ on electron photodetachment by multiphoton excitation of aqueous iodide at 312 nm, with detection of the aqueous electron in the 0.6 to 1 μm region¹³. Under such conditions, the nature of the initially accessed states is unclear, and it was concluded that the observed electrons came mostly from three-photon excitation of iodide into the continuum, thus bearing little relevance to the lower CTTS states. The most detailed studies of electron photodetachment of aqueous iodide were carried out by Bradforth and co-workers^{14,15,16} at room temperature, upon one-photon excitation on the low energy side of the CTTS band at 255 nm. The observed geminate recombination and electron escape dynamics on the picosecond time scale were analyzed using two different models, a diffusion-limited return of the electron from ~ 15 Å to its parent and a competing kinetics model. They concluded that the “ejected” electron in the halide detachment is merely separated from the halogen atom within the same solvent shell. The assignment of detachment into a contact pair is based on the temporal recombination profile and not supported by any new spectral absorption feature, which could identify such an electron in a contact pair. Based on their model a formation time of the hydrated iodine:electron pair within 200 fs was concluded¹⁴. The complex is expected to subsequently recombine with a time constant of 33 ps or dissociate with a time constant of 70 ps. The hypothesis of a contact pair was proposed by Staib and Borgis in their simulation of aqueous chloride excited to their CTTS states^{17,18}. Laubereau *et al* investigated the temperature dependence of the photodetachment dynamics upon 242 nm excitation detecting the solvated electron in the 0.5 to 1 μm spectral region¹⁹. They reported a first intermediate on a time scale of 180-220 fs, which they attributed to an electron-iodine pair in a transient solvent configuration, followed by a second time scale of 540-700 fs which they attributed to a solvent

reorganization leading to a quasi-equilibrated electron-iodine pair. Note that femtosecond experiments probing the dynamics of the dipole bound states of iodide in water clusters of varying sizes ²⁰ found that the electron is rapidly separated from the iodine atom and subsequently undergoes energy relaxation. The picture used to describe the process in water cluster is cast in terms of an isomerization of the water cluster to accommodate the nascent electron.

The above studies by Bradforth *et al* and Laubereau *et al* were all carried out by exciting iodide into the lowest CTTS states. However, the Rossky *et al* description of the CTTS states raises questions about the early time dynamics in the photodetachment process ¹⁰. Furthermore, Sauer *et al* reported a difference in the photodetachment quantum yield upon nanosecond excitation at 193 nm and 248 nm ²¹. At earlier times, few studies have dealt with the pump energy dependence. Lian *et al* investigated the photodetachment process of several aqueous atomic and molecular anions at pump wavelengths of 200 nm, 225 nm and 242 nm ²². For iodide, they found that the quantum yield is near unity at all these wavelengths, but the kinetics evolve quite different at later times for 200 nm and 225 nm excitation. For 200 nm excitation, the survival probability is larger, which they explained in terms of the initial spatial distribution of the photogenerated electrons. In another contribution, Moskun *et al* ²³ used a UV white light continuum to probe the formation of I^0 (in the range of 250-340 nm region) upon excitation at 200 nm. They reported an absorption that appears within the instrument response (300 fs) and decays with the same kinetics as the electron and iodide bleach signal, pointing to a recombination of I^0 and the electron as the sole mechanism for the bleach recovery.

1.3 The solvent shell of aqueous iodide

Salt molecules consist of a cation and an anion with positive and negative charge, respectively. The ions in the salt are stabilized by ionic bonds. When the molecules are dissolved, constituent ions fall apart and become solvated by solvent molecules. These solvation interactions must overcome the rather strong ionic bond. In addition, the solvent structure is distorted to accommodate the ions. The solvent molecules are found to reside at a specific distance to the solvated ions. The layers of solvent molecules around the solute are called solvation shells or hydration shell when the solvent is water. The hydration shell can be

described by a so-called radial distribution function $g(r)$, that gives the probability (ensemble-averaged) of finding a water molecule at a distance r from the ion. For r slightly larger than anion radius, $g(r)$ is zero because the Van der Waals repulsion prevents the solvent molecules to come too close to the ion. For larger r , $g(r)$ goes through a series of maxima and minima, corresponding to subsequent solvation shells (Fig. 1.3). The position of the first maximum represents the averaged distance of ion-solvent molecule in the first solvation shell. In liquid water, only one or two such maxima are pronounced depending on the solvated ion. The number of solvent molecules in the first solvation shell or the so-called coordination number is calculated by integrating $g(r)$ from 0 to the first minimum or by fitting the $g(r)$ with a gamma-like function (see chapter 2).

The hydration structure of the Γ^- ion has been already studied extensively. The solvation structure of iodide is experimentally investigated by x-ray diffraction and x-ray absorption spectroscopy. The first peak of the I-O radial distribution function is measured to be 3.5-3.76 Å^{24,25}. X-ray diffraction studies yield coordination numbers ranging from 6 to 9^{24,26,27}. Structural data obtained from Monte Carlo (MC) and molecular dynamics (MD) simulations^{28,29,30} include an I–O RdF first peak in the range of 3.55–3.78 Å, which is within the experimentally determined range of values, and an I–H first peak in the range of 2.55–2.93 Å. The first and second RdF peaks merge into each other, suggesting a rather diffuse solvation shell. Fig. 1.3 shows a radial distribution function for I-H and I-O resulting from a density functional theory (DFT) based MD simulation by Heuft et al³¹. They found a I-O and I-H distance of 3.55 Å and 2.61 Å, respectively. Their coordination number

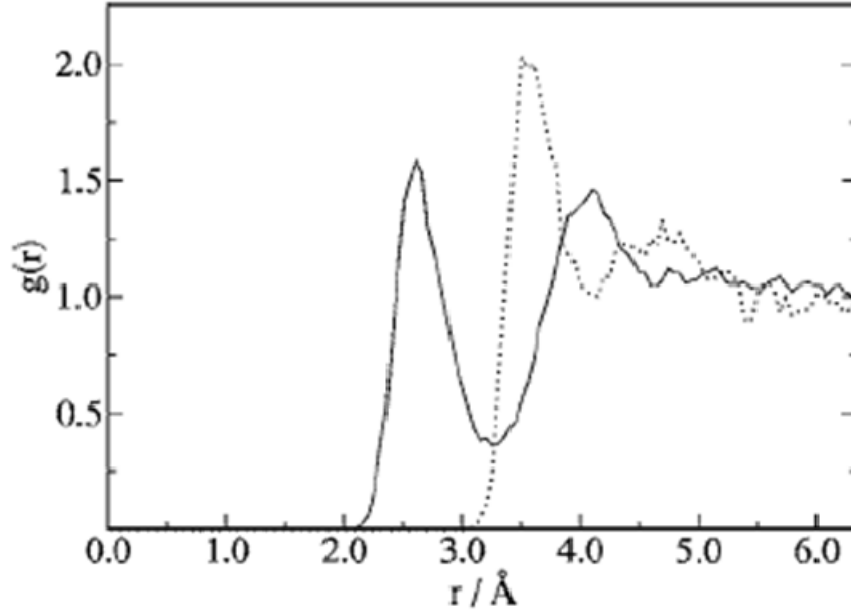


Fig. 1.3: Radial distribution function I-O (dotted) and I-H (solid). Source: ³¹

of 6.6 water molecules in the first shell is lower than most simulations but in very good agreement with our experimental value (see chapter 4). The orientation of water molecules with respect to iodide has, up to our best knowledge, not been reliably measured. The angle distribution of H-I-H and O-I-O from DFT simulation ³¹ show broad distribution ranging from 30 to 180°, though a visible peak appears at 80° in both angle distributions. This is consistent with the unstructured property found in the RDF.

The mobility of water molecules in the first solvation shell is characterized by a so-called residence time. The residence times are calculated from the time correlation function, which is defined as ³²:

$$R(t) = \frac{1}{N_h} \sum_{i=1}^{N_h} [\theta_i(0) \theta_i(t)] \quad (1.1)$$

where $\theta_i(t)$ is the Heaviside unit step function, which is 1 if a water molecule i is in the coordination shell of the ion at time t and 0 otherwise, N_h is the hydration number of this shell. A

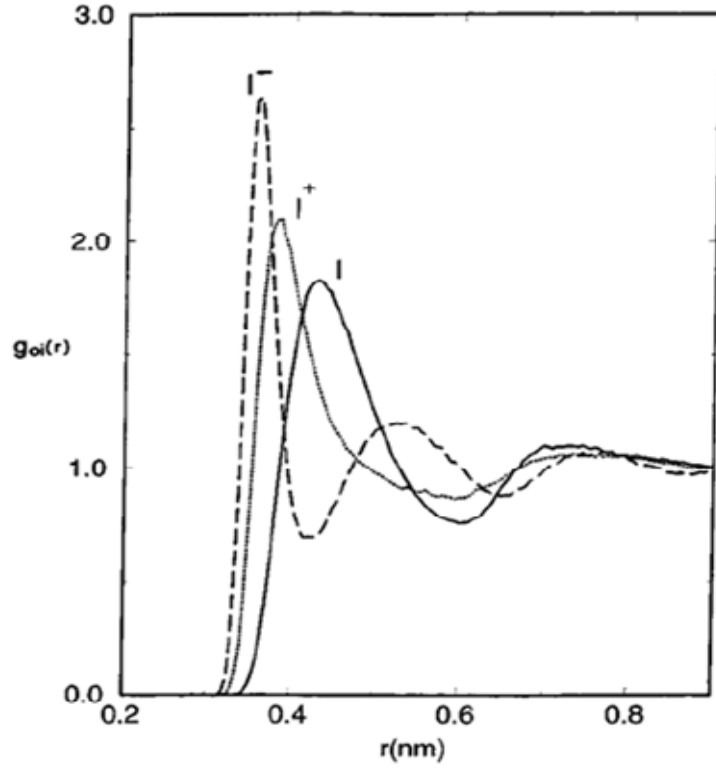


Fig. 1.4: Ion-oxygen radial distribution function of I^- , I^+ and I . Source: ²⁸

water molecule is considered as present if it is only absent for a period of $t^* \leq 2$ ps. The residence time, τ , is defined by ²⁸

$$\tau = \int_0^\infty \langle R(t) \rangle dt \quad (1.2)$$

where $\langle R(t) \rangle$ is ensemble average of $R(t)$. The residence time is obtained by either integrating $\langle R(t) \rangle$ to $t=10$ ps or fitting $\langle R(t) \rangle$ to an exponential decay. DFT simulation show that residence time of water in the first shell of iodide is 7.3 ps ³¹, while using a different simulation model Koneshan obtained 13.8 ps ²⁸. Femtosecond midinfrared nonlinear spectroscopy measurements found a residence time of 18 ± 5 ps ¹³².

Though the hydration structure of iodide has been studied both in experiment and theory, there are only a few theoretical studies on the hydration structure around neutral iodine atom ²⁸.

Fig. 1.4 displays simulated I-O RDF of iodine atoms together with that of I^- and I^+ by Koneshan et al.²⁸. Their simulation shows that the first maxima of the iodine-oxygen $g(r)$ is 4.25 Å, compared to 3.6 Å of iodide-oxygen. The broadening character of iodine-oxygen $g(r)$ results in a larger coordination number of 27, compared to 7.9 for I^- . These parameters are the subject of our study of the hydration structure around photodetached iodide, as presented in chapter 6.

1.4 Outline

This thesis is organized as follows: The present chapter provided background and previous works on aqueous iodide.

Chapter 2 introduces the principles of x-ray absorption spectroscopy (XAS) and analysis strategy for x-ray absorption data including X-ray Absorption Near Edge Structure (XANES) and Extended X-ray Absorption Fine Structure (EXAFS).

Synchrotron radiation, as the prime source for ultrafast x-ray studies performed, is introduced in chapter 3. Laser pump x-ray probe experiments with time resolution of 100 picoseconds and 250 femtoseconds are described in this chapter as well. A description for the all-optical pump-probe setup is also included.

Chapter 4 presents the structural analysis of the solvation shell around the reactant aqueous iodide. Assessment of the theoretical solvent structure derived from classical molecular dynamics (MD), quantum mechanics/molecular mechanics (QM/MM) and density functional theory (DFT) simulations are carried out by comparing the theoretical EXAFS signal with the static experiment. A fit of the experimental EXAFS data at L_3 edge is performed to yield a refined radial distribution function of the solvation shell.

Chapter 5 presents our studies on time-resolved optical spectroscopy of aqueous iodide. Results for one and multiphoton excitation are analyzed and discussed.

Chapter 6 and 7 reports time-resolved XAS with picoseconds and femtosecond time resolution, respectively. The solvent cage structure after 50 ps is determined. The electronic structure of iodine on the femtosecond time-scale is presented and discussed.

A summary of this work and an outlook on future experiments conclude this dissertation. The readers can find supplemental information on structural analysis of static and time-resolved x-ray data in the Appendix.

Chapter 2 X-ray Absorption Spectroscopy Theory

2.1 Introduction to X-ray Absorption Spectroscopy

X-ray Absorption Spectroscopy (XAS) measures the probability as a function of photon energy that an x-ray photon incident upon a sample will be absorbed by that sample. In the experiment, the energy of the incident beam of photons is changed monotonically in discrete steps, while a signal proportional to the absorption cross section is measured^{33,34}. The outcome of such XAS experiment delivers the characteristic x-ray absorption spectrum (Fig. 2.1), where the variation of the absorption coefficient shows several general features³⁵:

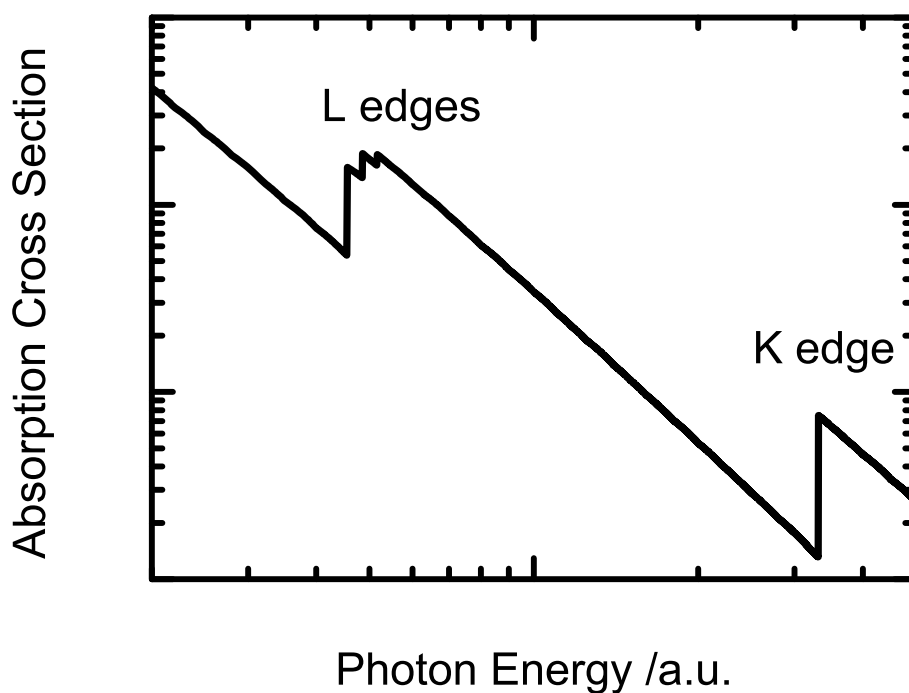


Fig. 2.1: Variation of the atomic x-ray absorption coefficient as a function of the photon energy. The characteristic saw-tooth-like features with a sudden increase of the absorption at certain energies represent the absorption edges.

1. An overall decrease in x-ray absorption with increasing energy. This feature is illustrative of the well-known quantum-mechanical phenomenon of x-ray absorption by atoms³⁶.
2. The presence of saw-tooth-like features with a sharp rise at discrete energies, called absorption edges. The energetic positions of these features are unique for a given absorbing element. They occur near the ionization energy of inner shell electrons and

also contain spectral features due to bound-bound and bound-continuum transitions. The absorption edges are related to the transitions from a particular atomic core-orbital to the free continuum (ionization of core orbitals, Fig. 2.2), but also include transitions to unoccupied bound levels just below the ionization limit.

3. When increasing the energy above an absorption edge, a weak (typically a few % of the absorption edge jump) oscillatory fine structure appears for molecules and solids that modulate the otherwise smooth absorption profile. This feature, absent for single atoms in the gas phase (and in Fig. 2.1), contains detailed structural information such as interatomic distances and coordination numbers.

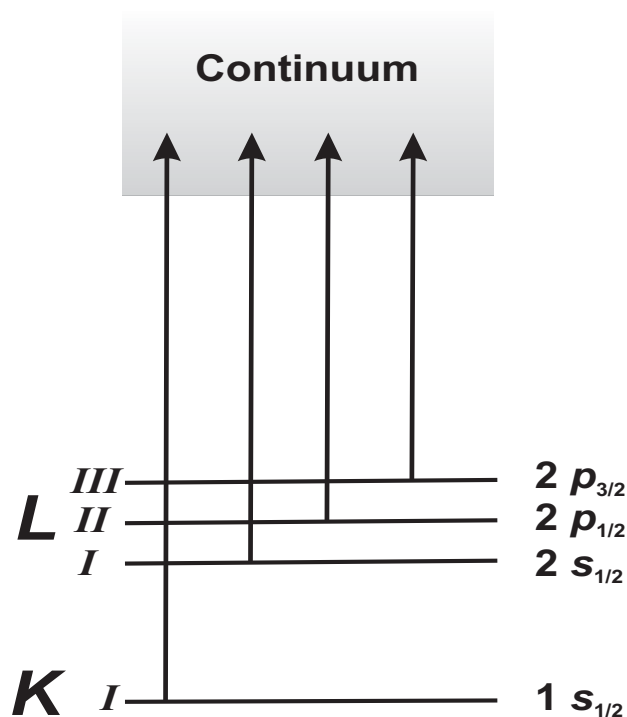


Fig. 2.2: Transitions resulting from the absorption of an x-ray photon by the deep-core electron. The ionized photoelectron can be excited to either higher-lying unoccupied state or into the continuum. Here the transitions are shown for all possible 1s and 2p core excitations, which according to nomenclature are called *K* and *L* absorption edges.

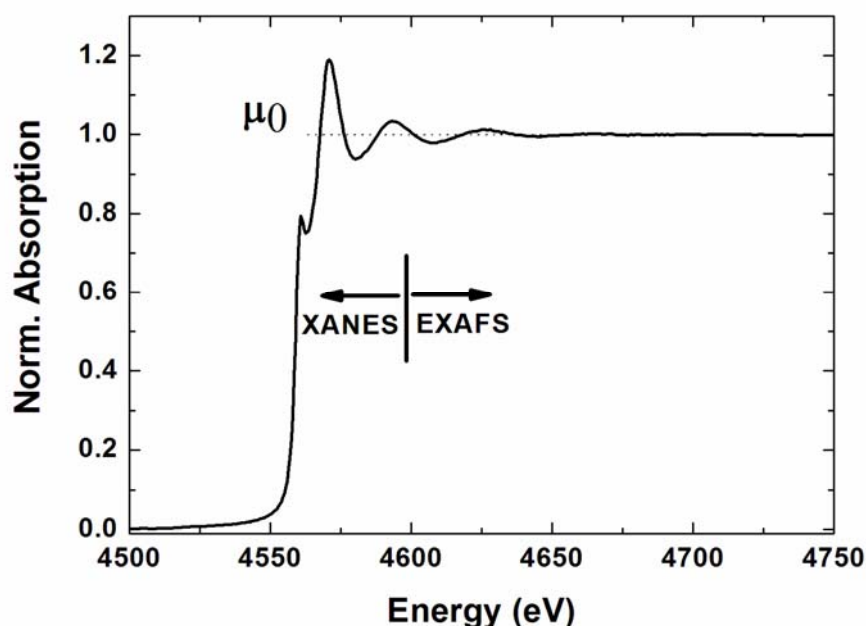


Fig. 2.3: The L_3 -edge x-ray absorption spectrum of an aqueous iodide in water. Here the division into the two characteristic spectral regions, namely XANES and EXAFS, is indicated with a vertical line at ~ 4560 eV. The horizontal dashed line marks the atomic-background intensity μ_0 used in the normalization of XAS spectra (the total edge jump equals to 1).

The nomenclature for x-ray absorption features reflects the core orbital, from which the absorption originates. In Fig. 2.2, the two innermost core orbitals are shown, namely the K and L shells and the characteristic transitions to the continuum states are indicated. For example, K edges refer to transitions from the innermost $n=1$ (n : principle quantum number) electron orbital (thus the K edge involves 1s electron), whereas L edges refer to the $n=2$ absorbing electrons (L_1 to 2s, L_2 to $2p_{1/2}$, and L_3 to $2p_{3/2}$ orbitals), to the corresponding higher-lying bound core shells and continuum states. The transitions are always referred to unoccupied states, i.e., to states with an electron above the Fermi energy E_f , leaving behind a core hole, and absorption features may appear just below the edge, which correspond to transitions to bound unoccupied levels just below the ionization limit. Above the ionization limit, the excited electron is considered as a photoelectron, and depending on its kinetic energy, it can propagate more or less freely through the material. The photoelectron propagation can be approximated by a spherical wave with a wavelength $\lambda = \frac{2\pi}{k}$, k being the photoelectron wave vector. The photoelectron wave vector can then be calculated via ^{37,38}:

$$k = \frac{2\pi}{\hbar} \sqrt{2m_e(\hbar\omega - E_B)} \quad (2.1)$$

When zooming into the vicinity of one of the absorption edges shown in Fig. 2.1, a fine structure of the spectrum can be seen (Fig. 2.3). The XAS spectrum is typically divided into two regions, the x-ray absorption near edge structure (XANES) and the extended x-ray absorption fine structure (EXAFS)^{34,39}. The transition energy between these two regions lies typically around a few tens of eV above the absorption edge, but this distinction is somewhat arbitrary and the two regions generally overlap. In Fig. 2.3, the L₃-edge XAS spectrum of aqueous iodide is shown.

2.1.1 XANES spectrum

The XANES part of the XAS spectrum depicted in Fig. 2.3 can be defined as the initial ca. 20-50 eV above the absorption edge (ca. 4560 eV). It contains information about both the electronic and the molecular structure of the system of interest^{39,40}. Indeed, it has been shown that XANES is in part determined by the geometrical arrangements of the atoms in a local cluster around the x-ray absorber in biological systems⁴¹, on surfaces⁴² and in both solid and liquid samples⁴³. This originates from the complicated electron scattering geometries found at these energies and is referred to as the multiple scattering (MS) of the excited photoelectron (Fig. 2.4). Note that at low energies above the absorption edge, the photoelectron wavelength λ_e , related to its kinetic energy (and thus its momentum k) via de Broglie's relation³⁶:

$$\lambda_e = \frac{h}{m_e v} = \frac{2\pi}{k} = \frac{\hbar}{\sqrt{2m_e(\hbar\omega - E_B)}} \quad (2.2)$$

is thus much larger than at higher energies in the so called EXAFS region⁴⁴ (see below in Section 2.1.2). It implies that the photoelectron can scatter off nearly all atoms present in the molecular cluster over various different scattering paths. As the λ_e decreases (at higher photoelectron's E_{kin} in the EXAFS range), the single scattering (SS) events between selected pairs of atoms dominate the process, although the MS is still present and should be accounted for in the proper description of EXAFS.

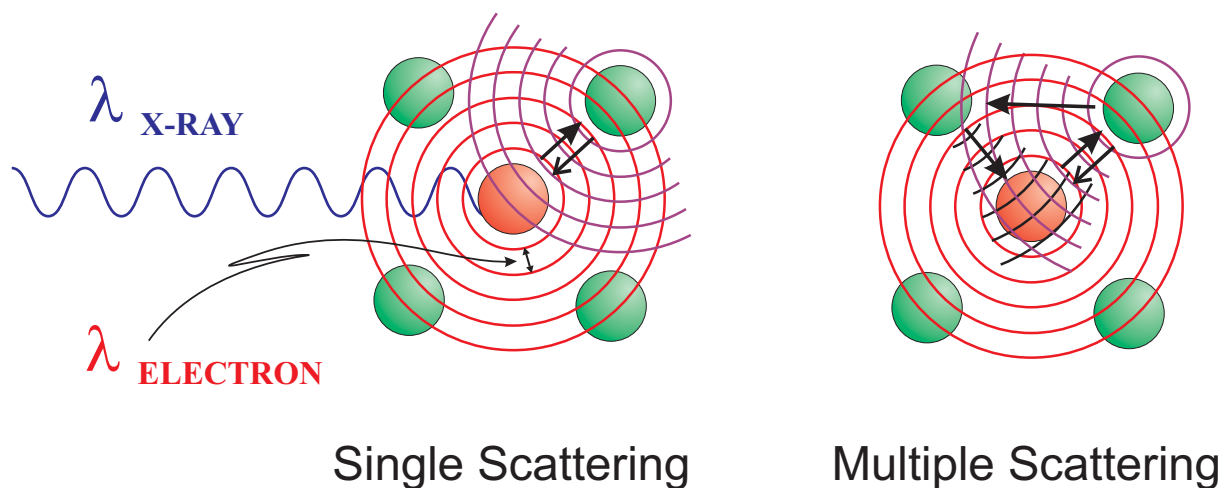


Fig. 2.4: Photoelectron wave scattering in the case of EXAFS (single scattering) and XANES (multiple scattering). The interference between the outgoing and the backscattered waves reflects the local geometric arrangement of the nearest neighbor atoms (grey spheres) around the absorber (black sphere) ¹²⁴.

The absorption resonances encountered in the XANES region, in particular in the first 10 eV energy range above the absorption threshold (which often lies a few eV below the ionization threshold of a given shell), have a physical origin, which is different for different classes of materials: it is dominated by the transitions to bound valence states or quasibound states (so-called shape resonances in molecules), core excitons in ionic crystals, unoccupied local electronic states in metals and insulators, etc. These are the states that bind the systems together in molecules and solids and determine their electronic structure. Therefore a careful analysis of this energy range delivers valuable information about the electronic landscape of the unoccupied valence shells in molecules (which are those that determine the chemical reactivity) and unoccupied density of states in solids ⁴⁵. In addition, the energies and intensities of the transitions to these states reflect the valency of the involved ions, which may change for different molecular symmetries or local bonding around the absorber and following the charge transfer reactions (i.e. oxidation state induced shift due to photoinduced electron transfer) and therefore are monitored in the XANES spectra.

It has been shown for several molecular and crystalline systems that the effective charge of the atom can be measured by means of the so called valence shift of the core level binding energy^{46,47,48,49}. Due to a weak but non-zero overlap of the core levels with valence shells, the ionization threshold and low-energy MS resonances change with the charge state of the absorber and affects the observed transition energies and intensities in the XANES region. The quantitative analysis of these effects is rather involved as the corresponding XANES absorption features are in addition strongly influenced by the local surroundings environment (eg. ligand system and their bondings to the absorbing central atom), also giving rise to the so called chemical shift^{50,51,52}

Furthermore, since the XANES transitions are subject to the same selection rules as optical transitions, the partial relaxation of these rules yields the information about the local symmetry around the absorber, which may manifest itself in the XANES region by the enhancement of formally-forbidden transitions as the case of $[\text{Fe}^{\text{II}}(\text{bpy})_3]^{2+}$ ⁵³. At higher energies (just above the ionization limit), the XANES spectra are largely dominated by the aforementioned MS events^{54,55,52}. The shape of XANES spectra concerning the number of MS resonances and their relative intensities is rather similar for each type of molecular symmetry^{52,54,56}. Therefore, XANES features are considered to be very sensitive to small changes of the local molecular geometry⁵⁷ and can even couple to nuclear motion^{58,59}. In several studies, it has been reported that the local geometry of a molecule can easily be recognized by the shape of its XANES spectrum, and the corresponding energies of the MS features were found to be strongly correlated to the interatomic distances^{60,61,62}. Furthermore, the spectra of K edges are different from those of $L_{2,3}$ edges (see Fig. 2.2), since K shells release s-electrons and L_2 and L_3 shells release p-electrons.

2.1.2 EXAFS spectrum

The EXAFS region covers the high-energy continuum above the ionization threshold (above 4560 eV for the spectrum shown in Fig. 2.3). It is dominated by an oscillatory pattern, which can be related to the photoelectron single scattering events with the neighboring atoms⁴⁴. In this regime, the photoelectron states can be approximated with spherical waves.

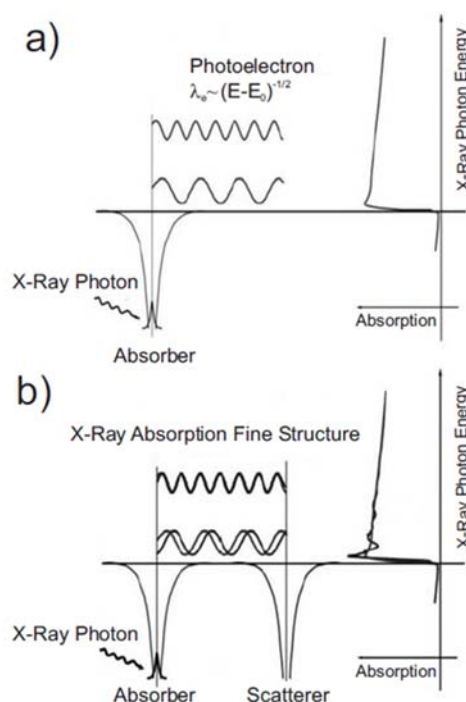


Fig. 2.5: The photoelectron scattering off the neighboring atoms causes the characteristic oscillatory pattern (the so called X-ray Absorption Fine Structure) in the EXAFS region of the x-ray absorption spectra (b). In the absence of the surrounding atoms(a) the absorption coefficient reflects only the atomic-background absorption (gas-phase spectrum) of the isolated absorber atom. The figure is taken from Ref.¹²⁵

The oscillatory structure is due to the interference between the outgoing photoelectron wave and the wave scattered back at neighboring atoms (see Fig. 2.5). Therefore, it does not exist in the case of the isolated atom (Fig. 2.5 a). The oscillatory pattern superimposed onto the gas-phase (or atomic-like) background absorption spectrum is referred to as the x-ray absorption fine structure (XAFS) and it includes both the XANES and EXAFS regions. As the photoelectron wavelength λ decreases with increasing photoelectron kinetic energy, at sufficiently high energies the electron scattering is such that the only significant contributions

to the final state wave function in the vicinity of the absorbing atom comes from paths in which the electron is scattered only once (SS events, Fig. 2.4), since MS probabilities decrease stronger with increasing energy^{44,63}. The photoelectron spherical wave emitted from the core-excited absorber is damped out rapidly due to inelastic losses caused by the extended valence orbitals of the nearby-lying atoms, and can be approximated by its mean-free path λ . The fact that multiple-scattering events can be neglected allows a straight forward analysis of the local structure via the analysis of the data by a simple Fourier transformation⁶⁴. For this purpose one generates a normalized XAS spectrum (normalized to the absorption edge jump $\Delta\mu_0(E)$ under consideration), which is defined as the normalized oscillatory part of $\mu(E)$ (the absorption coefficient), i.e., the EXAFS, via:

$$\chi(E) = \frac{\mu(E) - \mu_0(E)}{\Delta\mu_0(E)} \quad (2.3)$$

where $\mu_0(E)$ corresponds to the atomic-like background underlying the EXAFS pattern (see Fig. 2.5a) and $\Delta\mu_0(E)$ being the normalization factor corresponding to the absorption edge jump (a step-function-like sudden increase of the net absorption coefficient at the ionization threshold). At this point, it is convenient to switch from energy space to photoelectron wavevector space, so called k-space, in order to describe the interference effects in electron scattering. Using Eq. 2.1 and 2.3, we can generate $\chi(k)$ from the experimental data. This can be interpreted with the so-called EXAFS equation:

$$\chi(k) = \sum_i S_0^2 N_i \frac{|f_i(k)|}{k R_i^2} \sin(2kR_i + 2\delta_c + \phi) e^{-2\sigma_i^2 k^2} e^{-2R_i/\lambda(k)} \quad (2.4)$$

which is the standard EXAFS description proposed by D. Sayers et al. in Ref.⁶⁴. The structural parameters, for which the subscript i refers to the subgroup of N_i atoms with identical structural properties, e.g., (a) bond distance R_i and chemical nature, (b) the coordination number (or number of equivalent scatterers) N_i , and (c) the temperature-dependent root mean square fluctuations in bond length σ_i^2 , which should also includes effects due to structural disorder. Furthermore, $f_i(k) = |f_i(k)|e^{i\phi(k)}$ stands for the backscattering amplitude, δ_c is the

central-atom partial-wave phase shift of the final state, $\lambda(k)$ is the energy-dependent photoelectron mean free path (not to be confused with photoelectron's de Broglie wavelength λ_e , and S_0^2 is the overall amplitude reduction factor. Although the original EXAFS formula was derived to account for SS events from neighboring atomic shells only, the same phenomenological description can be used to represent the contribution from N_i equivalent MS contributions of total path length $2R$ ^{35,65}. In relation to the structural analysis, the EXAFS description provided by Eq. 2.4 includes the most relevant and essential parameters required for fitting the local atomic structure around the absorbing atom from the measured EXAFS ^{66,67}. The dependence of the oscillatory structure on interatomic distance and energy is described by the $\sin(2kR)$ term in Eq. 2.4. Fig. 2.6 shows this oscillatory part for an example of two nearest-neighbor distances $R_2 < R_1$.

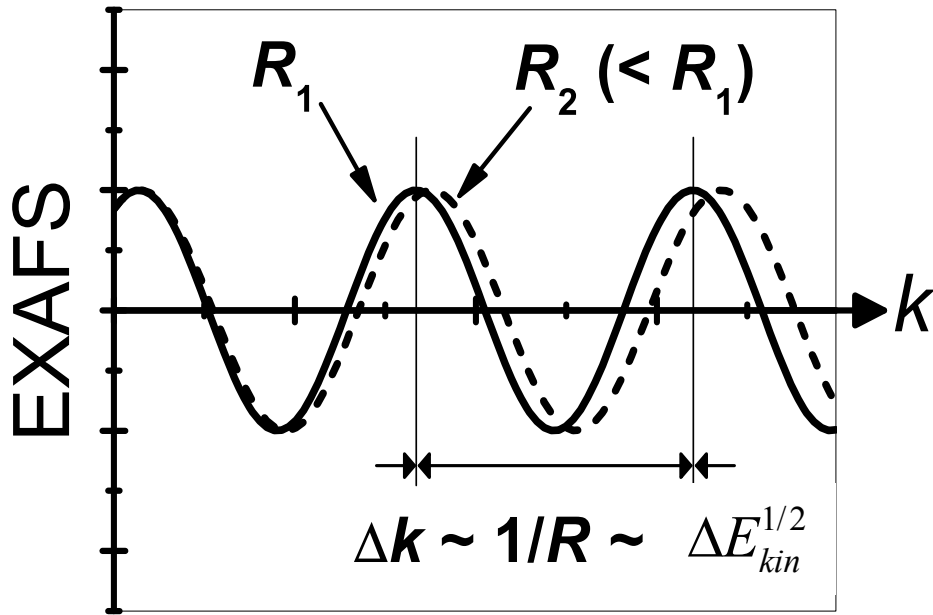


Fig. 2.6: The characteristic oscillations of the EXAFS function $\chi(k)$ (obtained via Eq. 2.4) in photoelectron wave vector space (k-space) are the measure of the interatomic bond distance between the absorber and the nearest neighbors R_1 . The observed shifts of $\chi(k)$ will reflect the bond length changes as shown here in the case of bond contraction $R_2 < R_1$. Source: ⁸⁸

It is clear that the $\chi(k)$ oscillations for two different distances show different periods (Fig. 2.6) in k-space (and thus energy space) with respect to both distances, which can be directly

linked to different interatomic distances from R_1 to R_2 ($\leq R_1$) and such shifts are often observed in EXAFS spectra of two distinct chemical species (i.e. the ground and excited states of a complex). The decrease of the photoelectron wave amplitude due to the mean free path and finite lifetime (including the ultrashort core-hole lifetime) of the electron is captured by the exponential term $e^{-2R_i/\lambda(k)}$. This factor is largely responsible for the relatively short range probed in an EXAFS experiment (up to a few tens of angstroms at most). The strength of the reflected interfering waves depends on the type and number of neighboring atoms and is governed by the backscattering amplitude $|f_i(k)|$ and hence is primarily responsible for the intensity of the EXAFS signal. Other factors, namely, the spherical-wave factors ($1/kR^2$) and mean-free path terms, appear secondary but are important for a quantitative description of the EXAFS amplitude. The phase factor $\phi = \arg f(k)$ reflects the quantum mechanical wavelike nature of the backscattering process. A somewhat larger contribution to the overall phase is given by the phase shift $2\delta_c$ at the position of the absorbing atom, since the photoelectron encounters the potential created by this atom twice. These phase shifts account for the difference between the measured and geometrical interatomic distances, which is typically a few tenths of an angstrom and must be corrected by either a theoretical or an experimental reference standard. Another exponential term $e^{-2\sigma_i^2 k^2}$, present in Eq. 2.4, accounts for the Debye-Waller (DW) broadening to a good approximation, is partly due to thermal effects, which cause the atoms to fluctuate around their equilibrium atomic positions. This small jitter in their positions smears out the otherwise sharp interference pattern of the rapidly varying $\sin(2kR)$ term with increasing k . The effects of structural disorder are similar and they give an additive contribution to σ_i^2 . In the case of asymmetric distribution of distances within a scattering shell (large anharmonicity), a cumulant expansion of the EXAFS equation may include the higher orders of σ_i^2 within the DW factor (i.e. σ_i^4 etc.) and the total phase of the EXAFS function³⁴. In any case, the DW effect seems more pronounced at shorter photoelectron wavelengths, and hence it terminates the EXAFS at sufficiently large energy beyond $k \sim 1/\sigma$, which is typically around 10^{-1} \AA . Finally, S_0^2 is a many-body effect due to the relaxation of the system in response to the creation of the core hole⁶⁸. It is usually approximated by a constant, which phenomenologically accounts for inelastic losses upon the creation of the photoelectron. The origin of such losses is related to multiple electronic

excitations of other electrons in the surroundings of the absorber. A photoelectron (thus with excess of kinetic energy) can excite some passive electrons in the valence shells to either a higher-lying bound state (shake-up process) or to continuum state (shake-off process) ³⁴. In consequence, the loss of the kinetic energy in the excitation process will shift the phase of the corresponding EXAFS oscillation and may result in an altered interference condition, which in turn affects the measured EXAFS amplitude.

2.1.3 EXAFS analysis for liquid

Unlike crystalline or ordered molecular systems, where the structure can be precisely determined (eg. via XRD), the ensemble structure of a disordered system such as liquids, glasses and gas phase is described by pair radial distribution function. The measured EXAFS signal, $\langle \chi(k) \rangle$, is dominated by single scattering from neighboring atoms to absorbers. Thus, in multi component case the EXAFS signal at an edge of absorber α , $\langle \chi_\alpha(k) \rangle$, is given by the sum of contributions from all species β integrated over the corresponding partial radial distribution function $4\pi\rho_\beta r^2 g_{\alpha\beta}(r)$ (ρ_β being average atomic density of specie β , $g_{\alpha\beta}(r)$ being radial distribution function of species β with respect to species α)

$$\langle \chi_\alpha(k) \rangle = \sum_{\beta} \int_0^{\infty} 4\pi\rho_{\beta} r^2 g_{\alpha\beta}(r) \gamma_{\alpha\beta}^{(2)}(k, r) dr \quad (2.5)$$

where $\gamma_{\alpha\beta}^{(2)}(k, r)$ is the pair signal which can be approximated based on single-scattering expression and being rewritten as ⁶⁹:

$$\gamma_{\alpha\beta}^{(2)}(k, r) \approx A_{\alpha\beta}(k, r) \sin(2kr + \phi_{\alpha\beta}(k, r) + O(\chi_4)) \quad (2.6)$$

where $A_{\alpha\beta}(k, r)$ and $\phi_{\alpha\beta}(k, r)$ are amplitude and phase shift function. The later function is roughly proportional to k as $\phi_{\alpha\beta}(k, r) \sim -2ka$, a being a constant within 0.3-0.4 Å, responsible for the shift of the peaks of the Fourier transform of EXAFS spectrum with respect to the actual position. The amplitude function $A_{\alpha\beta}(k, r)$ includes the functional dependence of the back-

scattering amplitude and the effect of inelastic losses, resulting in a roughly exponential decrease with r . This explains the short range order structural sensitivity of EXAFS. In reality the upper integration of Eq. 2.5 is 6-10 Å. Eq. 2.5 is widely used for calculation of the EXAFS signal for a simulated radial distribution of nearest neighbor^{70,71,72}. This approach has also been applied to assess the validity of QM/MM, CMD and DFT simulation, as reported in the paper attached to chapter 4.

In principle, one can derive information of the radial distribution function from the measured EXAFS signal. This strategy has been developed and employed by Filipponi and D'Angelo for disordered system such as liquids and glasses^{73,74}. The success of this method stems from the ability to model a correct shape of the distribution and from the availability of EXAFS equations to calculate the ensemble average of the EXAFS signal over that particular distribution. A four-parameter model function based on a Gamma-like function is suitable to mimic an asymmetric bond-length distribution⁷⁵. The probability of finding one atom at distance r from the absorber is given by:

$$p(r) = \frac{2}{\sigma|\beta|\Gamma(4/\beta^2)} \left(\frac{4}{\beta^2} + \frac{2(r-R)}{\sigma\beta} \right)^{(4/\beta^2)-1} \exp \left[- \left(\frac{4}{\beta^2} + \frac{2(r-R)}{\sigma\beta} \right) \right] \quad (2.7)$$

which is valid for $\beta(r-R) > -2\sigma$ (with $p(r)=0$). $\Gamma(p)$ is Euler's Gamma function, calculated for $4/\beta^2$ and defined on the positive real axis. R , σ^2 and β are the three distribution parameters representing the average distance, variance and skewness of the distribution, respectively. A fourth multiplicative parameter N can be introduced to represent the average coordination number. The function $Np(r)$ takes the role of $4\pi\rho r^2 g(r)$ in Eq. 2.5. Eq. 2.7 is valid for positive and negative β , in the limit $\beta \rightarrow 0$ the equation merges in to a Gaussian distribution. Therefore, it is a useful model function when the asymmetry has to be fitted as well. In comparison to MD simulations, Eq. 2.7 is a reasonably accurate model of bond length distribution in solids and liquids.

The parameters of Eq. 2.7 show a strong correlation, and a similar fit goodness can be archived using very different parameters choices. It is clear that the use of additional

information on a system to deliver physical constraints is important. A fundamental constraint is the symmetry upon exchange of atomic type $g_{\alpha\beta}(r) = g_{\beta\alpha}(r)$. In the peak fitting approach this results in a coordination number constraint. By defining the coordination number of species β round α as $N_{\alpha\beta} \sim g_{\alpha\beta}(r)\rho_\beta$ we get $N_{\alpha\beta} = N_{\beta\alpha}\rho_\beta$ in other word the coordination number of mixed bond seen from the two atomic sites at different ends must scale as the number density of the neighbor type atoms. In peak fitting approach the initial parameters for $g(r)$ are set based on a decomposition of a theoretical $g(r)$. Since the $g(r)$ of liquids is rather broad, it is necessary to decompose it into one (or more) short-range peaks and a long-range tail function $g_t(r)$. While the parameters of peak functions are refined, the EXAFS contribution of tail $g(r)$ is kept fixed. It is important to establish constraints between parameters of the peak functions. Based on a concept of diffraction signal $S(k)$, where the signal is a constant when $k \rightarrow 0$, one can derive a constraint for zero-order (or even higher) of $\Delta S(k)$ ⁷⁴:

$$\left(\frac{\partial^m \Delta S(k)}{(\partial k)^{2m}} \Big|_{k=0} \right) = 0 \quad (2.8)$$

which corresponds to

$$4\pi\rho \int_0^\infty r^{2+2m} \Delta g(r) = 0 \quad (2.9)$$

The decomposition of $g(r)$ can be rewritten as:

$$4\pi r^2 \rho g(r) = N_1 p_1(r | R_1, \sigma_1^2, \beta_1) + N_2 p_2(r | R_2, \sigma_2^2, \beta_2) + 4\pi r^2 \rho g_t(r) \quad (2.10)$$

The refinement of the peak parameters is then performed with the following constraints, resulting from Eq. 2.9 for $m=0$ and $m=1$:

$$\begin{cases} N_1 + N_2 = N^{tot} \\ N_1(R_1^2 + \sigma_1^2) + N_2(R_2^2 + \sigma_2^2) = M_2^{tot} \end{cases} \quad (2.11)$$

where N^{tot} and M_2^{tot} are the total coordination number and the total second moment of the matter distribution about $r=0$ associated with the two short-range peaks.

The constraints still allow for a redistribution of the coordination environment around the photoabsorber but prevent the fit from assuming unphysical values. In a two-peaks plus a tail model with the constraints the number of free parameters is six. The method has been successfully used for several liquid systems^{73,75,76} and should be generalized for peak fitting approach in EXAFS data analysis for disordered system. This strategy is applied for EXAFS analysis for iodide as presented in chapter 4.

2.2 Basic Principles of Multiple Scattering Theory

The multiple scattering (MS) theory, in general terms, describes the transport of particles interacting with a host medium through various processes of scattering, absorption and emission, the first-mentioned being the most important and significant one. In the particular case of the XAS phenomenon^{35,77,78,79}, the MS theory describes the propagation of the photoelectrons and the scattering events that a photoexcited core electron undergoes, once it is ionized from the absorbing atom and escapes with sufficient kinetic energy from the atom. The presence of the surrounding atoms (including their electronic clouds) cause the photoelectron to move on "bent" trajectories and to scatter (eg. backwards) onto the absorber and thus a quantum interference effect of both the outgoing and returning waves occurs. In plain words, one can think of an XAS experiment as of an interferogram of the atomic environment around the absorber.

2.2.1 Understanding XAS Phenomenon within MS Theory

The mathematical description of the XAS phenomenon is quite involved, therefore it will be limited here to its most fundamental aspects^{35,77,78}. As mentioned above, the x-ray absorption process involves the photoionization of a core electron, creating a core-hole state, and the excitation of the photoelectron to either higher-lying unoccupied states (below the ionization

limit) or continuum states above the ionization threshold. In a one-electron picture, within the dipole approximation, XAS measures the dipole-mediated transition of a deep core electron $|i\rangle$ of the absorbing atom into an unoccupied final state $|f\rangle$. The probability for such a transition is described by Fermi's Golden Rule ³⁴:

$$\mu(E) \propto \sum_f^{E_f > E_F} \left| \langle f | \hat{\epsilon} \cdot \vec{r} | i \rangle \right|^2 \delta(E - E_f) \quad (2.12)$$

where $\hat{\epsilon} \cdot \vec{r}$ is the dipole operator for the incident electromagnetic wave interacting with the atom and the summation extends over all the energies above the Fermi energy E_F . The deep core initial state $|i\rangle$ is usually the 1s (K-edges), 2s or 2p state (L-edges), although transitions from higher lying core levels (N, M, etc.) are also regularly measured. The XAS description is based on the accurate representation of the quantum interference of these two states using Eq. 2.12. In addition, the integral included in Eq. 2.12 applies to a product of electron wavefunctions, where the initial state can be approximated, to a good extent, as an extremely localized state around the absorber nucleus (and thus the dipole approximation is well-justified), whereas the final state contains a mixture of outgoing and back-scattered electron waves. Therefore, the absorption coefficient $\mu(E)$ in Eq. 2.12 will be mainly affected by the interference pattern at the center of the absorbing atom. One can distinguish two general strategies to solve Eq. 2.12. The first one consists of an accurate representation of both the initial core state $|i\rangle$, the presence of a deep-core hole, and the final state $|f\rangle$, followed by an explicit evaluation of the integral implied by Fermi's Golden Rule. This strategy, in general terms, is the approach taken by molecular orbital (MO) theory ^{80,81}.

The second approach uses the MS theory to rewrite Eq. 2.12 in terms of Green's functions ^{35,82}. In this case, we consider a flat interstitial potential V_{int} due to the system of ions and electrons in a given system (region II in Fig. 2.7a). The ions are the scattering sites of potential δV . The total Hamiltonian of such a system can be expressed as $H = H_0 + V_{\text{int}} + \delta V$. The scattering atomic potentials H_0 are approximated with spherically symmetric Coulomb-type potentials embedded within the interstitial potential V_{int} (region I in Fig. 2.7a). This

approximation is called muffin-tin (MT) potential approximation. Within the MT approximation, the electron wavefunction can be expressed by spherical harmonics within the MT potential with additional radially-dependent part, which extends into the V_{int} region. The outer region (region III in Fig. 2.7a) sets the specific boundary conditions onto the electron wavefunction acting within the cluster sketched in Fig. 2.7a.

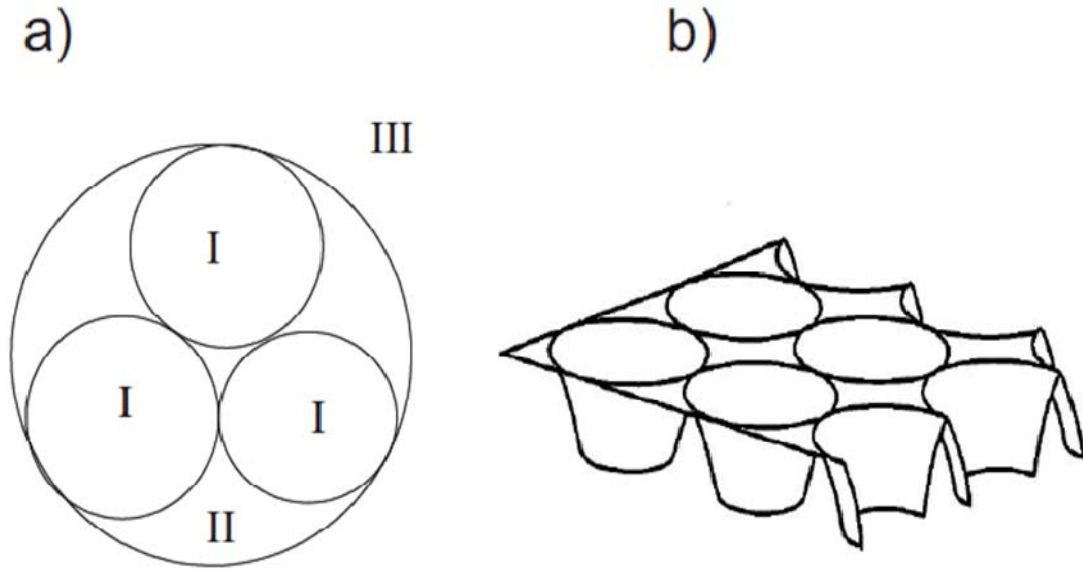


Fig. 2.7: Schematic representation of the muffin-tin potentials. In (a) the top-view of a MT potential energy surface is shown, indicating the three characteristic regions used in their construction. The region I describes the atomic potentials, embedded into a flat interstitial region II and surrounded by the outer region III, which provides the suitable boundary conditions for the photoelectron wavefunction. In (b), a 3D sketch of the MT potential energy landscape is displayed. The effect of the flat interstices is clearly visible. Taken from Ref. ³⁵

In Fig. 2.7b, a two-dimensional drawing of the potential energy landscape within the MT approximation is illustrated. Here, only the regions I and II of Fig. 2.7b are depicted in order to highlight the truncation (approximation) effect of the flat interstitial potential V_{int} superimposed onto the spherically-symmetric atomic potentials. Using the total Hamiltonian H , the one-particle Green's function can be written as $G(E) = 1 / (E - H + i\zeta)$ (where ζ is the net lifetime of the core-hole state including the effects of both intrinsic and extrinsic losses) ³⁵. The Eq.

2.12 can be then rewritten, using the operator form of this Green's function, $\sum_f |f\rangle \mathbb{G}(E) \langle f|$ ⁷⁷, as:

$$\mu(E) \propto \frac{1}{\pi} \text{Im} \langle i | \hat{\varepsilon}^* \cdot \vec{r} \mathbb{G}(E) \hat{\varepsilon} \cdot \vec{r} | i \rangle \Theta(E - E_f) \quad (2.13)$$

where $\Theta(E - E_f)$ is the Heaviside step function to assure that the absorption cross section is non-zero only above the Fermi energy E_f . In this representation, $\mathbb{G}(E)$, is the full one-electron propagator in the presence of the scattering potential. At this point, the MS expansion can be derived by expanding the Green's function to a Dyson series, $\mathbb{G} = G^0 + G^0 T G^0 + \dots$, where G^0 is the free-electron propagator, $\mathbb{G}(E) = 1 / (E - H + i\zeta)$ and $T = V + V \mathbb{G} T$ is the full atomic scattering matrix^{83,84}. The T -matrix can be expressed in terms of the single site scattering matrices t by:

$$T = t + t G^0 t + t G^0 t G^0 t + \dots \quad (2.14)$$

Dyson equation is then solved using Eq. 2.14, which is recognized as the Taylor expansion:

$$\mathbb{G} = G^0 + G^0 t G^0 + G^0 t G^0 t G^0 + \dots \quad (2.15)$$

$$\mathbb{G} = (1 - G^0 t)^{-1} G^0 \quad (2.16)$$

The MS fine structure can then be obtained by taking an appropriate trace over the matrix \mathbb{G} , which includes all those elements of \mathbb{G} corresponding to the absorbing atom and the angular momentum of the photoelectron final state.

2.3 Conclusions

In the scope of the scattering theory, we can conclude that at high energies the scattering of excited electrons is weak, such that the only significant contributions to the final state wave function in the vicinity of the absorbing atom come from paths in which the electron is scattered only once (EXAFS). However, when lowering the photoelectron energy into the XANES region, MS becomes more and more dominant. It appears from the above that because MS is sensitive to multiatomic correlations, it delivers information not only on the radial

distances of the surrounding atoms but also on their orientations relative to one another, including bond angles. In comparison, EXAFS mainly delivers the pair correlation function (i.e. RDF) and the mean displacement. In summary, direct structural information can be extracted from XANES, which, like EXAFS, is due to scattering of the photoexcited electron by neighboring atoms. However, while for EXAFS the theory is straightforward and easy to handle, XANES requires more elaborate theories beyond one-electron theories. Furthermore, multielectronic interactions complicate matters and their theoretical treatment is specific for each class of atom and requires introducing spin-orbit effects, crystal-field effects, and multiplet effects that originate from two-electron Coulomb and exchange interaction between electrons from different orbitals. These, combined with the overlapping contributions that occur in the XANES, have delayed its use as a structural technique compared to EXAFS. Up to date, it is mainly used to deduce the electronic structure of various systems. Only very recently, the first quantitative treatment of the XANES spectra, within the so called full MS theory, has delivered the structural details on a comparable level to the EXAFS analysis.

To summarize, XAS offers the following advantages as a spectroscopic technique for the analysis of geometric structures:

- It can be implemented in any type of media: gases, liquids, and solids (amorphous or ordered)
- It is highly selective, since one can interrogate one type of atom specifically, e.g., the central atom of a given solute inside a bath of solvent species by simply tuning into its characteristic absorption edge.
- It probes mainly the local structure around the atom of interest, which is fine for ultrafast processes, since short time scales correspond to short distance scales, i.e., on the femtosecond time scale the evolving chemical reaction affects only nearest neighboring atoms.
- It delivers both electronic and structural information. This is essential in chemistry, as it is the electronic structure changes that drive the nuclear dynamics (at least in a Born-Oppenheimer regime).
- The precision of structural determination by EXAFS is on the order of 10^{-2} - 10^{-3} Å, which is excellent for observing the transient structures of reaction intermediates.

All these advantages are particularly attractive for the study of dynamical processes in chemistry, biology, and material science and call for the extension of XAS to the ultrashort time domain.

Chapter 3 Experimental Method

3.1 Synchrotron Radiation Source

A synchrotron is a charged-particle accelerator in which the particle is accelerated by an electric field. Its orbital path (radius) is kept constant by a synchronously ramped magnetic field to compensate for the relativistic increase in particle mass. During acceleration, the particle approaches rapidly the speed of light.

The term synchrotron nowadays describes a large scale facility, which produces light from the infrared to extremely hard x-rays. Such a facility usually comprises of 3 main elements (Fig. 3.1): 1) A linear accelerator which yields ~ 100 MeV kinetic energy over a short path. 2) The booster is a circular shaped accelerator (270 m circumference for the SLS), which delivers the composite word “synchrotron” (synchronous cyclotron). The electrons entering the booster are already ultra-relativistic and have a speed very close to that of light. When the electrons are further accelerated by electric fields, they no longer gain considerable speed, but rather mass

via $m_r = \frac{m_0}{\sqrt{1 - (v/c)^2}}$. Thus the Lorentz force by the bending magnets $F_L = e \cdot \vec{v} \times \vec{B}$ need to

compensate the centrifugal force $F_c = \frac{m_r v^2}{r}$ and this requires synchronous increasing of the magnetic field (B), as the mass m_r increases with kinetic energy. 3) Finally, inside the storage ring, magnetic fields are kept constant again, and only a modest acceleration in the RF cavity is used to compensate for energy losses due to emission of radiation. The electrons in the SLS storage ring reach 2.4 GeV kinetic energy.

The SLS storage ring has a circumference of 288m, with a total of 12 straight sections, with different lengths of 4m, 7m and 11m, accommodating different insertion devices. There are a large number of dipole magnets (330 in total at the SLS) and a repetitive structure of quadropoles and sextupoles, which are used to steer the electron beam as well as to maintain a small emittance. Special attention was paid to the high vacuum system to keep the beam losses due to collision with residual gas as small as possible. However, the number of stored electrons still decreases due to electron-electron collisions, Touschek-scattering⁸⁵. This requires a new electron injection that adds new electrons to the remaining stored electron beam. The injection

is handled in the so-called top-up mode, and occurs periodically every few minutes. During the circulation, the accelerated electron emits radiation, thus losing its kinetic energy. An RF cavity, operated at 500 MHz, is used to compensate for the electron energy losses due to emission. The storage ring has a very complex diagnostic system, including correctors and orbit feedbacks to keep track of the electron beam and control its position to within 1 μ m. This guarantees a very high stability of the emitted radiation on the samples.

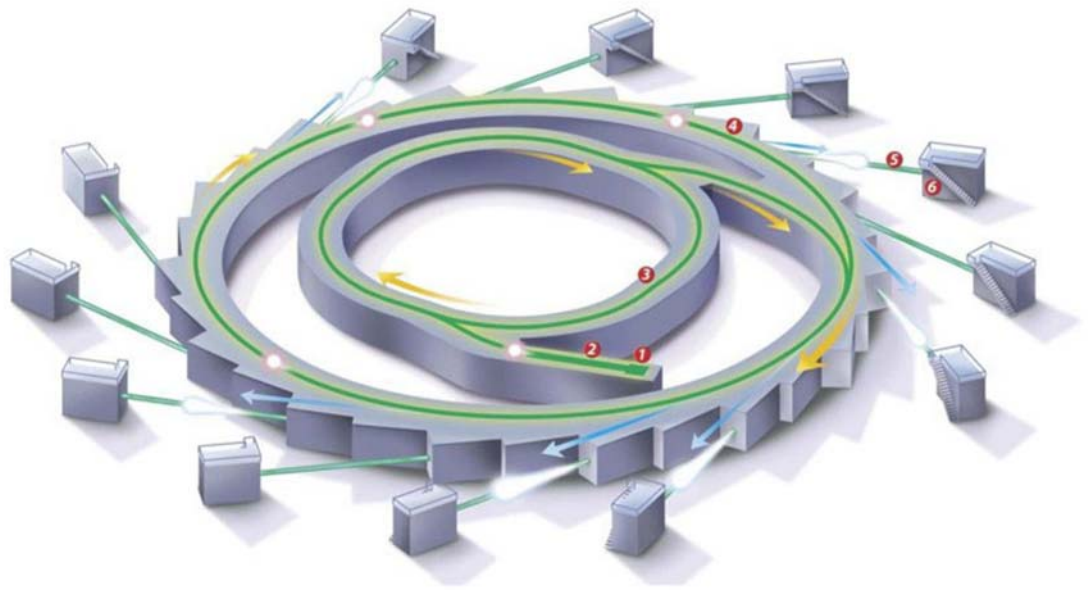


Fig. 3.1: Layout of a modern synchrotron (Australian synchrotron is illustrated). The key elements include: 1: electron gun, 2: linac, 3: booster ring, 4: storage ring, 5: beamline, and 6: experimental endstations. Source: ¹²⁶.

3.2 Bend Magnet and Undulator Radiation.

The electron circulates inside the storage ring in a well defined orbit, which is maintained by magnetic field force from bending magnets. These magnets exert transverse acceleration onto the electron beam, causing them to radiate electromagnetic waves. Another way of causing electrons to radiate is by letting them traverse an undulator, which consists of several periodic magnets of opposite polarity. The electron beam is transversely “wiggled” through the undulator gap. By wiggling the velocity of the electron beam is accelerated in a sinusoidal path and emits electromagnetic radiation. The physics of synchrotron radiation can be understood using Maxwell’s equation including relativistic and Doppler effects ⁸⁶. The properties of bend magnet and undulator radiation are discussed below.

3.2.1 Bend Magnet

A charged particle constrained to move on a curved path experiences a centripetal acceleration. Due to this acceleration, the particle radiates electro-magnetic wave. A non-relativistic particle emits radiation primarily at its frequency of revolution, with the characteristic pattern shown in Fig. 3.2a. However, as the speed of the particle approaches the speed of light, the angular distribution is distorted by relativistic effects and changes to a narrow cone of radiation in the forward direction with an angular spread $\theta \sim 1/\gamma$ where γ is the Lorentz factor $\gamma = \frac{1}{\sqrt{1-(v/c)^2}}$ (Fig. 3.2b). The SR resulting from a bending magnet is thus emitted tangentially to the electron orbit with a smaller divergence of $1/\gamma$ in the vertical direction. The peak emission in the laboratory frame, taking into account the relativistic and Doppler effects, can be expressed as ⁸⁶

$$\lambda \approx \frac{2\pi c m_0}{2\gamma^2 e B} \quad (3.1)$$

where c , m_0 , e and B are speed of light, electron rest mass and the dipole magnetic field, respectively. Each electron may be seen as a rotating searchlight. Once passing through the bending magnet, it illuminates the beamline for a very short time, thus this leads to a large wavelength bandwidth according to the Fourier-theorem. As a result of the relativistic and Doppler effects, the SR from bend magnets has an interesting relation between the emitted wavelength and bandwidth, $\Delta\lambda \approx \lambda$, where λ and $\Delta\lambda$ are peak and bandwidth wavelength, respectively. So, the emission spectrum of SR is characterized by a single parameter, the wavelength. This parameter is dependent on the electron energy and strength of the magnetic field.

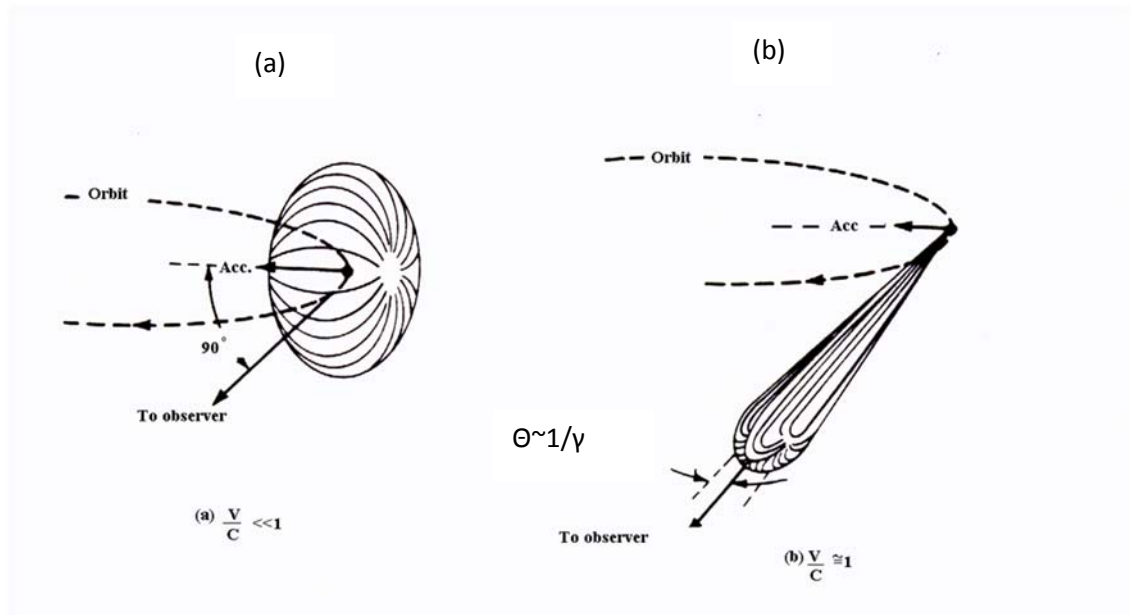


Fig. 3.2: The radiation pattern of (a) a charged particle moves in a circular trajectory at non-relativistic speed and (b) at relativistic speed. Adapted from Ref. ¹²⁷

3.2.2 Undulator and wiggler radiation

While bend magnets exist in both 2nd and 3rd generation synchrotrons, undulators have only been introduced to 3rd generation storage rings. Undulators are the most powerful generators of synchrotron radiation at storage rings. They consist of periodic dipole magnets generating an alternating static magnetic field which deflects the electron beam sinusoidally. When the electrons move in an undulator period of λ_u , each period generates a radiation cone which overlaps in a way that they interfere, giving the radiation special properties. The radiation from an undulator can be considered analogous to diffraction from a grating. In the electron coordinate, the radiation wavelength is the period of the undulator, λ_u , when translated into the laboratory frame this wavelength undergoes a Lorentz contraction and Doppler effects. In total the wavelength is $\lambda \approx \frac{\lambda_u}{2\gamma^2}$ ⁸⁶.

An important parameter describing the electron motion within the periodic magnetic field of an insertion device is the deflection parameter K given by ⁸⁷:

$$K = \frac{eB_0\lambda_U}{2\pi m_e c} = 0.934 \times \lambda_U[cm] \times B_0[T] \quad (3.2)$$

The maximum angular deflection of electron motion, in term of K, is equal to $\delta = K / \gamma$. For $K \leq 1$ the insertion device is defined as an undulator meaning the radiation from adjacent periods will interfere coherently and behave like a diffraction grating. For the first harmonic ⁸⁶:

$$\frac{\Delta\lambda}{\lambda} = \frac{1}{N} \quad (3.3)$$

where N is number of periods. For harmonic of n order, the undulator spectrum is given by ⁸⁸:

$$E_n[keV] = 0.95 \times \frac{2nE^2[GeV]}{\lambda_U \times (1 + K^2 / 2)} \quad (3.4)$$

An example of an undulator spectrum is illustrated in Fig. 3.3a. The wavelength can be shifted by changing the gap of the undulator which varies the magnetic field providing a tunable source over an extended spectral range.

Another type of insertion device for x-ray radiation is wiggler (Fig. 3.3b). Wiggler has similar design as undulator, but longer period of magnet dipole. Wiggler synchrotron radiation is similar to that produced by bend magnet, but $2N$ times as intense due to repetitive electron bending over the length of a $2N$ pole wiggler.

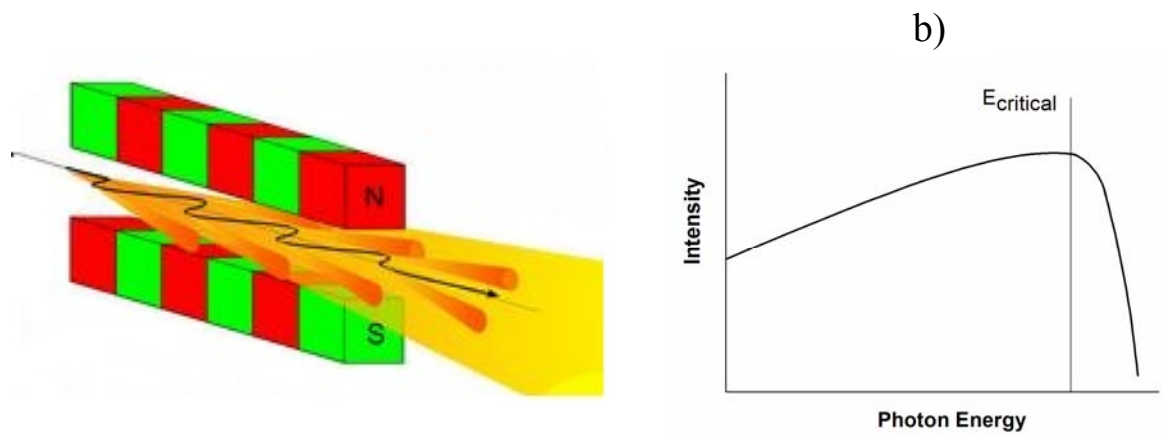
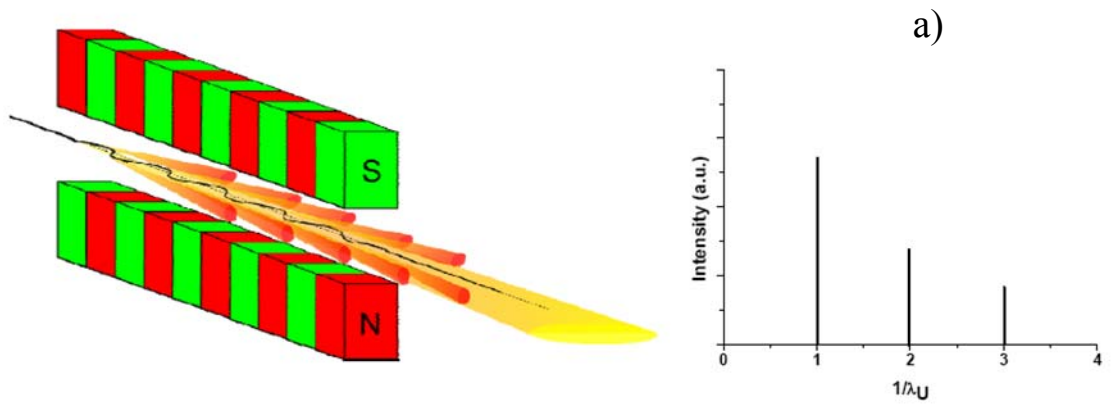


Fig. 3.3: The radiation pattern of relativistic electron traversing an undulator (a) is similar to a diffraction pattern⁸⁶. b) sketch of a wiggler and its continuous spectrum, which is analogous to that of bend magnet. The critical energy E_{critical} is sometimes defined as the max intensity, sometimes dividing the left and right regions into equally weighted regions.

3.3 Temporal Structure of Synchrotron Radiation

The RF of the SLS storage ring has a frequency of 500 MHz which creates sequential potential wells along the electron orbit, which can trap the electrons, generating electron buckets. The number of buckets depends on the circumference of the storage ring. The SLS fills 390 buckets out of a total of 480 at a round trip time of 960 ns. The electrons that are trapped in these buckets form electron bunches within a well-defined duration of 70 -100 ps. The separation between adjacent electron bunches is 2 ns (500 MHz). Since the storage ring is not completely filled there is an empty gap of 180 ns in the ring fill. This has proven its utility for removal of residual gas ions. These see an overall 1MHz alternating electric field, which effectively swings them out of the electron orbit path, so that collisions (and thus charge removal) is reduced. However, this gap can be filled with an isolated bunch without hampering its ion-removal capacity. Fig. 3.4a shows the temporal structure of the SLS storage ring. Fig. 3.4b,c are measured by an avalanche photodiode (APD) at the microXAS beamline. This electron bunch is used for time resolved investigations, as will be explained below. The total current stored in the ring is 400 mA which makes 1 mA for each bunch. The single bucket inside the gap can be filled up to 3-4 mA. This camshaft bunch allows time-resolved measurements to be performed and is a critical component to the laser-electron slicing technique.

As previously mentioned, the stored beam gradually decreases due to Touschek scattering and due to collisions with residual gas ions. The beam lifetime inside a synchrotron is ca. 4-12 hours depending on the storage ring current (which influences Touschek scattering rate). At SLS, a Touschek dominated beam lifetime of 3.5 h is estimated for the design current of 400 mA in the presence of undulators with a minimum 4 mm gap size⁸⁹. Originally, this leads to repeated injections every 4-8 hours (depending on synchrotron) to maintain a high light intensity. Since a few years, it is now possible to frequently inject a small amount of electrons every 1-2 minutes, which effectively maintains a constant beam intensity. In this top-up mode, the current of each stored bunch is topped-up if it is lower than a set value, keeping the overall average ring current quasi constant over time. Three major demands for the bunch control in top-up mode are: precise timing system, flexible control system and sophisticated diagnostics. Fig. 3.5a exhibits the schematic of the control system. SR is collected by an avalanche

photodiode (APD). The output signal from the APD is directly connected to a fast digitizer. The digitizer is externally triggered by the rate of the ring revolution frequency. A VME (Versa Module Eurocard) crate contains all controls cards and implements algorithm written in low level software to process bunch pattern and control timing of Linac and pulsed magnet to inject the required current into desired buckets of the storage ring. Fig. 3.5b shows the flowchart of the filling algorithm software. After each top-up cycle, the injection stops, the time duration to the next top-up circle is calculated according to the beam lifetime, current deadband and integrated current. During this interval, the acquired filling pattern is averaged and processed to extract the relative charge for each bucket. The bucket number is then sorted from lowest to highest charge. Whenever the beam current is lower than limit, electrons will be injected to the bucket with lowest charge until the beam current is larger than low limit plus deadband, otherwise it continues to inject to the next lowest charges. This results in a flat filling pattern with charge fluctuation of only few percents from one bucket to another. The control is executed via the SLS network using EPICS software.

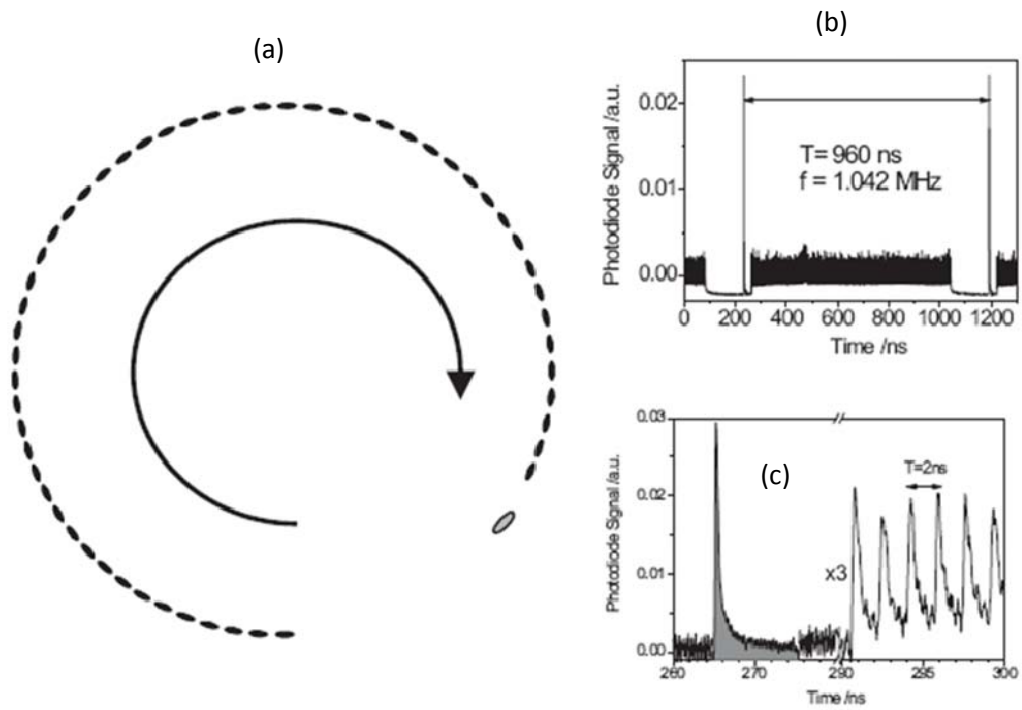


Fig. 3.4: An example of filling pattern of a modern 3rd generation synchrotron, eg. The ALS or the SLS, is shown. (b) the resulting time structure of the emitted x-ray will be determined by the particular electron bunch filling pattern of the storage ring (here the SLS filling pattern is presented) (c) The zoomed region within the empty gap, where a single electron bunch is located and emits a single x-ray pulse used for time-resolved experiment. Source: ⁸⁸

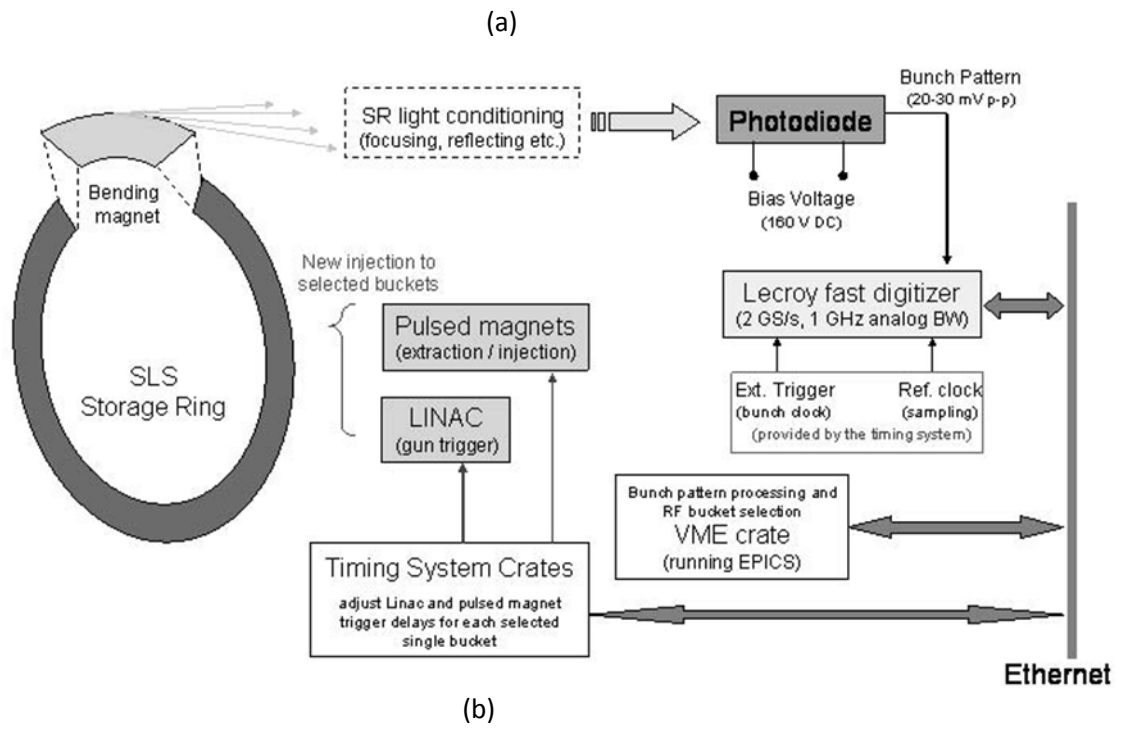


Fig. 3.5: (a) Filling pattern feedback loop architecture, (b) algorithm flowchart. Source: ¹²⁸

3.4 Static XAS measurement and microXAS beamline flux curve

Static x-ray absorption of solvated iodide around the iodine L_1 and L_3 edges were measured at the Micro-XAS beamline at the Swiss Light Source. The experimental setup is shown in Fig. 3.6. The sample is circulated by a free-flowing jet of 200 micron thickness tilted at 45° . This represents the condition used in the time-resolved XAS. The ring stores a current of 400mA giving a flux at sample position of around 1×10^{12} photons/s at L_1 and L_3 edges. The x-ray energy from the third harmonic of the U19 undulator can be tuned by a Si (111) double crystal monochromator, yielding an energy resolution of 0.8 eV at both edges. The beam is reshaped and attenuated with slits before passing through a pair of Kirkpatrick Baez (KB) mirrors which focuses the beam onto sample. Two ion chambers (Oxford Danfysik, 30 cm length, bias 1.2 kV) filled with He measure the incoming and transmitted flux through the sample. The output current is amplified by a low noise current amplifier FEMTO DLPCA-200 with a typical gain of 10^6 to 10^9 V/A. The I0 ion chamber absorbs only 0.19% of the incoming flux giving rise to 50nA at 5keV. The X-ray energy was calibrated with Ti and V foils, whose K edges were recorded and compared to the literature spectra. A 27-elements silicon detector (Ketex) was also implemented to record the x-ray fluorescence signal, but it did not produce as good S/N as in transmission mode. The edge jumps of both L_1 and L_3 edges of I are in agreement with calculations using the known cross sections (via XOP)⁹⁰. The absorption spectra were collected with an integration time of 10 s per data point giving a N/S (for the normalized spectra) of 0.0025 and 0.001 at $\Delta E=250$ eV at L_1 and L_3 edges, respectively.

The X-ray beam travelling through the ionization chamber is partially absorbed by He gas, generating primary photoelectrons. The generated electron and positive He ion are accelerated toward the two statically biased electrodes, producing output current. From this current one can determine the incoming X-ray flux prior to the chamber by the following formula⁹¹:

$$F[\text{photons/s}] = \frac{I[A] \times E_I[\text{eV}]}{(1 - T) \times E[\text{eV}] \times 1.6 \cdot 10^{-19}} \quad (3.5)$$

where F is number of photon per second, T is transmission, E_I is ionization potential of He, 24.587eV, I is current in amperes. The number of electrons created by a single photon at energy

E is $p=E/E_1$, from the measured current one can determine number of electrons per second, thus tracking back number of incident photons by dividing by p . The total incident number of photons is obtained by considering the absorption by the ion chamber. Fig. 3.7 shows the flux measurements at the three different harmonics in microXAS beamline. The dashed curve shows the calculated flux of the U19 undulator with a gap size of 7.5 mm, 400 mA storage ring current and 2.4 GeV electron beam. The black solid curve is the measurements performed around the 3rd (5.87 keV), 5th (9.79 keV) and 7th (13.73 keV) harmonics at 9 mm undulator gap at 350 mA storage ring current. The blue curve in the figure illustrates part of the micro-XAS beamline spectra extracted from the current on IC1. In this measurement, the undulator gap sizes are adjusted for maximum fluxes according to the incident x-ray energy.

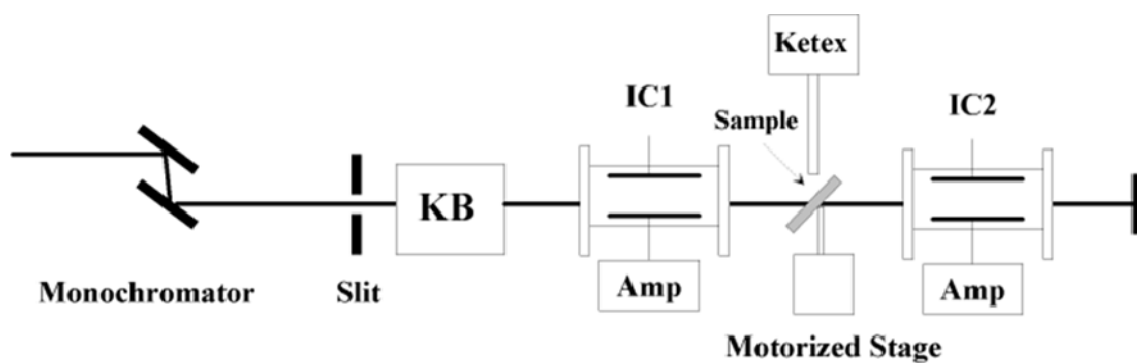


Fig. 3.6: A typical experimental setup for static XAS. IC1 and IC2 are ion chambers that measure the incoming and transmitted flux through the sample. The sample is circulated in a free flowing jet which is mounted in a motorized stage.

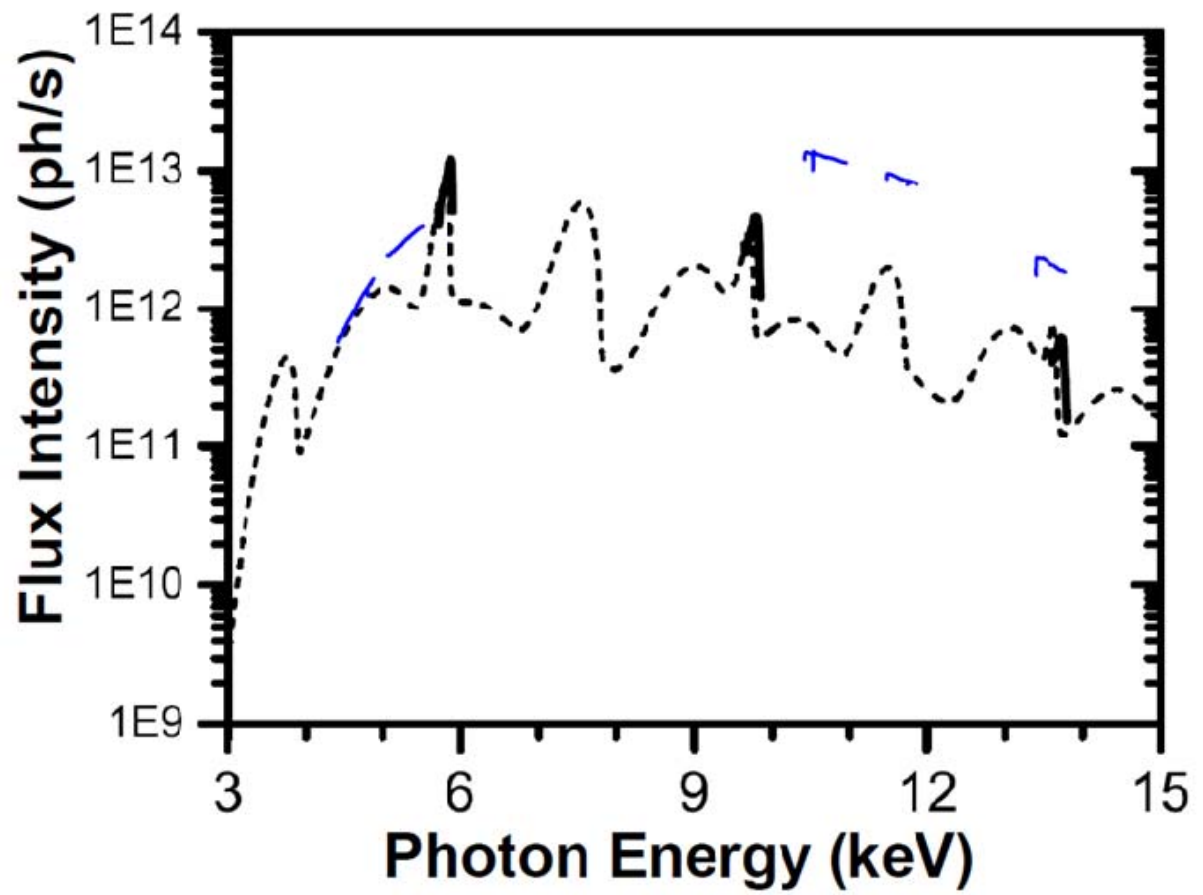


Fig. 3.7: A comparison between the theoretical (dashed curve) and the measured flux curves without undulator gap optimization (black solid curve) and with undulator gap optimization (blue solid curve) source: ⁸⁸.

3.5 Femtosecond x-ray generation using the synchrotron-based laser-electron slicing technique

Various efforts have started for building free electron laser (FEL) facilities, with the goal of producing wavelength in the Å range and pulse duration ~ 100 fs. Though such facilities provide high brightness (10^{20} photon/pulse) and short pulse duration, the cost for building it is very high. Zholents *et al*⁹² proposed a method for generation of femtosecond synchrotron x-ray pulses using a femtosecond laser to modulate the energy of electron bunch, which was demonstrated by Schoenlein *et al*⁹³ at the ALS, and now has been implemented at BESSY and the SLS. Although the brightness of this fs x-ray source is much lower than that of future FELs, it offers comparable pulse duration and, more importantly, the system can be installed as an add-on at an existing synchrotron at a much lower cost than FEL. This fascinating add-on has been installed at the SLS by the FEMTO group using the microXAS beamline as an extraction path for fs x-ray radiation.

The basic idea (Fig. 3.8) of the method is to use the high electric field of a femtosecond laser pulse to modulate the energy of an electron bunch that is traveling inside a wiggler (modulator) to “slice” out a number of electrons with the same pulse duration as the laser. When the energy of sliced electron bunch is several times larger than the electron beam energy spread, it can be

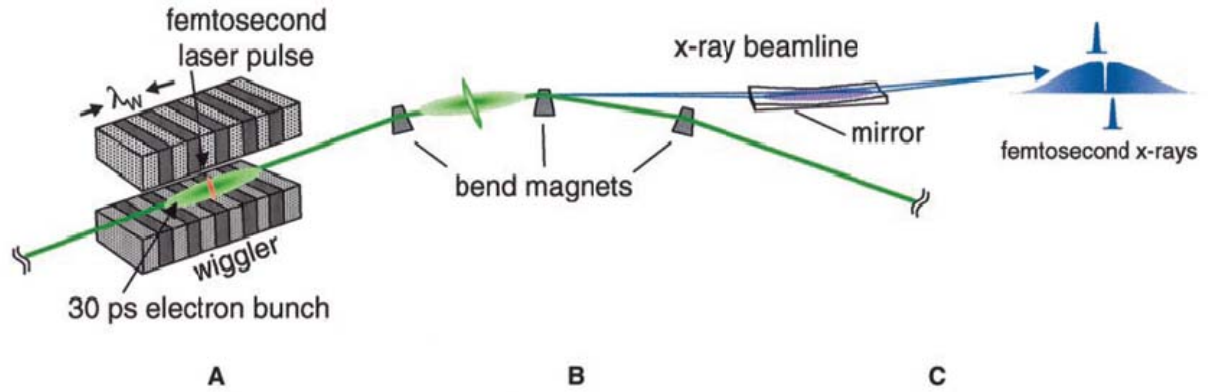


Fig. 3.8: Schematic laser slicing method for femtosecond synchrotron. (A) laser interaction with electron bunch in a resonantly tuned wiggler. (B) transverse separation of modulated electrons in dispersive bend of the storage ring. (C) Separation of femtosecond synchrotron radiation at the beamline separation image plane. Source: ⁹³

spatially separated from the unsliced beam at a bending magnet after the modulator. This sliced beam then goes through a radiator (bending magnet or undulator), and emits fs x-rays. The interaction between the laser and electron beams is nicely described by the theory of a small signal gain FEL amplifier ⁹⁴. Under the periodic magnetic field of a wiggler an electron beam can resonantly interact with the optical electric field of the laser if the wiggler is tuned such that the peak of spontaneous emission of the electron beam coincides with the wavelength of the horizontally polarized laser. In this case the interaction part of the electron beam will gain or lose energy depending on the phase difference of laser and electrons (electron is accelerated or decelerated depending on the optical phase seen by each electron at the entrance of the wiggler). As a result, two subsets are sliced out from the original electron beam corresponding to a gain and a loss of energy. The central wavelength of spontaneous emission of a wiggler is given by ⁹³:

$$\lambda_s = \frac{\lambda_w (1 + K^2 / 2)}{2\gamma^2} \quad (3.6)$$

where λ_w is the period of wiggler, K is the deflection parameter, given by Eq. 3.2. The resonance condition is $\lambda_s = \lambda_L$ with λ_L being the laser wavelength. Next to this condition, the transverse mode of the laser must match the transverse mode of the wiggler emission and the laser bandwidth must be comparable to the wiggler radiation average over the transverse mode. With these conditions, the modulated energy of the electron beam is governed by ⁹³:

$$\Delta E \cong 2 \left(A_L A_w \frac{M_w}{M_L \sqrt{2}} \eta_{emit} \right)^{1/2} \cos \phi \quad (3.7)$$

where A_L is the laser pulse energy, M_w is the number of wiggler periods, M_L is laser pulse length in optical cycles, $A_w \cong 4.1\alpha h\nu_L K^2 / (2 + K^2)$ is energy spontaneously emitted by a single electron when passing through the wiggler ⁹³, α is the fine structure constant, h is Planck's constant, and ν_L is the laser frequency. The interaction between laser and electron results in coherent radiation emission in the far infrared, so-called THz light. The origin of the radiation can be understood in two ways: (i) the electron beam absorbs laser energy and emits THz light, (ii) the sliced electron which has femtosecond duration can be translated to a wavelength in the μm range via the Fourier-theorem equation $\Delta t \Delta \lambda \approx \lambda^2 / 2\pi c$ ⁸⁶ where Δt and $\Delta \lambda$ are the pulse duration and spectral bandwidth, respectively. This THz light is a very useful signal for optimizing the spatial and temporal overlap of laser and electron beams ⁹⁵. It is also used to monitor online the fs x-ray fluxes.

A 'slicing' system consists of two main parts, the laser system and the insertion device.

3.5.1 Laser system

A femtosecond oscillator (repetition rate of 100 MHz, pulse duration 30fs, average power 500 mW, wavelength 795 nm), is synchronized to the RF master frequency of the ring (500MHz) with a jitter estimated to be < 2 ps. The output of the oscillator is split into two

branches to seed laser amplifiers, called “phase I” and “phase II”. The phase I regenerative amplifier (115 fs, 1 kHz, 2.1 mJ, 800 nm) is sent to the experimental station via a 22 m vacuum pipe for sample excitation. The phase II laser is a two stage amplifier, after the first regenerative amplifier stage the stretch output pulse is further amplified in a symmetrically pumped 2-pass, the output pulse is then compressed to provide 50 fs, 2kHz, 3 mJ at 805 nm. To maintain the phase II laser in a good mode (nearly diffraction limited with $M^2 \leq 1.4$) for slicing, the Ti:sapphire crystal in the 2-pass amplifier is cryogenically cooled to 45 K. Before being sent to a long evacuated transport tube, the laser is expanded to 12.7 cm diameter to avoid nonlinear interaction with optical components. The laser beam is then slightly focused into the wiggler over the 50 m distance resulting in a Rayleigh length of 0.6 m, beam waist of 490 μm for electron energy modulation. The optical alignment is done using several motorized mirrors, one of them is inside the ultra high vacuum (UHV) of the storage ring. The beam position is monitored by a CCD camera that looks at a residual laser leakage through one of the mirrors. The beam position is automatically corrected via feedback loop.

3.5.2 Insertion devices: modulator and radiator

The insertion devices for laser slicing fs synchrotron generation are installed in the 11 m long straight section 5L of the SLS storage ring (Fig. 3.9). The electron beam interacts with the laser in the modulator (wiggler: $B_{w,\text{eff}} = 1.98$ T, minimum accepted gap $g=11$ mm, $\lambda_w = 138$ mm, $N_w = 17$ periods) that is tuned to 805 nm, to generate a femtosecond slice of energy modulated electrons. The sliced electrons pass through a chicane 3-dipole for spatial separation from the core beam and then being refocused by triplet before radiating by passing through the radiator (in-vacuum undulator $B_{u,\text{eff}} = 0.92$ T, $g= 5\text{mm}$, $\lambda_u = 19$ mm, $N_u = 96$ periods). There are several fast-orbit feedback correctors (FOFB-corrector) and an insertion device feedforward (ID-FF) to correct the electron beam orbit. The laser beam exiting the modulator is transported to a diagnostic hutch, where together with the THz signal the slicing process is optimized and monitored. When the modulator magnetic field is tuned to the optimal interaction at the slicing laser wavelength, the laser induces an energy modulation estimated from Eq. 3.7 to be $\Delta E / E \sim 1\%$ ⁹⁵ (electron energy of the ring $E=2.4$ GeV, thus modulated energy $\Delta E \sim 24$ MeV) with laser optical cycles of 18 and pulse energy 2.5 mJ. For this energy modulation, the chicane provides a spatial (± 2 mm) and angular (± 0.5 mrad) horizontal

separation of the sliced beams at the radiator center. The radiation from the core beam is blocked by a slit system, allowing only emission from the higher energetic satellite beam to pass. The radiation from the core beam is suppressed by 1000:1 by the photon absorbers and adjustable slits. The background is mainly limited by the so called ‘halo’ emission, which is the emission from the incomplete relaxation of the modulated electron beam from the previous laser-electron interaction 1ms ago ⁹⁶. The ratio of signal to halo is ~10:1. The femtosecond x-ray flux measured with an avalanche photodiode is $2 \times 10^5 (6 \times 10^4)$ photons/s in a 0.1% bandwidth at 5 (8) keV, for 2 mJ slicing laser pulse energy and 4 mA camshaft current.

As mentioned above, the far-IR coherent radiation from the modulated electron is used to optimize the spatial and temporal overlap of laser and electron beam. The THz signal is collected by an InSb bolometer cooled down to 4.2 K. Fig. 3.10a shows the THz and fs x-ray intensity as a function of modulator gap. The central wavelength of wiggler radiation, converted from the gap size is displayed in the top scale of the graph. The fs x-ray is red shifted because only radiation from a subset with energy gain is accepted by the first mirror of the beamline. Similar behavior is also observed when fs x-ray and ‘halo’ radiation signal are measured as a function of radiator gap (Fig. 3.10b). The fs x-ray peaks at a smaller gap than the ‘halo’. The x-ray pulse length and timing stability are characterized by differential diffraction signal from photoexcited bismuth. Deconvoluting the dynamics curve with the pump pulse duration and nonlinear geometry yields an effective x-ray pulse length of 140 ± 30 fs FWHM ⁹⁵. Time zero of the time trace curve is determined to be drifted by 30 fs rms over 5 days.

SLS FEMTO Source: Hard X-Rays

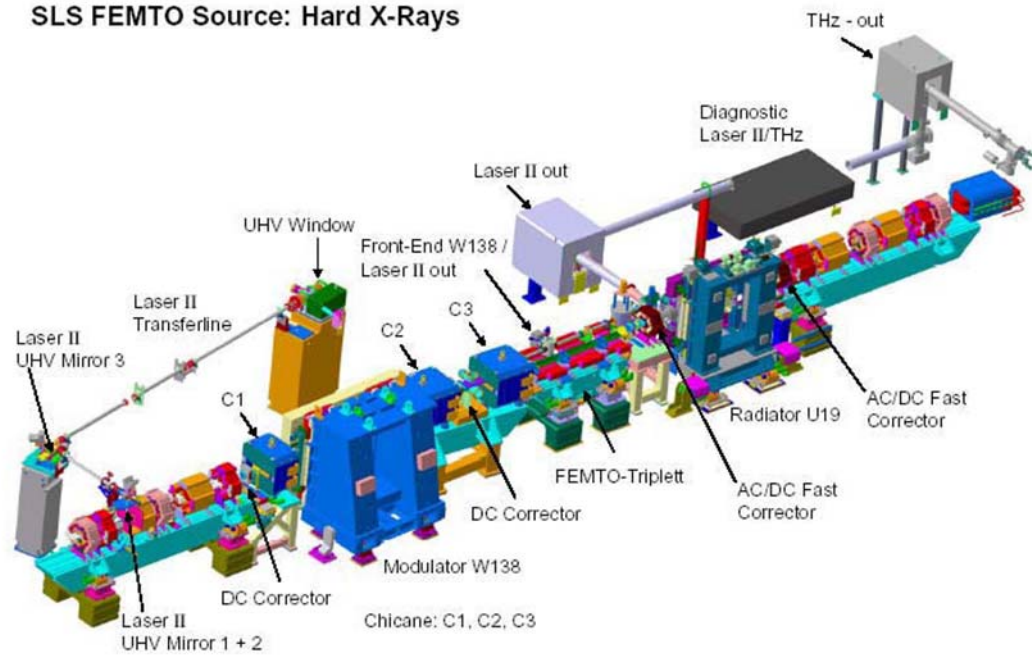


Fig. 3.9: Engineering layout of the FEMTO source: Laser II transport line, slicing spectrometer installed in a long (11 m) straight section, and ports for laser and THz diagnostic. Source: ¹²⁹

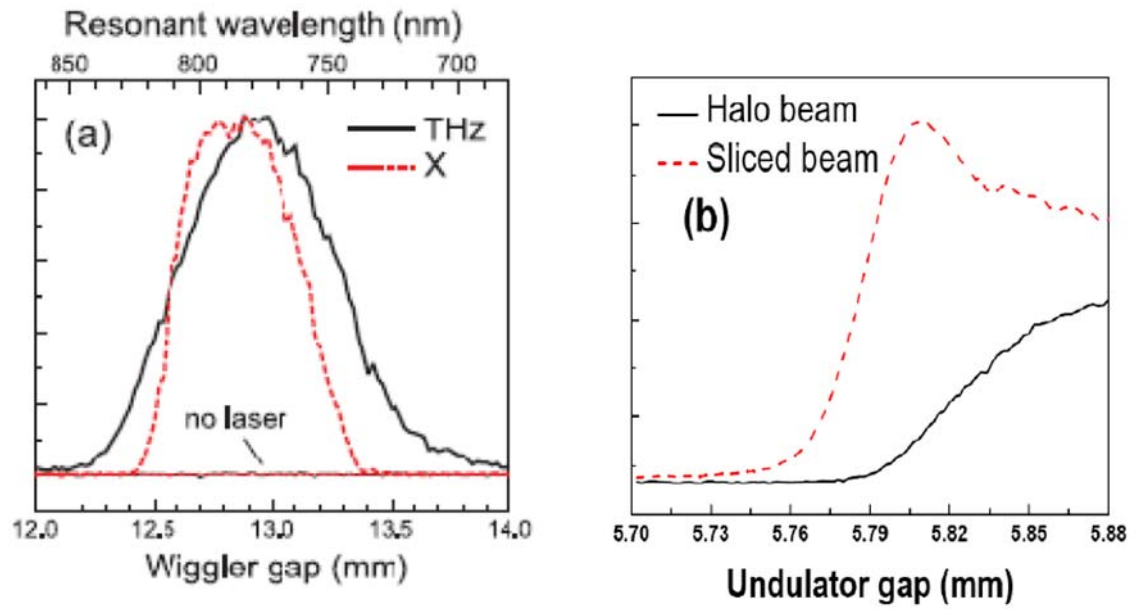


Fig. 3.10: (a) the laser-electron interaction is tuned by changing modulator gap. THz and x-ray signal are monitored. The resonant wavelength for x-ray is red shift because only radiation from electron with 0.6-0.8% energy gain is accepted by the first mirror in the beam line. Source: ⁹⁵, (b) The sliced x-ray peaking a shorter gap compare to the halo beam because the sliced electrons are at higher energy than the halo.

3.6 Picosecond- resolved XAS setup

The picosecond-resolved XAS measurements of aqueous iodide were carried out at microXAS beam line at the SLS. Description of the beamline and details on the experiment were reported previously⁸⁸. In this section, we briefly review and emphasize the experimental parameters. The samples were prepared by dissolving sodium iodide (NaI) with 99.9% purity (Aldrich-Sigma) into distilled water. Different concentrations, 50 mM, 100 mM, 200 mM, and 500 mM were measured. The samples were circulated in a free flowing liquid jet thickness of 200 μm to avoid subsequent products of photochemistry. Optical absorption (UV-VIS) of the samples were measured frequently, old samples were replaced with fresh ones when the UV-VIS show the trace of poly-iodide, corresponding to a concentration of < 1 mM of I_3^- .

The experimental setup for laser pump-picosecond x-ray probe is illustrated in Fig. 3.11. The transient absorption of iodide L_1 and L_3 edge are measured using 3rd harmonic of radiator with energy resolution of ca. 0.8 eV, provided by double crystal monochromator (DCM) Si (111). Monochromatic x-ray beam come out from DCM is focused into the sample by Kirkpatrick-Baez (KB) mirror which consists of two Rh coated mirrors for horizontally and vertically focusing. The x-ray foci of 60x120 μm (vertical x horizontal) at the sample position, located at ca. 50 cm from the KB mirror, was measured by scanning a 50 μm pinhole. The samples and detectors are kept in a chamber, flushed with He to avoid losing x-ray flux by the absorption in air. The ring was operated at 350 mA with cathode current of 2 mA, providing a x-ray flux of ca. 1000 to 6000 photons/pulse over the two edges. Pumping laser at 400 nm is derived from a doubling BBO crystal of fs laser (115 fs FWHM, 1 kHz, 2.1 mJ, 800 nm). The laser spot size at sample position was 180 x 155 μm (vertical x horizontal), giving fluence of 1.7 J/cm² for 50 mM sample and 1 J/cm² for other concentrations. Spatial overlap of laser and x-ray were performed by means of a 50 μm pinhole. The x-ray beam position on the samples is traced by the pinhole which was identically mounted as the sample, and the overlap was done by centering the laser beam on the pinhole. To ensure a best spatial overlap, laser and x-ray transmitted intensity through the pinhole are scanned against the pinhole positions, the laser point is shifted by a motorized mirror such that its center positions is coincided with that of x-ray. Time delay between x-ray and laser is electronically controlled by a phase shift feedback loop. Briefly, the device controls the cavity length of the laser oscillator which is synchronized

to the RF master of the ring, the regenerative amplifier amplifies the oscillator pulse while keeping its phase unchanged ⁹⁷. Temporal overlap was performed using a fast silicon photodiode (rise time 750 ps). Camshaft pulse signal was monitored by a fast oscilloscope 4 GHz, the middle of the rising edge was marked before the photodiode switched to display the pump laser pulse, the process is repeated for laser. The time delay was controlled such that both markers are overlapped. The time zero can be achieved within an uncertainty of ± 100 ps. The measurement were performed in both transmission and fluorescence mode. X-ray signal, detected by silicon avalanche photodiode (APD) C30703F, EG&G is amplified by FEMTO amplifier before being integrated by electronic boxcar. The signal from camshaft pulse was integrated using an electronic gate with pulse width of 20 ns at frequency of 6 kHz from the boxcar. The probe signal was recorded at the laser excitation time and at 500 μ s later, where the sample is in static state. To account for the background and long time drift of the signal, ‘zero’ count rates were recorded at two positions between the camshaft and the multibunch. Details of the data acquisition techniques are reported by Gawelda ⁸⁸. The transient absorption of the

samples are calculated by $\Delta A = \ln\left(\frac{I_{unpump}}{I_{pump}}\right)$, where I_{unpump} and I_{pump} are transmitted intensity of

unpumped and pumped sample, respectively. Energy-resolved measurements were also carried out with different energy steps depending on scanning energy range, the minimum step was 0.1 eV, largest steps of 5 eV are in the EXAFS region. The transient absorption was calculated for every scan before the weighted average is performed at each energy point ⁹⁸.

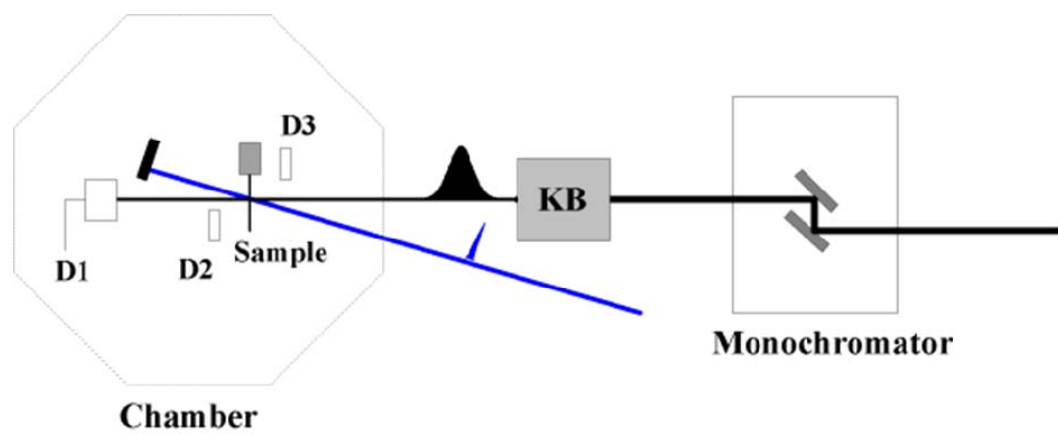


Fig. 3.11: The schematic of experimental setup for ps-resolved measurement in dual mode. D1-3 are avalanche photodiodes.

3.7 Femtosecond-resolved X-ray Absorption

Laser pump-fs x-ray probe experiments are carried out at the same experimental station as the ps-resolved XAS measurement. The experimental technique is similar to the one described above except that the pump-probe synchronization is inherently established, the time delay can just be controlled by moving a translation stage to change the optical path of the pump beam (Fig. 3.12). On the other hand, the measurements become more difficult due to extremely low flux of fs x-ray. Femtosecond pink beam (polychromatic beam) is monochromatized by a double crystal Ge (111) monochromator giving an energy resolution of ~ 2 eV at L_1 and L_3 edge of iodide. The beam is then focused in both dimensions to the sample position by KB mirror, resulting in a spot size of $50 \times 100 \mu\text{m}$ (vertical \times horizontal). At iodide the L_3 edge, the x-ray flux at the sample position under 1 atm He is 20 ph/pulse: sliced beam and 2 phs/pulse: halo beam, at L_1 edge, 33 ph/pulse: sliced beam and 1 ph/pulse for halo. The x-ray probes the sample transmission at 2 kHz. The measurements were done in transmission mode only, since fluorescence signal is undetectable at such a low incident flux. Two-photon excitation is performed by 400 nm fs laser with fluence at sample position being 0.8 J/cm^2 . The laser spot size is $\sim 200 \times 200 \mu\text{m}$ at sample position. To attempt to slightly compensate for the low signal-to-noise due to the low flux, only high concentration samples, 0.43 M, are measured, degraded samples are regularly replaced to ensure a negligible amount of Γ_3 in the sample. Optical measurement shows that at this concentration, only a negligible amount of Γ_2 molecules is formed before 20 ps. The signal from the transmission APD feeds the two boxcars sequentially, one for sliced beam and the other for halo beam. The halo signal derived from the pulse just before the sliced one is electronically integrated by the boxcar. Its count rate is considered as a background in data analysis. The data acquisition is done in the same way as in the picosecond experiment. In addition, the background drift is regularly measured by entirely blocking x-ray although this was already done in situ by measuring the zero intensities. The time delay in energy scan is finally calculated by compensating the change of x-ray path length (due to the rotation of the monochromator crystal) with the delay line which controls the pump laser path length.

The success of any pump-probe experiment strongly relies on the stability of spatial and temporal overlaps. In this type of experiment, the spatial overlap is much more difficult than

picoseconds setup because the monochromatized probe beam cannot be monitored by phosphorescence or burning paper. We used a technique based on knife-edge scan to initially mark the x-ray position. Two blades are mounted to make a right angle in a holder that is identical to the jet nozzle. X-ray is scanned so that the center of the differentiated curve of the knife edge signal is located at the corner of the blades. This corner is marked by the attenuated pump laser before the blades are replaced by a 100 μm pinhole. The next procedure is similar to picosecond-resolved experiment. Fig. 3.13 shows the x-ray and laser profile obtained by differentiating the knife-edge curve. The timing overlap is done using the more intense pink beam (entire SR) with a fast photodiode. The time zero is then post corrected for the beam path length difference when the monochromator is put into place. Once overlaps are secured, we start searching for a signal at a selected energy where we previously found a large signal in the ps-resolved measurement. Since the probe flux is extremely low, a conventional time scan would take long time to find the signal and especially time zero. A more efficient way for finding time zero signal is a so-called binary search. A range of time which possibly contains the time zero is divided into two regions. A difference in transient absorption of two ends of a region is measured. The regions which show a zero signal indicates that both measured time points are at either before time zero or after time zero, and should be excluded. The time zero search continues on the other region. The process is repeated until the time zero uncertainty is about one ps.

During the actual data collection, the laser position on the sample is monitored online by a beamprofiler that collects residual transmitted laser through the last mirror that direct the pump laser into the chamber. We set the beamprofiler at the same distance to the mirror as does the sample so that the beam size on the beamprofiler is exactly the one on the sample. At the same time, the THz and fs x-ray signals are also monitored online and can be optimized whenever necessary.

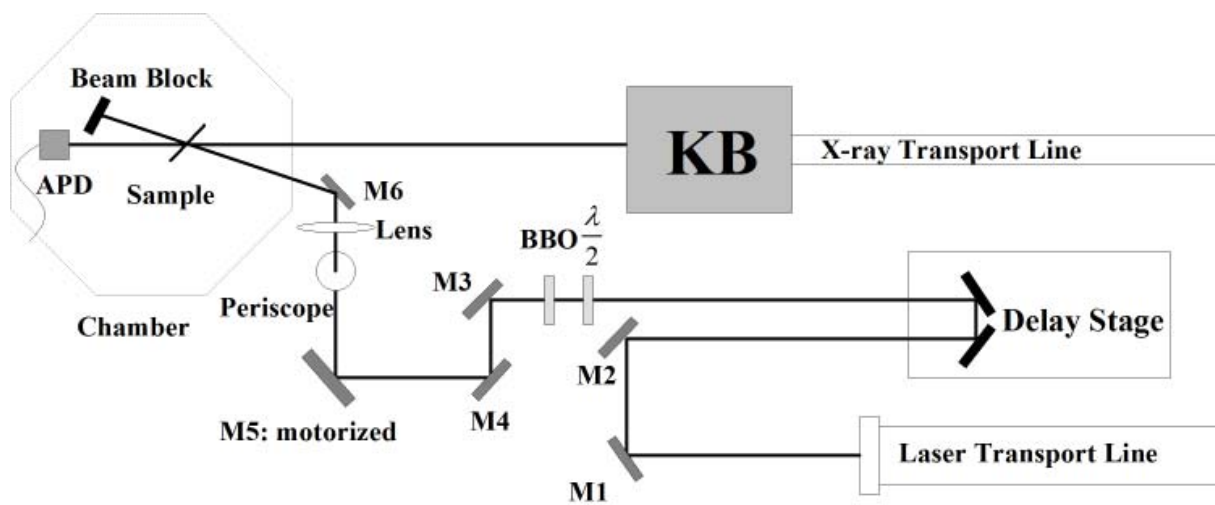


Fig. 3.12: Experimental apparatus for laser pump-fs x-ray probe. M1-5 are dielectric coated mirrors with high reflectivity ($R > 99\%$), in which M5 is mounted on a motorized mirror mount.

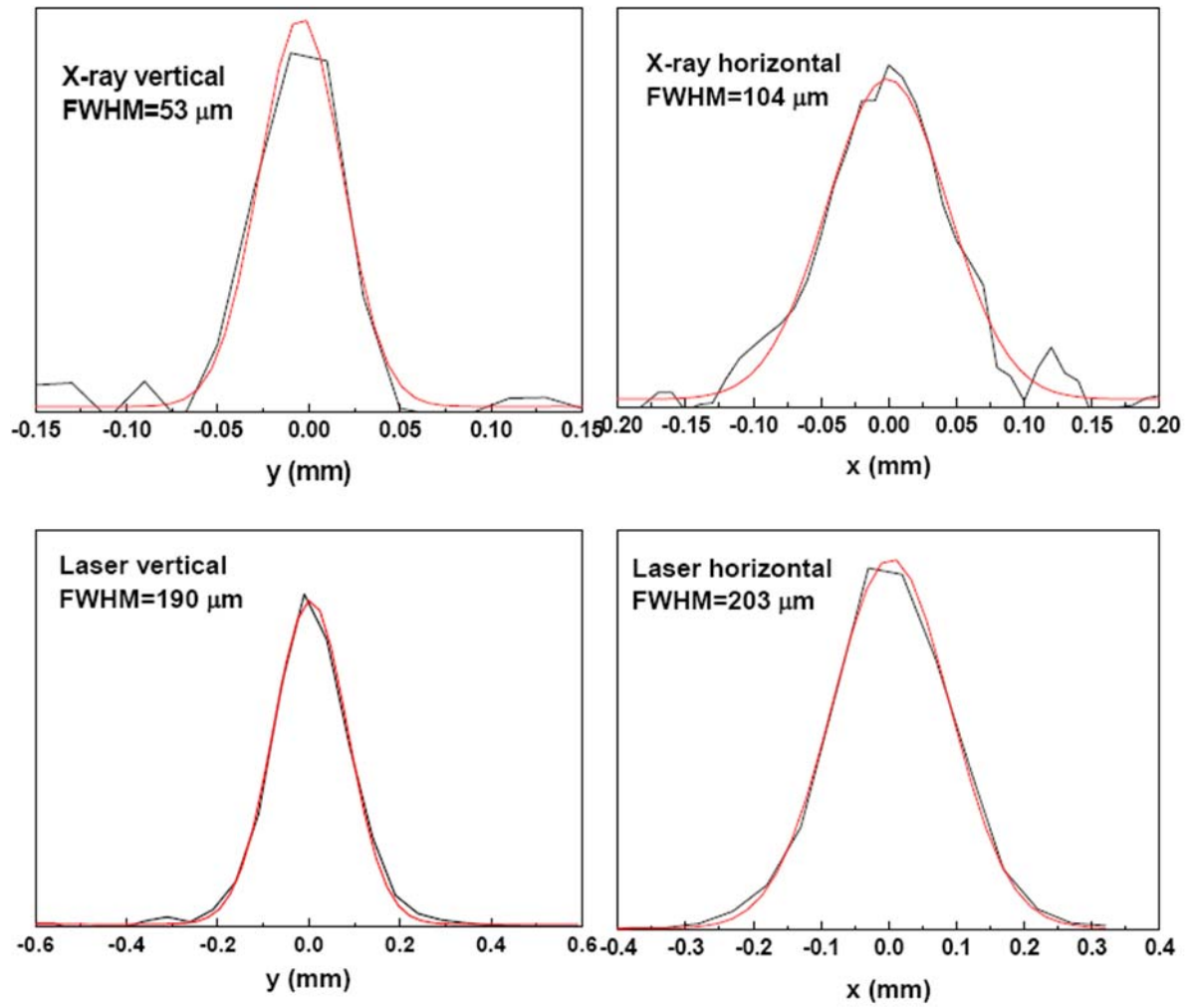


Fig. 3.13: Profile of x-ray and laser through knife-edge scan (black curve), the red curves are Gaussian bestfit the profile.

3.8 Femtosecond All Optical Pump-Probe Setup

3.8.1 400 nm pump white light continuum and 800 nm probe

The optical femtosecond transient absorption of aqueous iodide was investigated under one and two-photon absorption with pump pulse at 240 nm and 400 nm, respectively. The transient absorptions resulted from the femtosecond excitation were probed with the 800 nm, 240 nm, 580 nm and broad band white light continuum 340 nm-650 nm. Fig. 3.14 sketches experimental setup for 400 nm pump white light continuum probe. A fundamental pulse from Ti:sapphire laser (800 nm, 120fs, 1kHz, 0.8mJ) is split into two beams for the pump and the probe branches at a intensity ratio of 9/1. The pump beam is frequency doubled to 400 nm by a BBO crystal (cut angle 29 degree). The repetition rate is reduced to 500 Hz by a chopper before focusing the beam onto the sample. The probe beam enters a delay line mounted with a retro reflector and is subsequently focused into a 2 mm thick CaF₂ window for white light continuum generation. The white light continuum is collimated by a silver coated parabolic mirror before being focused by another parabolic mirror to the sample. We used the parabolic mirrors instead of lens to reduce the group velocity dispersion of the white light. The transmitted probe beam sent to a monochromator, is dispersed by a 150 l/mm grating, and recorded by a diode array (DA 512 pixels). The wavelength is determined by the light position on the diode array. The DA detector records full 2D transient spectra (wavelength and time), so inherently the temporal and spectral information is acquired simultaneously at 1 kHz. Wavelength calibration is done by using an Hg emission line.

The probe beam enters the sample at twice the repetition rate as the pump beam to allow measuring transient spectra on a shot-to-shot basis. The transient absorption is calculated by

$$\Delta OD = \log\left(\frac{I_{unpump}}{I_{pump}}\right) \quad (3.8)$$

where I_{unpump} and I_{pump} are the transmitted probe spectra without and with pump laser, respectively. Note that for the transient XAFS we used the different definition for the signal via

$\Delta A = \ln\left(\frac{I_{unpump}}{I_{pump}}\right)$, which is related to ΔOD via $\Delta A = 2.3 \Delta OD$. The pump beam size is ~ 250

μm and that of the probe is $\sim 60 \mu\text{m}$. The sample is circulated in a free flowing jet (thickness $200 \mu\text{m}$) at a speed of $\sim 0.5 \text{ m/s}$. For the given pump beam size and repetition rate this flowing speed ensure a fresh sample at every pump shot.

The solvated electron is probed at 800 nm . The above described setup can be easily turned into a 400 nm pump- 800 nm probe setup by removing the CaF_2 plate and the parabolic mirrors. The focal length of the lens is adjusted to have a proper beamsizes on the sample.

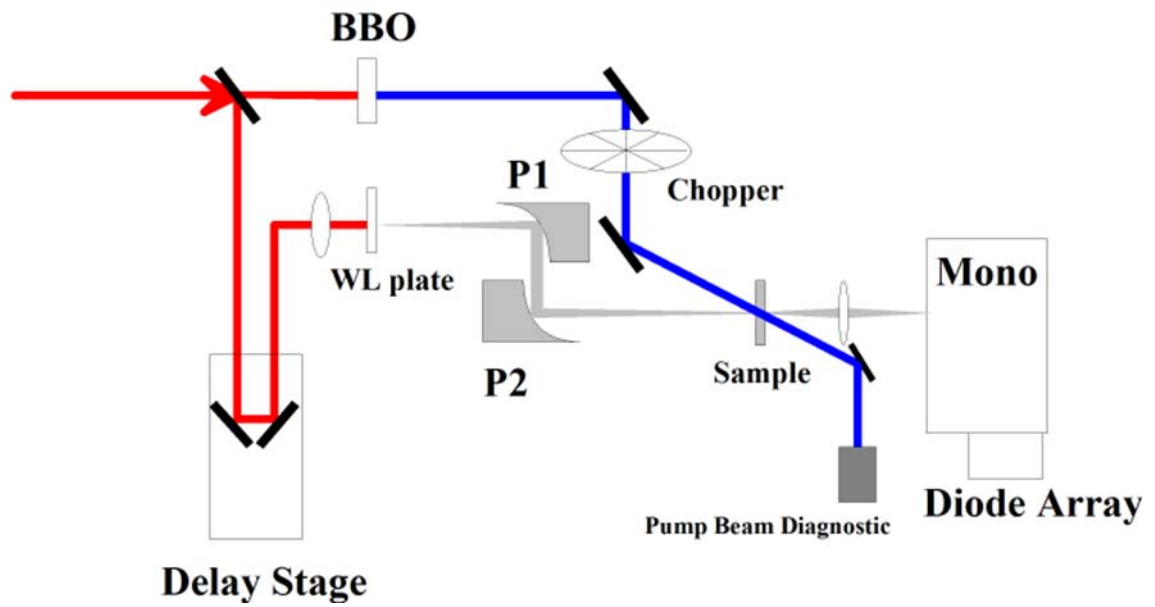


Fig. 3.14: Experimental setup for two-photon excitation using 400 nm and broadband white light continuum probe.

3.8.2 400 nm pump 211 nm probe

In order to avoid temperature effect on the kinetics of bleached iodide, we probe the sample at an isosbestic point, 211 nm upon 400 nm excitation (Fig. 3.15). This measurement was performed at the optical pump-probe setup in PSI, where a fundamental Ti: sapphire laser pulse (115 fs FWHM, 1 kHz, 2.1 mJ, 800 nm) is split into two beams to make a pump and a probe arm. The 211 nm is created by mixing a laser at 287.3 nm from TOPAS (collinear optical parametric amplifier of super-fluorescence) with fundamental 800 nm in a 59.2 ° cut BBO crystal. The pump beam after the delay line is frequency-doubled by second harmonic generator BBO crystal, following a reducing repetition rate to 500 Hz by mean of chopper. The pump and probe beam is focused onto sample at $\sim 200\ \mu\text{m}$ and $\sim 70\ \mu\text{m}$ in diameter, respectively. The 211 nm beam is split into a probe beam which goes through the sample and a reference beam which pass by the sample to correct for the intensity fluctuation of the probe beam. To avoid scattering from the pump beam, the reference and the probe beam are monochromatized at 211 nm before being detected by photodiodes. To correct the transient absorption for the pump fluctuation another photodiode is implemented to record its intensity. The pump beam is also chopped to 500 Hz for the same reason as stated above.

3.8.3 400 nm pump 240 nm probe

Fig. 3.16 depicts the setup for 400 nm pump 240 nm probe. The 240 nm probe is generated by TOPAS which was partially seeded by a fundamental 800 nm fs laser. The remaining intensity of the fundamental beam goes through a delay stage before being doubled in frequency to create 400 nm beam for excitation. A reference beam is separated from the probe beam to correct for the probe fluctuation. A monochromator is set to 240 nm so that the photodiodes behind it can record the probe and reference intensity.

3.8.4 240 nm pump 800 nm probe

Probing solvated electron from single photon excitation experiments are carried out. The pump at 240 nm is generated by TOPAS with incident femtosecond laser at 800 nm, 1.6 J/pulse. A part of the fundamental 800 nm is separated by a beamsplitter before entering the TOPAS for probing the electrons. The 800 nm beam is delayed with respect to 240 nm pump. The rest of the setup is similar to the above 400 nm pump 240 nm probe.

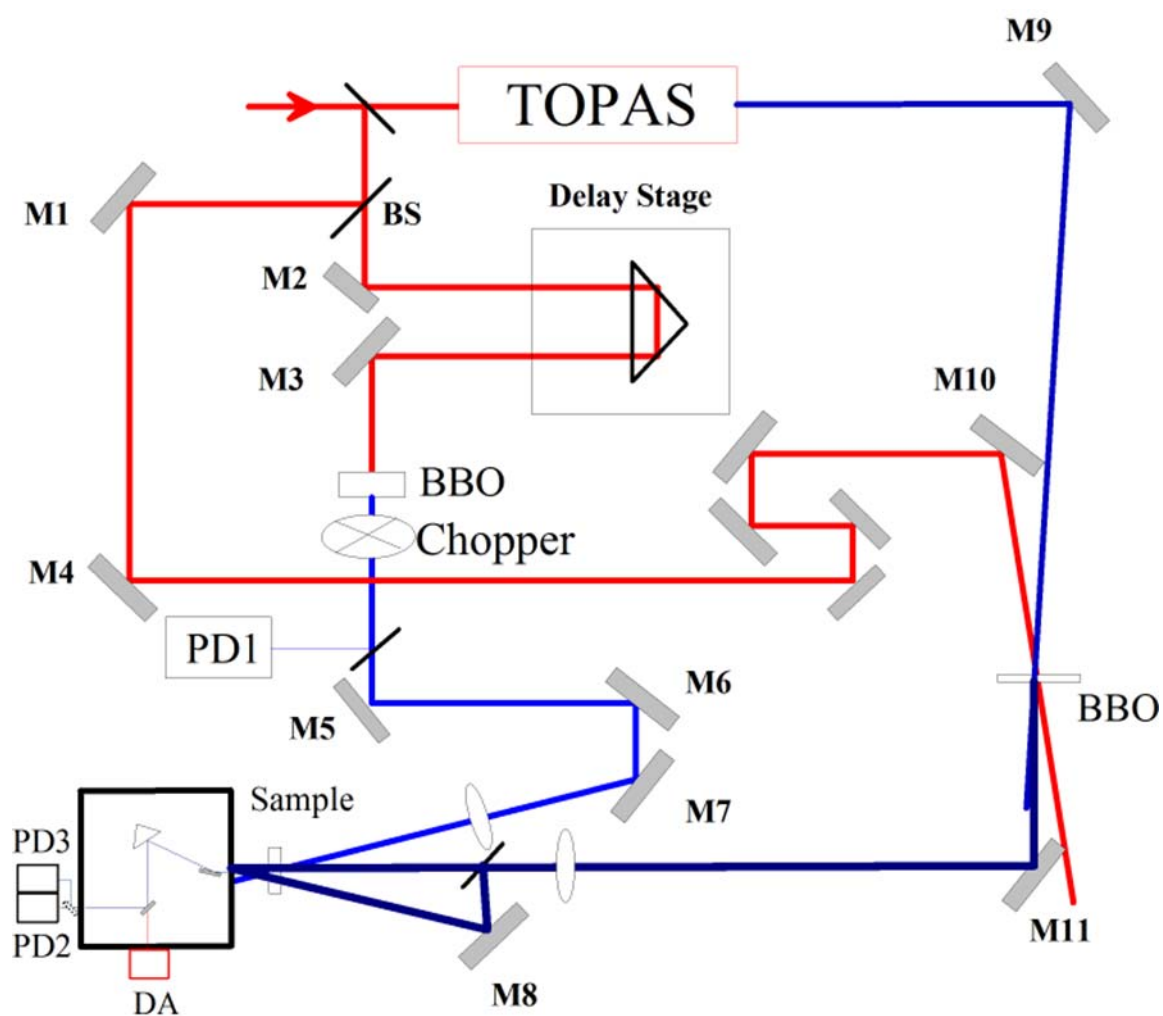


Fig. 3.15: Experimental setup for two-photon excitation using 400 nm and probing the bleach iodide at 211 nm

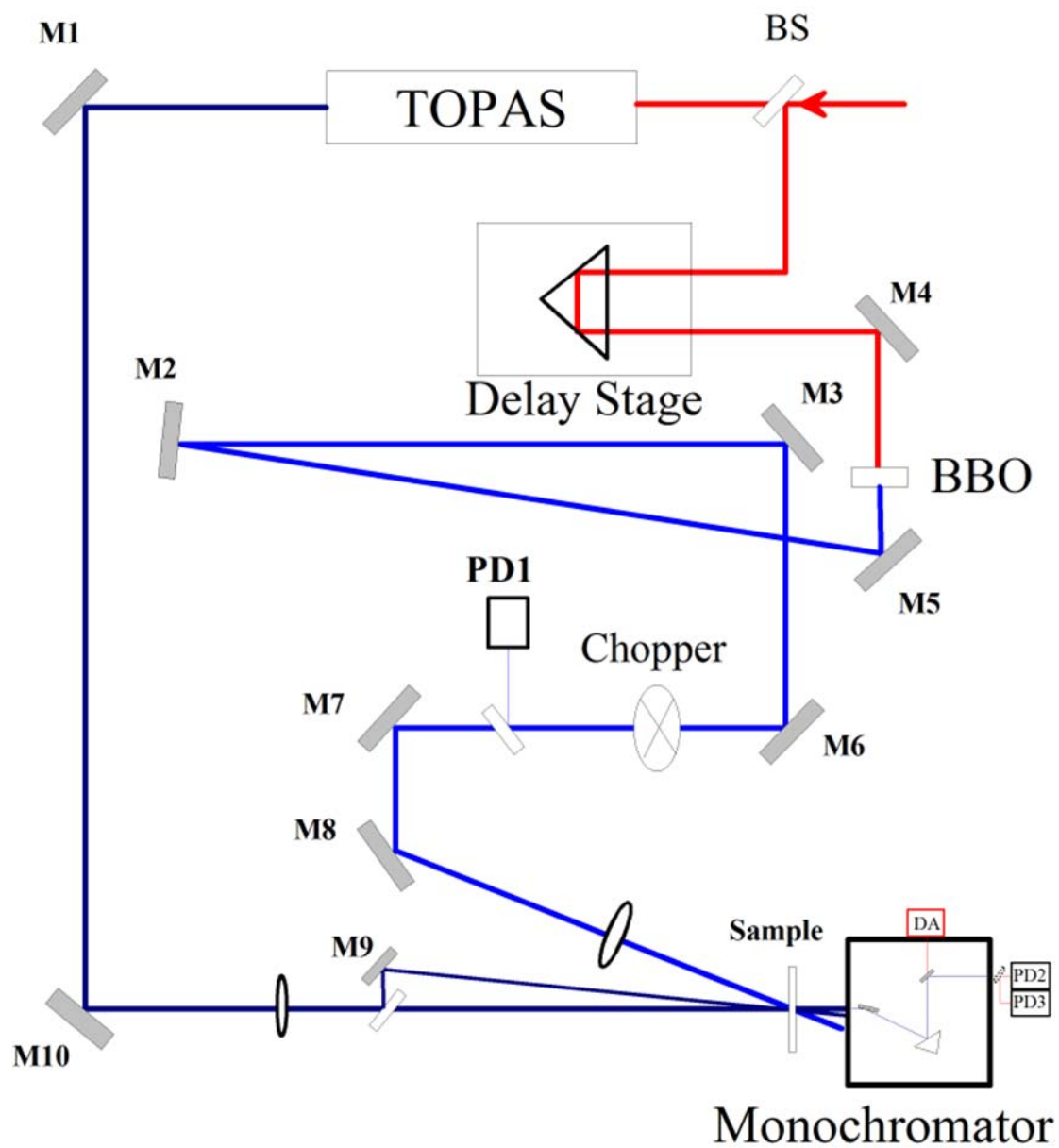


Fig. 3.16: Experimental setup for 400 nm pump 240 nm probe

Chapter 4 Structural Analysis of Iodide Static Solvation Shell

In this chapter, we present EXAFS data analysis at L_3 edge of aqueous iodide. The theoretical structure derived from classical MD, DFT and quantum mechanics/molecular mechanics (QM/MM) simulation techniques are assessed and compared to the experimental data. The details are presented in the subsequent article. In the following we introduce the analysis of the EXAFS at the L_3 -edge of iodide. The EXAFS analysis is carried out using a peak fitting approach (see section 2.1.3). An iterative structural optimization is performed by a Matlab program that uses GNXAS⁹⁹ for the calculation of EXAFS signal.

4.1 Data reduction

In order to extract structural information, the raw absorption data at the iodide L_3 edge was reduced to create EXAFS signal via a standard data reduction procedure, which includes the following steps:

1. Pre-edge and post-edge normalization: The pre-edge is normally a linear function, while the post-edge is modeled with a polynomial function. The raw data is normalized to the edge step (difference between post- and pre-edge at the inflection point (edge step)).
2. Convert the spectra from energy to k-space using Eq. 2.1
3. The EXAFS $\chi(k)$ function is obtained after subtracting the so called atomic background. This is modeled with a curved step function including a number of polynomial functions of order of two to four in the post-edge region (or simply: determined by the difference between the pre- and post-edge functions above). These functions should exclude the oscillatory pattern due to the interference effect in the EXAFS; otherwise one would remove the vital structural information contained in the data. For display purposes the oscillating features at larger k can be amplified by weighting $\chi(k)$ with n^{th} power of k. This should have no implication in interpreting these oscillations, if the fitting algorithm can use the error on each data point. In practice, however, the EXAFS analyzed without taking the individual errors into account, and then this weighting does have implications in the interpretation.

Data reduction was performed using Pyspline¹⁰⁰ a versatile program for XAS that allows users to choose suitable regions to freely place spline functions to model pre and post-edge

curves interactively. The post-edge L_3 XAS was modeled with two segmented cubic spline functions. The inflection point at the L_3 edge roughly determines its ionization threshold. The XANES region of L_3 is fitted with a Lorentzian-shaped curve, which should model the shoulder in the rising edge, and a step function whose edge position determines the Fermi level, which is somewhat below the ionization potential. The final EXAFS functions have proven to not be sensitive to number and order of the polynomial functions, thus assuring us that the structural content is preserved in the treated data. It is important to notice that even the XANES spectra of the L_3 edge contain more geometric structural information than the L_1 edge due to its larger absorption cross section, originating from a larger number of electron in the p orbital.

4.2 Refinement of radial distribution function

In order to acquire information about the caging solvent shell structure, the pair radial distribution functions of I-O and I-H are optimized to fit the experimental EXAFS. A valid function to model the radial distribution function of I-O and I-H is given by Eq. 3.7. The two-body scattering dominated EXAFS signal ⁶⁹ can be then calculated (via Eq. 1 in the attached article) using the modeled $g(r)$.

Although GNXAS can fit a raw absorption spectrum to refine $g(r)$ as it has been done for aqueous bromide ⁷³, it does not support fitting directly a EXAFS spectrum. We used a Matlab script that employ GNXAS for $\chi(k)$ calculation. The parameters of the $g(r)$ are adjust to best fit the experimental $k\chi(k)$. The initial guess parameters for

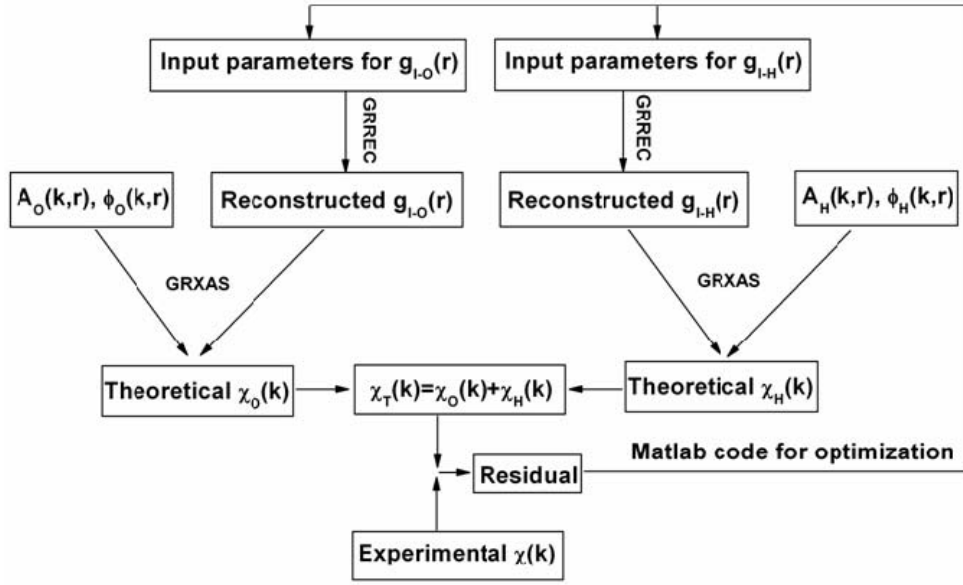


Fig. 4.1: Flowchart of fitting procedure for $g(r)$ refinement, GRREC and GRXAS are programs in GNXAS package.

the $g(r)$ are taken from a single peak decomposition of QM/MM $g_{I-O}(r)$ and $g_{I-H}(r)$ to the Eq.2.7. The symmetric factor $\beta_X(X: O,H)$ must be larger or equal to zero in the first solvation shell¹³¹. Therefore the lower limit of β_X is set to zero. The scattering amplitude and phase shift, as well as the non structural parameter S_0^2 are kept the same as the ones used in regular EXAFS calculations for CMD, QM/MM and DFT (see attached article below). The flowchart of this procedure is illustrated in Fig. 4.1. The RdF's functions for I-H and I-O are reconstructed from the input parameters via GRREC program. These functions together with the scattering amplitude, $A_X(k,r)$ ($X=O,H$), and the phase shift, $\phi_X(k,r)$ ($X=O,H$), are then be used to calculate the theoretical EXAFS signal. The total $\chi_T(k)$ is finally compared to the experiment by Eq. 3 in the attached article to find the sum of squared error (SSE) after a fit for ionization threshold to the experiment. Note that this fit sequence does not include the measured error to calculate the SSE, and for this reason the k-weighting is important. The SSE values are minimized by iteratively adjusting the input parameters for each $g(r)$. Once the fit has converged, the parameters and their uncertainties are determined by pair-parameter correlation maps¹⁰¹, where the SSE's are computed as a function of two parameters, varied in a certain

range around the minimum, while values of the rest of parameters are kept fixed to their best fit values. The functions are computed for all possible pair combinations of the nine free-fitting parameters of $g_{I-O}(r)$ and $g_{I-H}(r)$, which are N_O , N_H , R_O , R_H , σ_O^2 , σ_H^2 , β_O , β_H and E (see caption of Table 4.1 for the explanation of the symbol). The appendix A presents the contour of SSE at 68.3% ($\pm \sigma$), 95.4% ($\pm 2\sigma$), and 99.73% ($\pm \sigma$) confidence level (σ is standard deviation of an assumed Gaussian distribution of SSE). The projection of the concentric ellipses to the axis determines the boundaries of the parameters.

4.3 Results and discussion

The upper panel of Fig. 4.2 displays the I-O and I-H theoretical EXAFS signal, the lower panel shows the total signal which is the summation of the above theoretical signals. As can be seen, the dominant contribution to the EXAFS signal is the scattering from oxygen. The EXAFS signal associated with hydrogen is non-negligible due to the close distance of hydrogen to the anion. The agreement between the sum of EXAFS signal and the experiment is very good. Optimized structural parameters are reported in Table 4.1. The parameters boundaries are determined for 68.3% confidence level.

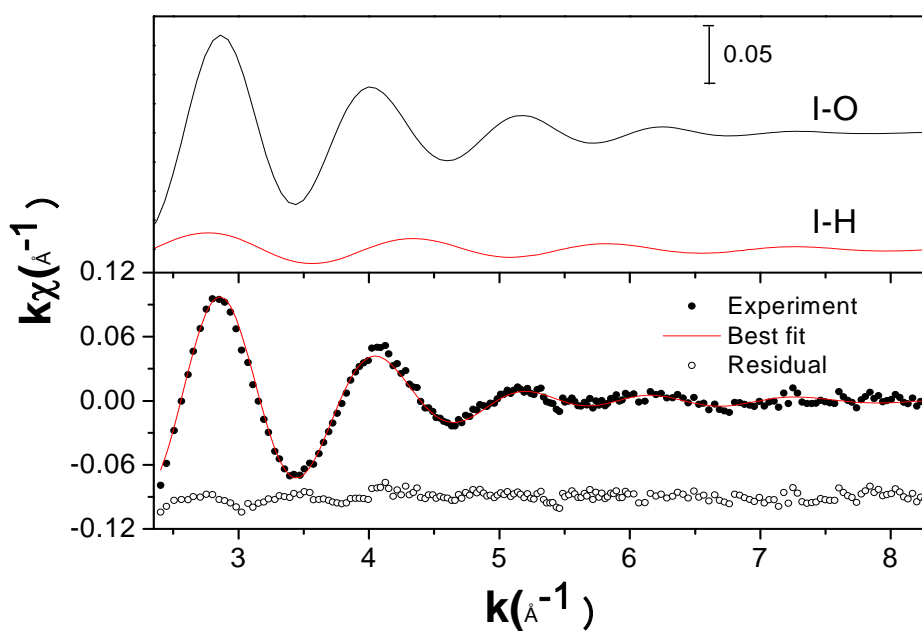


Fig. 4.2: EXAFS spectrum of iodide L3 edge. The upper panel shows EXAFS signal associated with I-O (black) and I-H (red) radial distribution. In the lower panel, total signal and experiment are displayed.

The reconstructed $g(r)$ of I-O and I-H from the best fit parameters are shown in Fig. 4.3 together with $g(r)$ derived from QM/MM simulation. Consistent with the conclusions from the calibration of the simulations (see article below), the reconstructed $g(r)$'s are in good agreement with QM/MM simulation. Interestingly, the coordination number of hydrogen and oxygen are in good agreement with the reported values of 5.1 and 6.6, respectively derived from DFT simulation⁷³. These values are smaller than those yielded by QM/MM simulation, which is 7.9 and 9 for hydrogen and oxygen, respectively. The refined $g(r)$ of I-O shows an opposite asymmetry to that of QM/MM simulation, this discrepancy is believed to originate from high uncertainties of β_X ($X=O,H$), due to the low correlation with other parameters.

Table 4.1. Optimized structural parameters of $g_{I-O}(r)$ and $g_{I-H}(r)$, in comparison with the decomposed QM/MM $g(r)$ for the first shell.

	Best fit values	Lower boundary ^a	Upper boundary ^a	First shell QM/MM $g(r)$
N_O	7.1	5.5	9.2	9.05
N_H	3.6	1.6	6.0	7.93
R_O	3.50	3.46	3.54	3.62
R_H	2.66	2.60	2.76	2.81
σ_O^2	0.03	0.02	0.04	0.063
σ_H^2	0.02	0.009	0.05	0.11
β_O	0.03	0	0.42	0.92
β_H	1.06	0	2 ^b	1.086
E	12.9	11.8	14.2	-

N_X , R_X , σ_X , β_X , E ($X=O$: oxygen, H : hydrogen) are coordination number, averaged distance from the anion, dimensional less skewness and energy shift, respectively.

^a The boundaries are determined at 68.3% of confidence level

^b β_H shows a large uncertainty for 68.3% of confidence level the upper boundary reach the max allowed value, 2. For 95% of confidence, β_H : 0.4 - 1.9

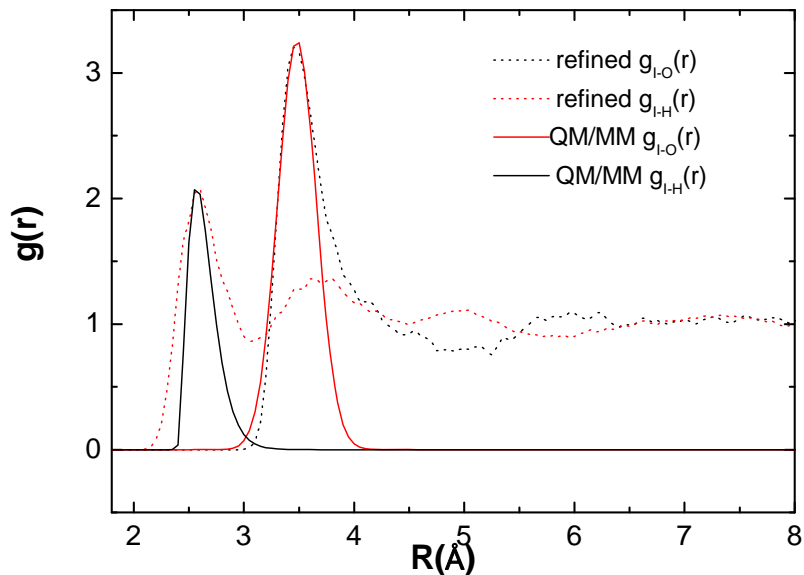


Fig. 4.3: Refined radial distribution function of I-O (solid black) and I-H (solid red), and those derived from QM/MM simulation.

4.4 Conclusions

A detailed study of local structure of iodide in water using peak fitting method is presented for the first time. The resulting structure of iodide first solvation shell is in good agreement with QM/MM simulation. The results show that an accurate structure can be achieved for a disordered system by the simple peak fitting of radial distribution function.

**The solvent shell structure of aqueous iodide:
X-ray absorption spectroscopy and classical, semi-classical and quantum
molecular dynamics**

V. T. Pham¹, I. Tavernelli², C. Milne¹, R. van der Veen¹, P. D'Angelo³, Ch. Bressler¹ and M. Chergui¹

¹ Ecole Polytechnique Fédérale de Lausanne, Laboratoire de spectroscopie ultrarapide, ISIC, FSB, CH-1015 Lausanne, Switzerland

² Ecole Polytechnique Fédérale de Lausanne, Laboratoire de chimie et biochimie computationnelles, ISIC, FSB, CH-1015 Lausanne, Switzerland

³ Dipartimento di Chimica, Università di Roma "La Sapienza", Ple A. Moro 5, 00185 Roma, Italy

The L₃ X-ray absorption spectrum of aqueous iodide is reported, and its EXAFS is compared to theoretical spectra reconstructed from the iodide hydration shell structure obtained from classical, semi-classical (Quantum mechanics Molecular mechanics, QMMM) and full quantum (density functional theory, DFT) molecular-dynamics simulations. In particular, the I-O and I-H radial distribution functions thus derived are used to simulate the EXAFS signal. Since EXAFS is mainly sensitive to short distances around the iodine atom, it is a direct probe of the local solvation structure. The comparison shows that QMMM simulations deliver a satisfactory description of the EXAFS signal, while classical and in particular, DFT-based simulations perform poorly.

I. Introduction:

The properties of solvated ions and the role of the surrounding water molecules are important in a large variety of chemical reactions and biochemical processes.^{1,2} They are also key for transport of ionic solutes in water,³ and ionic hydration dynamics play a central role in several physiological contexts such as ion transport through membranes, where the hydration shell reorganizes in the initial and final stages of the membrane-crossing mechanism.⁴ Despite the importance of this subject, the structure of the solvation shell and its dynamical behaviour are still intensely debated.

Various experimental and theoretical studies have been carried out on halides in water aimed at obtaining a complete description of the solvent shell structure and dynamics. X-ray and neutron diffraction studies yield coordination numbers that are significantly scattered, varying by almost a factor of two for nearly all halides.^{5,6} In the case of iodide, which is the system of interest here, the first peak of the I-O radial distribution function (RDF) was found to be in the range of 3.55–3.76 Å, and the coordination numbers with oxygen atoms varied from 4 to 9. This spread of values underlines the difficulty of defining a solvation shell due to its diffuse character. To determine more precisely the solvent shell structure, hard X-ray absorption spectroscopy on the halides seems more appropriate. Indeed, using X-ray absorption near edge structure (XANES) and extended X-ray absorption fine structure (EXAFS) one probes the local structure around the atom of interest.

Tanida *et al*⁷ recorded L₁- and L₃-edge XANES spectra of aqueous I⁻ and compared them to simulated spectra assuming model geometries of clusters of water molecules around the ion. The spectra were satisfactorily described by taking into account the first hydration shell only. A somewhat similar approach was adopted by Merklings *et al*⁸ for both the XANES and the EXAFS of the bromide ion. They derived optimized geometries of [Br(H₂O)_n]⁻ (1 ≤ n ≤ 8) from quantum chemical calculations, and in order to reproduce the XANES spectra in a satisfactory way, they introduced statistical fluctuations, which in their case were obtained from snapshots of the Monte Carlo (MC) simulations. The latter improvement underlines the complexity of the problem, which is already implicit from the above mentioned spread of coordination numbers and distances. In limiting their analysis to the first shell and to optimized geometries, the simulations of Tanida *et al*⁷ and Merklings *et al*⁸ are not sufficient to capture the dynamics of hydration in a bulk liquid and in particular the exchange with the molecules of the bulk. D'Angelo *et al*⁹ carried out a K-edge EXAFS study of Bromide ions in aqueous solutions. By classical Molecular Dynamics (CMD) simulations, they obtained a Br-O radial distribution function (RdF), which they used with the integral form of the EXAFS

equation to simulate an EXAFS spectrum in very good agreement with the experiment. The integral form of the EXAFS equation¹⁰, rather than the well-known discrete form,¹¹ appears to be ideal for simulating EXAFS signals of disordered systems. While in D'Angelo *et al*'s work the detailed orientation of water molecules around the bromide could not be retrieved because the H atoms were neglected, their approach provided an Oxygen coordination number (6.9) and first shell distance (3.34 Å) within the range of previous (mostly X-ray scattering) studies⁵. The same approach was used by Wallen *et al*¹² who extended the range of temperatures into the supercritical regime of water.

Recently, the valence level electronic structure of water and of aqueous solutions of halide salts was studied by Winter *et al* using photoelectron spectroscopy.¹³ They found no effect of perturbation by the halide salts on the binding energies of water, suggesting that perturbation by the salt ions is minimal. A different conclusion was reached by Cappa *et al*¹⁴ who carried out an Oxygen K-edge absorption study of aqueous sodium halide solutions, finding that the electronic structure of adjacent molecules is significantly perturbed by the ions. This manifests itself by the appearance of an intensity increase of the pre-edge and main-edge absorptions. These results were interpreted by Density functional theory (DFT) molecular dynamics (MD) of clusters of water around the ion, as arising from a strong direct perturbation of the unoccupied molecular orbitals of water by the anions, which does not require significant distortion of the hydrogen bond network beyond the first solvation shell.

From the above, it appears that the interpretation of experimental data, be it structural or electronic, heavily relies on computational simulations.^{2,5,8,9,14,15} In the case of iodide, various force-field-based computational MC or MD studies have been reported.^{3,16-18} Structural data obtained from these simulations include an I–O RdF first peak in the range of 3.55–3.78 Å within the experimentally determined range of values⁵, and an I–H first peak in the range of 2.55–2.93 Å. The first and second RdF peaks show incomplete separation, suggesting a diffuse solvation shell. The calculated coordination number varied from 7.3 to 9.7 (again in the range of experimentally determined values⁵) for oxygen and 6 to 6.6 for hydrogen atoms. The dynamical behaviour of the solvation shell is reflected by the residence time of water molecules in the first shell that ranges from 7.7 to 13.8 ps, depending on parameters of the force field. Recently, Heuft and Meijer¹⁹ reported on a DFT-based Car-Parinello MD simulation of a box of 64 water molecules and one I[−] atom. They found a rather unstructured solvation shell, explained by the fact that the Iodide-water hydrogen bonding is weaker than the water-water hydrogen bond. They also concluded that iodide had no effect on the dipole moment of the surrounding water molecules, which would agree with the valence band

photoemission results of Winter *et al.*²⁰ In addition, the water molecules were found to bind to the ion for relatively short times of the order of 8-10 ps. Finally, their RdF's looked quite different to those derived by classical or semi-classical methods.^{3,18} Very recently, Wick and Xantheas²¹ carried out MD simulations with polarisable potentials of the aqueous solvation structure of Chloride and Iodide in the bulk and at interfaces, identifying an anisotropy of the solvation shell. A number of classical^{17,22} and quantum simulation²³ studies had already pointed out to the solvation shell anisotropy around halides, even in the presence of nonpolarizable anions.²⁴

It appears that most quantum simulations have been carried out on cluster models of water molecules around the halide,^{8,14,19} and that in general, few simulations (classical, semi-classical or quantum) have been checked against experimental observables. The approach by Filippini, D'Angelo and co-workers^{9,10} based on the integral form of the EXAFS equation seems a simple and rather straightforward way of bench marking the computational simulations against experimental data. It would identify which of the classical, semi-classical or quantum simulations give the best radial distribution function, and in particular the first shell distance. As already mentioned, D'Angelo *et al.*⁹ showed that the CMD give a good description of the EXAFS spectra. However, given the extensive use of DFT methods for the description of water structure and dynamics,^{8,14,19,25} it is important to establish to what extent these quantum methods could provide a more realistic description of the shell structure around halides, compared to other methods. Here, we perform classical, semi-classical (Quantum mechanical molecular mechanics, QMMM) and Density Functional Theory (DFT) based MD simulations of aqueous solutions of iodide, which we use to simulate the EXAFS spectrum at the L_3 edge.

The present work stems from our interest in the study of electronic solvation dynamics, which represents the reorganisation of the solvent shell upon an electronic structure change of the solute. Given its importance in chemistry and biology, it represents one of the most studied processes in chemical physics, mainly using molecular dyes as solutes.²⁶ We previously proposed²⁷ an alternative approach based on atomic ions as solutes, whose electronic structure is modified by a short laser pulse that abstracts the electron, while probing is done by X-ray Absorption Spectroscopy using picosecond x-ray pulses from a synchrotron storage ring. We recently demonstrated the feasibility of such experiments by recording the transient XAS spectrum of an aqueous iodide solution at the $L_{1,3}$ edges of iodine, 50 ps after laser excitation.^{28,29} Clear signatures of both electronic (resulting from the electron abstraction) and solvent shell structure changes could be read off the spectra. However a

quantitative analysis of the solvent shell reorganization relies on a clear description of the solvation shell structure around Γ^- prior to laser excitation, which is the object of this contribution.

II. Experimental Methods:

A 500 mM iodide aqueous solution was prepared by dissolving sodium iodide 99.9% purity in distilled water. The sample is circulated in a free flowing liquid jet of 200 μm thickness. X-ray absorption spectra at the iodine L_3 edge recorded in transmission mode at the micro-XAS beamline of the Swiss Light Source (Villigen, Switzerland), using the third harmonic of the undulator. An Si(111) double crystal monochromator was used, giving an energy resolution of 0.8 eV in the measured energy range. Two ionization chambers filled with He at 1 bar were utilized to measure the incoming and the transmitted beam intensity through the sample. The synchrotron was operated at 350 mA. The incident fluxes at the sample position are typically 5.5×10^{11} ph/s at the L_3 -edge.

III. Computational methods:

Classical MD

All classical MD simulations used for the equilibration of the QM and QM/MM setups were performed in the isothermal-isobaric ensemble (NPT) using the AMBER 7 package with the parm99 force-field. The system is made of one Γ^- ion solvated in 1192 TIP3P water molecules in a cubic box of $(33.6 \text{ \AA})^3$, using periodic boundary conditions. The system was equilibrated for 10 ns with a time-step of 1 fs and was maintained at 300 K and 1 atm by a thermo- and barostats of the Berendsen type. Electrostatic interactions were treated using the particle mesh Ewald scheme. The last 5 ns of the MD run was used to compute the structural properties of iodide solvation shells at a classical level.

Full-DFT setup and first principle MD simulations

In the full-DFT setup, aqueous iodide was modelled using a periodically replicated cubic simulation supercell of side 18.15 \AA , containing one iodide ion and 183 water molecules. The cell size and the number of water molecules were determined by imposing that the iodine-water system yields a total pressure equal to a sample of liquid water at room temperature and standard pressure (1 atm). To this end, a classical MD trajectory of 10 ns at 300 K and 1 atm was computed to set up the initial configuration for the DFT-based MD simulations.

The system composed of a solvated iodide ion and the water molecules was treated within periodic boundary conditions and the Kohn-Sham orbitals were expanded in plane-waves at the Γ point of the Brillouin zone up to a kinetic energy cutoff of 100 Ry.

All DFT calculations were performed using Troullier-Martins-type pseudopotentials for the core electrons. Integration of the nonlocal parts of the pseudopotential was performed using the Kleinman-Bylander scheme. The exchange and correlation potential was described at the BLYP level of theory. A short preparation run of ~ 2 ps was performed starting from the classically equilibrated geometry. This was followed by a production run of 5.5 ps that was used to sample the trajectory for the analysis of the iodide solvation geometries.

All DFT based MD simulations were performed using the Born-Oppenheimer scheme with a time step of 15 au. During the preparation run which follows the classical equilibration, the temperature was controlled through a Nosé-Hoover thermostat. The production runs were performed in the microcanonical ensemble at constant energy using the software package CPMD.³⁰

QM/MM setup and QM/MM MD simulations

The QM/MM setup consists of a single iodide ion described at a DFT level of theory solvated in a classical bath of 1192 TIP3P water molecules in a box of $(33.6 \text{ \AA})^3$. The force field parameters used for the water molecules are those employed in the classical MD simulations. The quantum part of the system was confined in a cubic box with 12 \AA edge, but classical water molecules could enter the QM box. The inherent periodicity in the plane-wave calculations was circumvented solving the Poisson equation for non-periodic boundary conditions, while periodic boundary conditions were retained for the classical solvent box. All other simulation conditions for the QM part (the I^- ion) and MD parameters were kept identical to the ones used in the full-DFT MD simulations. The steric interaction between the QM and the MM part were modelled by a Lennard-Jones potential as described by the parm99 force field, while the electrostatic interactions with the neighbouring MM atoms were described by a fully Hamiltonian hierarchical coupling scheme³¹ as implemented in the CPMD code.

The simulation protocol follows closely the one used for the full-DFT MD calculations. The only difference lies in the quality of the sampling (trajectory length) since the QM/MM approach is computationally less demanding and allows therefore longer simulation times. The QM/MM radial distribution functions were computed from a single trajectory of 15 ps.

IV. Simulation of EXAFS spectra:

For the hydration shell of halogen anions, particularly those with large radii, due to the large structural disordered the main contribution to the EXAFS signal is associated with the single scattering events that reflect a two-body interaction. Rather than using the usual discrete form of the EXAFS equation,¹¹ the signal is modeled as a function of the radial distribution function $g(r)$ as¹⁰:

$$\chi(k) = \int_0^{\infty} 4\pi\rho_O r^2 g_{I-O}(r) A_O(k, r) \sin(2kr + \phi_O(k, r)) dr + \int_0^{\infty} 4\pi\rho_H r^2 g_{I-H}(r) A_H(k, r) \sin(2kr + \phi_H(k, r)) dr \quad (1)$$

where $A(k, r)$ and $\Phi(k, r)$ are the amplitude and phase functions. Conversely, an average hydration shell structure, described by radial pair distribution function, can be extracted from the analysis of the EXAFS signal using Eq. 1. Theoretical EXAFS signal at the iodine L_3 edge associated with the oxygen and hydrogen atoms of the first shell water molecules, are calculated from Eq. 1 using the GNXAS program.^{10,32} The phase shifts $\Phi(k, r)$ are calculated from a snapshot of atomic coordination given by the MD simulations. A Hedin-Lundqvist (HL) plasmon-pole was used for the phase shift calculation with muffin-tin radii for iodide, oxygen and hydrogen of 2.28, 0.9, and 0.21 Å, respectively. Inelastic losses of photoelectron are accounted for by complex potentials where the imaginary part includes core-hole width of 3.08 eV for the $2p_{3/2}$ hole.³³ The $\chi(k)$ signal is mainly sensitive to a limited distance from the absorber due to the finite photoelectron mean-free path, this effect together with the spectral damping due to monochromator resolution are included in the scattering amplitude $A(k, r)$. Reduction amplitude S_0^2 , accounting for a uniform reduction of the signal associated with many-body effects, is set to 1. The total $\chi(k)$ contribution which is the sum of the two-body signals from oxygen and hydrogen atoms were shifted in energy space to fit the experiment. The agreement between the theory and the experiment is then evaluated by sum of squared error (SSE) value expressed in Eq. 3.

$$SSE = \sum_{i=1}^N (\chi_i^{\text{exp}} - \chi_i^{\text{theo}})^2 \quad (3)$$

where χ_i^{exp} and χ_i^{theo} are experimental and theoretical EXAFS signal for each data point i .

V. Results and discussion:

Figure 1 shows the L_3 -edge XAS spectrum of aqueous Iodide at room temperature. Figure 2 shows the I-O and I-H $g(r)$'s from the classical, the QMMM and the DFT MD simulations. These $g(r)$'s are in agreement with those of the literature both for the classical^{3,18,21} and for the DFT simulations¹⁹. The DFT $g(r)$'s point to a smaller density of water molecules in the first shell than the classical or QMMM simulations. Finally, the classical and DFT simulations point to a more pronounced shell structure, at least up to the first two shells. The dotted trace in Figure 3 is the L_3 -edge EXAFS spectrum extracted from the raw data with Pyspline³⁴, a program for EXAFS data reduction. The background was modelled by three segmented cubic functions.

In Figure 3 we compare the experimental and theoretical $\chi(k)$ spectra, calculated from Eq. 1 using the $g(r)$'s of Figure 2. The structural parameters derived from the classical, QMMM and DFT simulations have been kept fixed in the EXAFS analysis. In this way the first hydration shell structure obtained from the simulations can be directly compared with experimental data and the validity of the theoretical framework used in the simulations can be assessed. The upper panels of Figure 3 show the separate I-H and I-O first shell contributions as derived from their respective $g(r)$'s (Figure 2). The sum of these two contributions (total) is overlaid onto the EXAFS experimental signal, and the resulting residuals are also shown.

It is clear that the classical and QMMM-based $g(r)$'s deliver a better agreement with the experimental data than the DFT simulations. The classical MD is also quite satisfactory but shows deviations in the high k region, whereas the QMMM-based $g(r)$'s provide a better fit. Thus we can conclude that the QMMM simulation provides a more accurate description of the solvent shell structure.

If we consider the good description of the EXAFS signal obtained from the present semi-classical simulations and the pure classical simulations of D'Angelo *et al* on aqueous Br^- ⁹, it appears that the main reason for the poorer agreement with the DFT-based simulations lies in the quality of the water-water intermolecular interactions and the fact that these are comparable or stronger than the solute-water interaction. Indeed for solutes with an ordered solvent shell, such as aqueous Co^{2+} which forms a $\text{Co}(\text{H}_2\text{O})_6$ complex, DFT-MD did generate a structure that satisfactorily reproduces the EXAFS spectrum.³⁵ Previous studies have shown that the outcome of DFT-based MD simulations of liquid water is very sensitive to the particular choice of the functional³⁶ and basis set³⁷. Water computed at DFT level within the generalized gradient approximation (GGA) for the exchange-correlation functional is generally over structured and diffuses one order of magnitude more slowly than experimentally determined. Hybrid functionals improve the predictions slightly,³⁸ and the

reason for such discrepancies was the subject of a recent theoretical study³⁹. It is generally believed that the structure of liquid water stems from the competition between H-bond and van der Waals (vdW) interactions.⁴⁰ Even though DFT-GGA has been successful in describing a wide variety of strongly interacting systems, it has not found equal success in describing weak interactions.

Of special importance here is the determination of anisotropy of the solvation shell. In ref. ²¹, using classical molecular dynamics simulations with polarisable potentials the authors identified an anisotropy in the radial-angular distribution function (RADF) of water around iodide. They used the same definition of the distance as in the radial distribution function, but defined the angle between the anion-hydrogen vector and the induced dipole vector of the anion. The solvation shell was clearly anisotropic with a very low probability of finding anions near the region in which the induced dipoles are pointing away, and with a high probability of finding hydrogen atoms on the other side. Given the weakness of the anion induced dipole, one may ask if this anisotropy is real. Therefore, in order to address this point, here we adopt a different approach. Instead of using the direction of the dipole on the ion, we take as reference the direction between the iodide and the closest H atom (that may change from one frame to the other, but not so frequently) and for all anion-hydrogen vectors in the sample we compute the corresponding angles α_i formed with the reference axis, and the their length, r_i . The index i runs over all H-atoms and a value of $\alpha=0$ defines the direction towards the closest H-atom. The result is shown in Figure 4, where we plot the RADF sampled along our trajectories (which corresponds to the probability of all $\{\alpha_i, r_i\}$ pairs) as a function of $r \cos(\alpha)$ and $r \sin(\alpha)$. For the sake of comparison, we present the result for both the DFT and QMMM MD simulations. Interestingly, we find a rather structured distribution of water H-atoms in the first solvation shell of I⁻. Along the abscissae at a distance of about 2.5 Å ($\alpha=0$) is the distribution of the closest H-atom, which has a standard deviation of about 0.3 Å in both full DFT and QMMM simulations. In the same direction, at small angular deviations from the reference axis, the distributions of the second and third closest H-atoms are also well resolved. Overall, the agreement between the two simulation set-ups is good, even though a slightly more structured RADF is observed in the full DFT calculation in agreement with what was observed for the radial distribution functions.

In conclusion, we have performed classical, semi-classical (QMMM) and full quantum (DFT) molecular dynamics simulations of iodide in water, which we have calibrated against experimental EXAFS spectra at the L₃-edge. It appears that for aqueous halides QMMM and

classical simulations deliver a better description of the solvation shell. In particular, QMMM offers the potential of a more precise description of the quantum part due to the solute-solvent interaction, while allowing simulations over several picoseconds. We discussed the origin of the discrepancies of DFT-MD, but we stress that they are peculiar to the case of weak solute-solvent interactions, leading to disordered solvent shells. We also confirm that the solvation shell around iodide is anisotropic, a feature that is of importance when discussing the solvent shell rearrangements upon light excitation of the system.²⁸

Acknowledgments: we thank the Swiss NSF for support via contracts 200021-107956, 200021-105239/1 and 200020-116533 and the Sekretariat für Bildung und Forschung via contract COST D 35 060016. We also thank the Pleiades Cluster for High Performance Computing (HPC) resource.

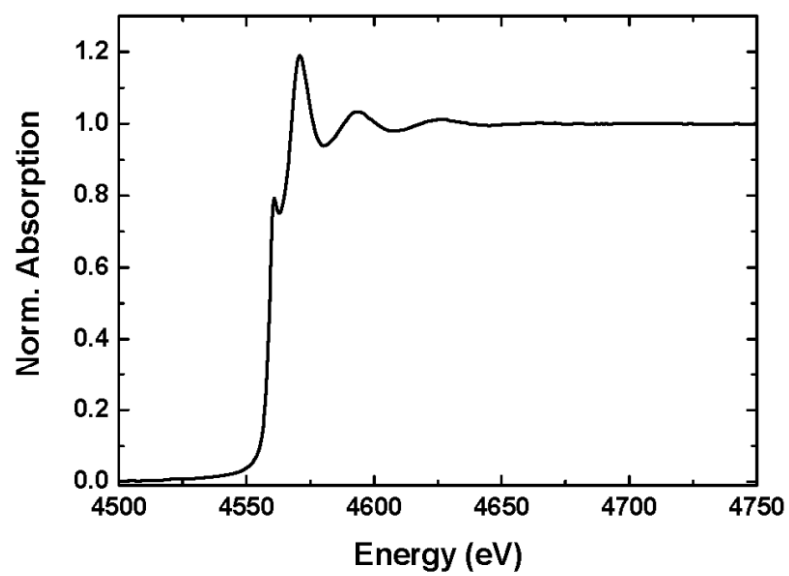


Figure 1. Aqueous iodide L₃-edge absorption spectrum.

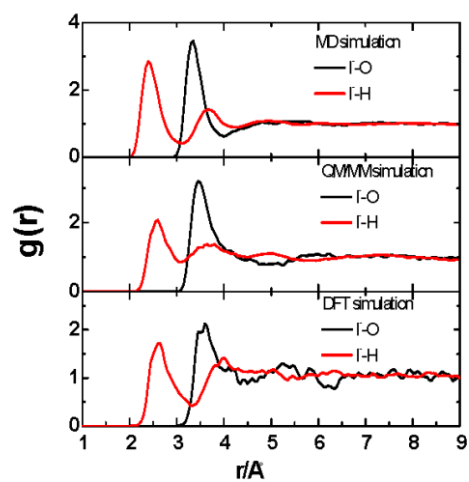


Figure 2. Radial distribution function around iodide of the oxygen (black) and hydrogen (red) atoms of waters to iodide from classical MD, QM/MM and DFT simulations.

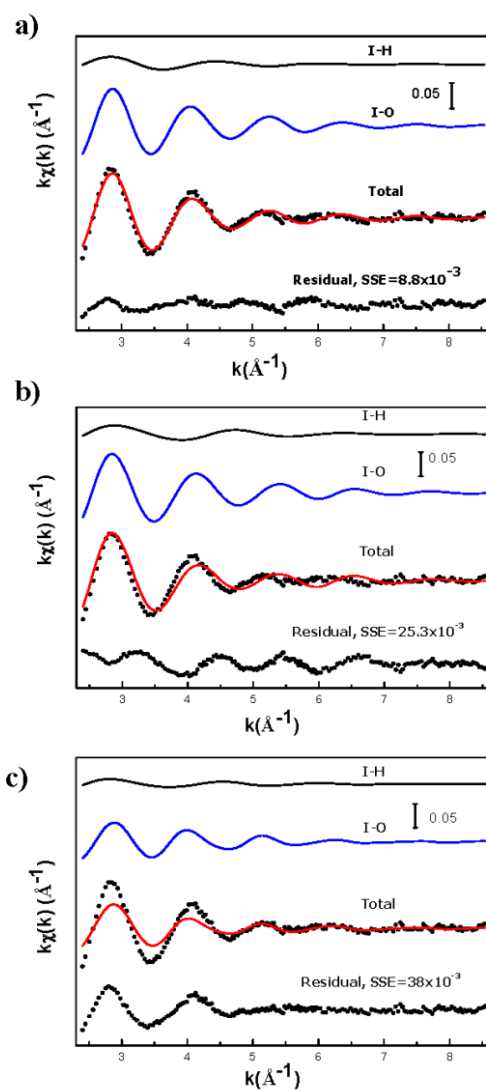


Figure 3. Theoretical EXAFS calculations from the simulated QM/MM (a), CMD (b) and DFT (c) structures. The black and blue curves are EXAFS signal associated with I-H and I-O scattering, respectively. The red curves are total EXAFS signals. The upper dotted black curves are the experiment, the lower ones are residual between the theory and the experiment. The quality of the calculations (SSE) is given in the graphs.

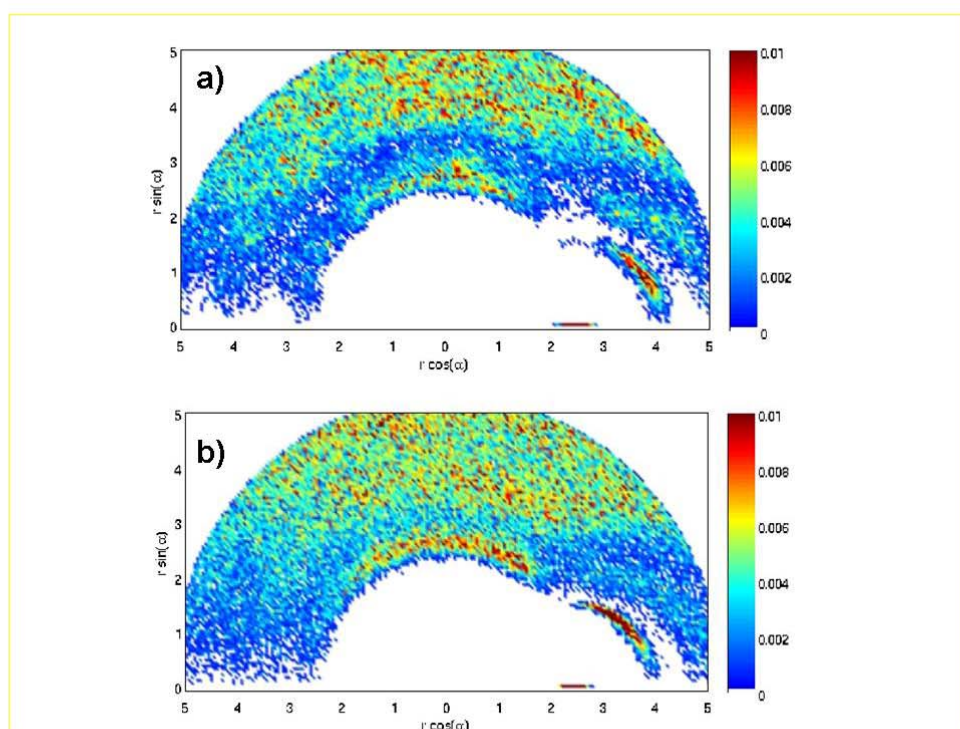


Figure 4. Radial-angular distribution function (RADF) of iodide anions with the water hydrogen atoms obtained from the DFT (a) and the QMMM (b) simulations. The reference is the direction between the iodide and the closest H atom (that may change from one frame to the other, but not so frequently). We define the angle α between this reference axis and the anion-hydrogen vector (a value of $\alpha=0$ defines the direction towards the closest H-atom).

References:

- 1 K. Ando and J. T. Hynes, *Journal of Physical Chemistry B* **101** (49), 10464 (1997).
- 2 D. Laage and J. T. Hynes, *Proceedings of the National Academy of Sciences of the United States of America* **104** (27), 11167 (2007).
- 3 S. Koneshan, J. C. Rasaiah, R. M. Lynden-Bell, and S. H. Lee, *Journal of Physical Chemistry B* **102** (21), 4193 (1998).
- 4 E. Gouaux and R. MacKinnon, *Science* **310** (5753), 1461 (2005).
- 5 H. Ohtaki and T. Radnai, *Chemical Reviews* **93** (3), 1157 (1993).
- 6 R. M. Lawrence and R. F. Kruh, *Journal of Chemical Physics* **47** (11), 4758 (1967); A. K. Soper, *Journal of Physics-Condensed Matter* **9** (13), 2717 (1997).
- 7 H. Tanida, K. Kato, and I. Watanabe, *Bulletin of the Chemical Society of Japan* **76** (9), 1735 (2003).
- 8 P. J. Merklung, R. Ayala, J. M. Martinez, R. R. Pappalardo, and E. S. Marcos, *Journal of Chemical Physics* **119** (13), 6647 (2003).
- 9 P. Dangelo, A. Dinola, A. Filipponi, N. V. Pavel, and D. Roccatano, *Journal of Chemical Physics* **100** (2), 985 (1994).
- 10 A. Filipponi, *Journal of Physics-Condensed Matter* **6** (41), 8415 (1994).
- 11 J. J. Rehr and R. C. Albers, *Reviews of Modern Physics* **72** (3), 621 (2000).
- 12 S. L. Wallen, B. J. Palmer, D. M. Pfund, J. L. Fulton, M. Newville, Y. J. Ma, and E. A. Stern, *Journal of Physical Chemistry A* **101** (50), 9632 (1997).
- 13 R. Weber, B. Winter, P. M. Schmidt, W. Widdra, I. V. Hertel, M. Dittmar, and M. Faubel, *Journal of Physical Chemistry B* **108** (15), 4729 (2004).
- 14 C. D. Cappa, J. D. Smith, K. R. Wilson, B. M. Messer, M. K. Gilles, R. C. Cohen, and R. J. Saykally, *Journal of Physical Chemistry B* **109** (15), 7046 (2005).
- 15 B. Winter and M. Faubel, *Chemical Reviews* **106** (4), 1176 (2006).
- 16 E. Brodskaya, A. P. Lyubartsev, and A. Laaksonen, *Journal of Chemical Physics* **116** (18), 7879 (2002); A. Ignaczak, J. A. N. F. Gomes, and M. N. D. S. Cordeiro, *Electrochimica Acta* **45** (4-5), 659 (1999); P. Jungwirth and D. J. Tobias, *Chemical Reviews* **106** (4), 1259 (2006).
- 17 L. X. Dang and B. C. Garrett, *Journal of Chemical Physics* **99** (4), 2972 (1993).
- 18 B. Hribar, N. T. Southall, V. Vlachy, and K. A. Dill, *Journal of the American Chemical Society* **124** (41), 12302 (2002).
- 19 J. M. Heuft and E. J. Meijer, *Journal of Chemical Physics* **123** (9) (2005).
- 20 B. Winter, R. Weber, W. Widdra, M. Dittmar, M. Faubel, and I. V. Hertel, *Journal of Physical Chemistry A* **108** (14), 2625 (2004).
- 21 C. A. Wick and S. S. Xantheas, *Journal of Physical Chemistry B* **113** (13), 4141 (2009).
- 22 M. A. Carignano, G. Karlstrom, and P. Linse, *Journal of Physical Chemistry B* **101** (7), 1142 (1997).
- 23 H. A. Stern, G. A. Kaminski, J. L. Banks, R. H. Zhou, B. J. Berne, and R. A. Friesner, *Journal of Physical Chemistry B* **103** (22), 4730 (1999); S. Raugei and M. L. Klein, *Journal of Chemical Physics* **116** (1), 196 (2002).
- 24 S. Rajamani, T. Ghosh, and S. Garde, *Journal of Chemical Physics* **120** (9), 4457 (2004).
- 25 B. Winter, E. F. Aziz, U. Hergenbahn, M. Faubel, and I. V. Hertel, *Journal of Chemical Physics* **126** (12) (2007); B. Winter, E. F. Aziz, N. Ottosson, M. Faubel, N. Kosugi, and I. V. Hertel, *Journal of the American Chemical Society* **130** (22), 7130 (2008).

- 26 O. Kühn and L. Wöste, *Analysis and control of ultrafast photoinduced reactions*.
(Springer, Berlin ; New York, 2007).
- 27 C. Bressler, M. Saes, M. Chergui, D. Grolimund, R. Abela, and P. Pattison, *Journal of*
Chemical Physics **116** (7), 2955 (2002).
- 28 V. T. Pham, W. Gawelda, Y. Zaushitsyn, M. Kaiser, D. Grolimund, S. L. Johnson, R.
Abela, C. Bressler, and M. Chergui, *Journal of the American Chemical Society* **129**
(6), 1530 (2007).
- 29 C. Bressler, R. Abela, and M. Chergui, *Zeitschrift Fur Kristallographie* **223** (4-5), 307
(2008).
- 30 C. I. Corp, (1990-2004).
- 31 A. Laio, J. VandeVondele, and U. Rothlisberger, *Journal of Chemical Physics* **116**
(16), 6941 (2002).
- 32 http://gnxas.unicam.it/XASLABwww/pag_gnxas.html.
- 33 M. O. Krause, *Journal of Physical and Chemical Reference Data* **8** (2), 307 (1979).
- 34 A. Tenderholt, B. Hedman, and K. O. Hodgson, presented at the 13th International
Conference On X-Ray Absorption Fine Structure (XAFS13), Stanford, California,
2006 (unpublished).
- 35 R. Spezia, M. Duvail, P. Vitorge, T. Cartailier, J. Tortajada, G. Chillemi, P. D'Angelo,
and M. P. Gaigeot, *Journal of Physical Chemistry A* **110** (48), 13081 (2006).
- 36 J. VandeVondele, F. Mohamed, M. Krack, J. Hutter, M. Sprik, and M. Parrinello,
Journal of Chemical Physics **122** (1), 014515 (2005).
- 37 H. S. Lee and M. E. Tuckerman, *Journal of Chemical Physics* **125** (15), 154507
(2006).
- 38 T. Todorova, A. P. Seitsonen, J. Hutter, I. F. W. Kuo, and C. J. Mundy, *Journal of*
Physical Chemistry B **110** (8), 3685 (2006).
- 39 I. C. Lin, A. P. Seitsonen, M. D. Coutinho-Neto, I. Tavernelli, and U. Rothlisberger,
Journal of Physical Chemistry B **113** (4), 1127 (2009).
- 40 C. H. Cho, S. Singh, and G. W. Robinson, *Journal of Chemical Physics* **107** (19), 7979
(1997).

Chapter 5 Femtosecond Optical Transient Absorption of aqueous iodide

5.1 Introduction

In recent years, there have been intense studies of solvation dynamics of iodide in water using femtosecond laser absorption spectroscopy. Dynamics of the solvated electron upon one- and multiphoton excitation has been investigated by several groups^{13,14,19}. The mechanism of one-photon detachment is mainly based on two models. The first model involves the creation of contact pair via CTTS excitation. Upon one photon excitation of iodide, the valence electron is promoted to the lowest excited state s-like orbital of the CTTS. The electron creates with an iodine radical a so called contact-pair at a rate of k_p , where the electron either non-adiabatically recombines with the parent atom (geminate recombination) at a rate constant k_r or escapes the solvent cage at a rate constant k_d to become a hydrated electron. This model was proposed by Staib and Borgis for aqueous Cl^- ¹⁷ and was implemented on I^- by Bradforth's group¹⁵. The second model is based on the diffusion-limited recombination where the reverse electron transfer reaction is immediate once the geminate partners reach a certain separation (reaction radius). The kinetics of solvated electron is fitted using this model to get a reaction radius and parameters for the potential well created by iodine and electron²². This model shows a better fit to the data than the Staib-Borgis model since the recombination of electron with partners are determined by the distance to the iodine radical, meaning that the escaped electron in the Staib-Borgis model can still be non-geminately recombined if it is within the reaction radius of iodine, which is closer to the truth.

The photophysics of iodide under multi-photon excitation is very different from the one-photon case²². Pioneer experimentalists in this subject are Eisenthal and co-workers¹³ who monitored the kinetics of electron generated by two and three photons of 312.5 nm from the I^- . They found that the multiphoton absorption of aqueous iodide promotes the electron from the ground state to higher lying states of the CTTS band, p-like state, where it non-adiabatically relaxes to lowest states of CTTS band, s-like state in 50 fs. The electron in the lowest CTTS state then relaxes in 80 fs to the ground state of the I^- . The solvation process of I^- can be totally different if I^- is excited to different upper states of the CTTS band, for which no other works have been reported.

In this work we apply both kinetics and diffusion-limited models to study the kinetics of electron upon one-photon excitation. The results are then compared with the literature. Though our main concern in multiphoton excitation is to find the production yield of iodine atoms at the same pump wavelength and fluence as in the x-ray experiments, the analysis reveals new insights in solvation dynamics of iodide upon multiphoton excitation. The kinetics of electron and iodide bleach under multiphoton excitation mechanism are reported for the first time and discussed.

5.2 Single photon excitation

In the following section, we present all-optical pump-probe studies on aqueous iodide using one-photon detachment. The sample is excited at 240 nm and the solvated electron is probed at 800 nm. At this probing wavelength the signal is dominated by the solvated electron with its molar absorption $\epsilon_e = 17600 \text{ M}^{-1}\text{cm}^{-1}$, while the absorption of diiodide I_2 is negligible in comparison with that of solvated electron (Fig. 5.1). The kinetics of the electron signal are studied under a excitation range of 13-75 mJ/cm^2 and the sample concentration was varied within 50-1000 mM. Details of the experiments are described in chapter 3.

Fig. 5.2 shows a typical time trace of 240 nm pump-800 nm probe for a 50 mM sample (fluence 35 mJ/cm^2). The data is very similar to the kinetics of electron generated by 255 nm pump as reported in ref. ¹⁵. The rise time of ~ 200 fs is obtained after a deconvolution of the rising edge (fitted with a step function) with our cross correlation time of 0.2 ps, which is consistent with the appearance time of solvated electron found by other groups ^{15,19}. The decay is fitted with two exponential decay functions plus an infinite exponential decay yielding a first decay time $\tau_1 = 15.7$ (0.3) ps with a relative amplitude of 57%, $\tau_2 = 103$ (6) ps taking 18% of the maximum, the survival probability remains 25% of the maximum at long delay times. These decay times are relatively longer than those observed in 255 nm pump 800 nm probe ¹⁴.

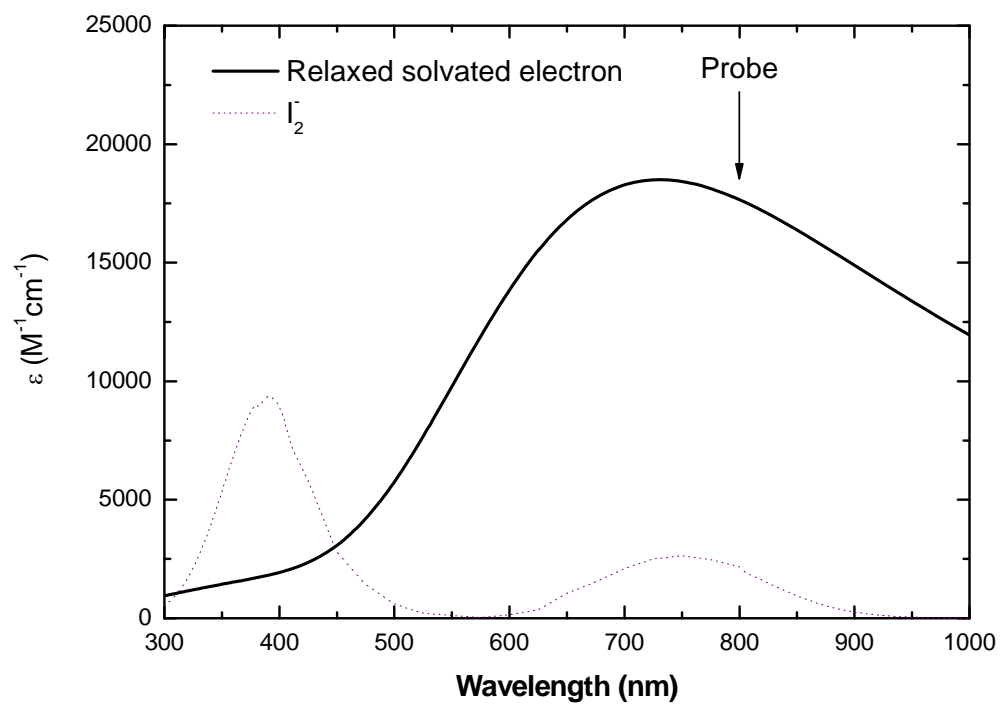


Fig. 5.1: Absorption extinction of fully relaxed solvated electron (solid curve) and diiodide I_2^- (dotted curve). Taken from ref. 130

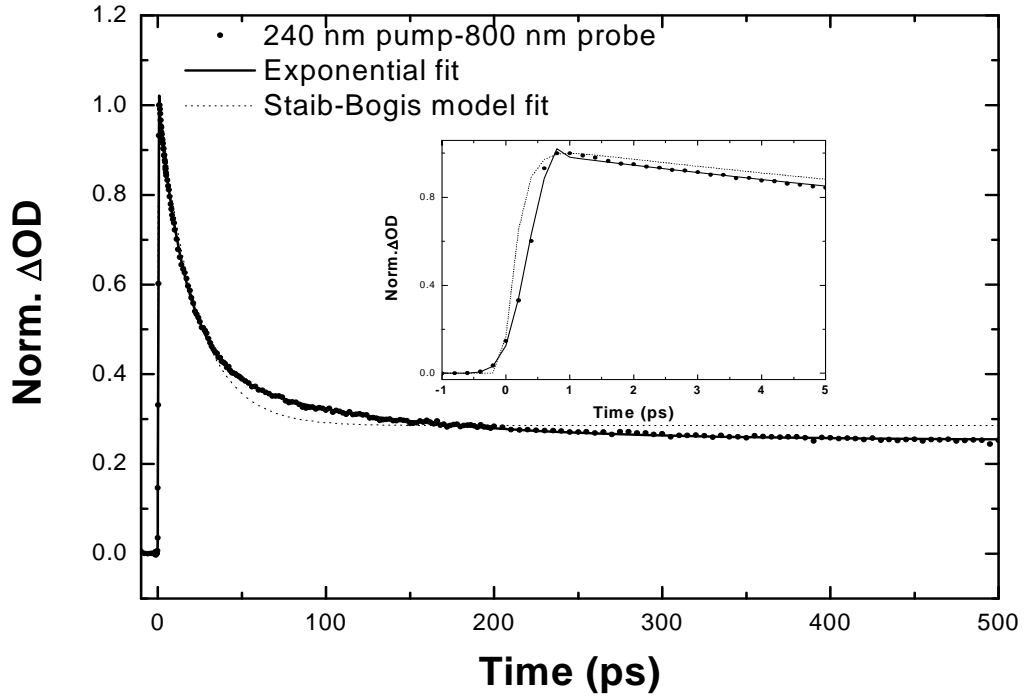
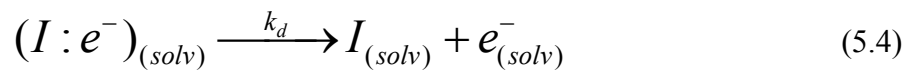
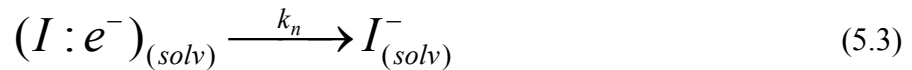
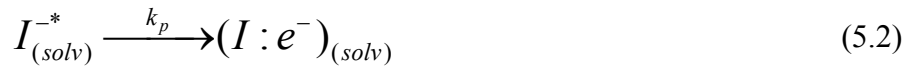
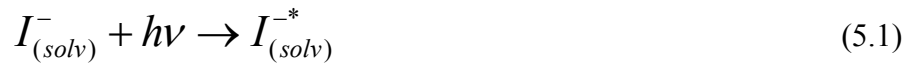


Fig. 5.2: Kinetics of solvated electron probed by 800 nm upon 240 nm one-photon excitation. Solid circle is measured data, solid curve represents 3 components exponential decay fit, dotted curve show the fit using Staib-Borgis model.

The simplest model based on competitive kinetics suggested by Staib and Borgis¹⁷ is employed. The following reactions are accounted for to simulate the kinetics:



where $I_{(solv)}^-$, $I_{(solv)}^{-*}$, $(I:e^-)_{(solv)}$ and $e_{(solv)}^-$ are solvated iodide, excited iodide anion, I:e contact pair and solvated electron, respectively. From this set of equations, one derives a set of rate

equations for the time dependent species populations (annotated by the species symbol inside square bracket)

$$\left\{ \begin{array}{l} \frac{d[I_{(solv)}^-]}{dt} = -P(t) \cdot [I_{(solv)}^-] + k_n \cdot [(I : e^-)_{(solv)}] \\ \frac{d[I_{(solv)}^{-*}]}{dt} = P(t) \cdot [I_{(solv)}^-] - k_p \cdot [I_{(solv)}^{-*}] \\ \frac{d[(I : e^-)_{(solv)}]}{dt} = k_p \cdot [I_{(solv)}^{-*}] - k_n \cdot [(I : e^-)_{(solv)}] - k_d \cdot [(I : e^-)_{(solv)}] \\ \frac{d[I_{(solv)}]}{dt} = k_d \cdot [(I : e^-)_{(solv)}] \\ \frac{d[e^-]}{dt} = k_d \cdot [(I : e^-)_{(solv)}] \end{array} \right. \quad (5.5)$$

where $P(t)$ is initial excited population of iodide created by the pump pulse. We assume that the pump pulse has a Gaussian profile, thus the initial population of photoproducts has the same shape, with a pulse duration given by the cross correlation

$$P(t) = f \cdot \exp\left(\frac{-t^2}{t_c^2}\right) \quad (5.6)$$

where f and t_c are fractional excitation and cross correlation time, respectively. The analytical solution for Eq. 5.5 after the pump was achieved assuming that the cross section for the $(I : e^-)_{(solv)}$ pair is the same as for the solvated electron $e_{(solv)}^-$:

$$\Omega_{SB}(t) = \frac{k_d}{k_d + k_n} + \frac{k_p}{k_d + k_n - k_p} \cdot \left[\frac{k_p - k_d}{k_p} e^{-k_p t} - \frac{k_n}{k_n + k_d} e^{-(k_d + k_n)t} \right] \quad (5.7)$$

The dotted curve of Fig. 5.2 displays the fit of the numerical solution of Eq. 5.5 with the experiment, yielding best fit parameters $1/k_p = 0.19 \pm 0.04$ ps, $1/k_n = 29.3 \pm 1.1$ ps, $1/k_d = 76.9 \pm 3.7$ ps. These values agree with those of Kloepper *et al.* who fitted the kinetics of the solvated

electron using the above analytical solution. As can be seen from the figure, the fit shows a bad agreement with the data from 100 ps onwards. The deviation of the model with experiment stems from the assumption that electrons that initially diffuse away from their geminate partners are no longer available for recombination leading to a leveling-off of the fitted curve¹⁶. The continued decay in the experimental data reflects secondary recombinations.

For a better modelling of the geminate recombination, an interaction potential between geminate partners is required. The approach is based on Shushin's semi-analytical theory¹⁰² for diffusion-controlled reaction in a potential well. In this model, geminate partners interact by means of an attractive mean force potential (MFP), $U(r)$, with Onsager radius a (at which $U(a) \approx -kT$). It can be shown that the recombination and escape from the potential well are pseudo first-order reaction. The survival probability is given by²²

$$\Omega(t) \approx 1 - (1 - p_d) \left[1 + \frac{\text{Im } \lambda^{-1} \exp(\lambda^2 W t) \text{erfc}(\lambda \sqrt{W t})}{\text{Im } \lambda} \right] \quad (5.8)$$

where $W = W_r + W_d$ is the total decay rate (W_r , W_d being decay rate of recombination and dissociation), $p_d = W_d / W$ is the escape probability of a geminate pair generated in the potential well ($r_i < a$), $\lambda = \alpha / 2 + i(1 - \alpha^2 / 4)^{1/2}$, where $\alpha = p_d \sqrt{a^2 W / D}$ with D being the diffusion constant. In the derivation of Eq. 5.8, it was assumed that all the geminate pairs were generated inside the potential well ($r_i < a$). In more general case, Shushin's equations must be averaged over the initial electron distribution $P(r_i)$; a compact analytical expression similar to Eq. 5.8 cannot be obtained in such a case but a numerical solution can be computed from the Laplace transform of $\Omega(t)$ using Eq. B11 and B24 given in Appendix B of ref.²². In Shushin's theory all geminate pairs for which $r_i < a$ have the same recombination dynamics, so that the overall kinetics are not sensitive to the exact profile of $P(r_i)$ at these short distances.

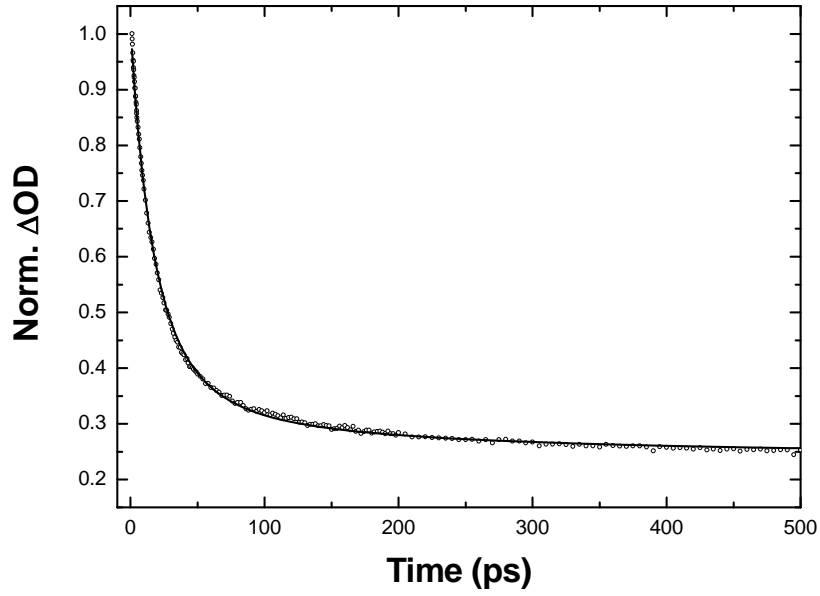


Fig. 5.3: Open circle curve represents the same data as Fig. 5.2, solid curve shows the fit using MFP model.

This model is implemented for the 240 nm pump-800 nm probe time trace. The best fit parameters are shown in Table 5.1 together with reported values for comparison:

Table 5.1:

	$\lambda_{\text{pump}}(\text{nm})$	p_d	α	$W^{-1}(\text{ps})$
This work	240	0.221 ± 0.003	0.41 ± 0.02	17.5 ± 0.3
Lian <i>et al.</i> 22	225	0.216	0.34	14

In order to estimate the Onsager radius a , we use a diffusion coefficient at room temperature $D=0.56 \text{ \AA}^2/\text{ps}$ from the published values $D_{I^0} = 0.1 \text{ \AA}^2/\text{ps}$ ²⁸ and $D_{e_{aq}^-} = 0.46 \text{ \AA}^2/\text{ps}$ ¹⁰³. The resulting Onsager radius estimated for Lian's best fit values is 4.4 \AA versus our value is 5.8 \AA . The mismatch between these two values may come from the excitation energy. In fact, our Onsager radius is within the predicted values of the average center of mass separation between

iodine and electron 5.5-6 Å derived from simulation ¹⁰⁴. From our best fit parameters, we estimated time constants for the recombination and dissociation of the geminate partners (via the relationship between p_d and W_d given above) to be $\tau_r = 22$ ps and $\tau_d = 79$ ps, respectively. These decay rates are in good agreement with k_n and k_d obtained from the kinetics model.

Fig. 5.4a displays the kinetics profile of 240 nm pump-800 nm probe for pump fluences within a range of 13-75 mJ/cm², the sample concentration is 50 mM. All curves have the same kinetics supporting the Shushin's theory which states that all geminate pairs for which $r_i < a$, where $a=5.8$ Å, have the same recombination dynamics. In order to simulate the kinetics of electron beyond 100 ps, where subsequent products of the iodide photodetachment process are formed, we included all known photochemical reactions. The reactions are based on the photodetachment studies of Br⁻ ¹⁰⁵. Eq. 5.9-5.17 are subsequent reactions to the set of Eq. 5.1-5.4. For early reactions in Eq. 5.1-5.4, the rate constants k_p , k_n and k_d obtained from the fit are utilized, the rate constants for subsequent reactions, k_5 - k_{13} are taken from published values. Table 5.2 shows the rate constants and its reference. These completed set of reactions are later used to calculate the population of iodine radical needed for analyzing the x-ray data, as presented in chapter 6. Fig. 5.4b shows the normalized solvated electron population for different excitation yields corresponding to different pump fluences. These calculations are in good agreement with experiment, where the kinetics profiles are independent of the initial fraction of photogenerated iodine radical.

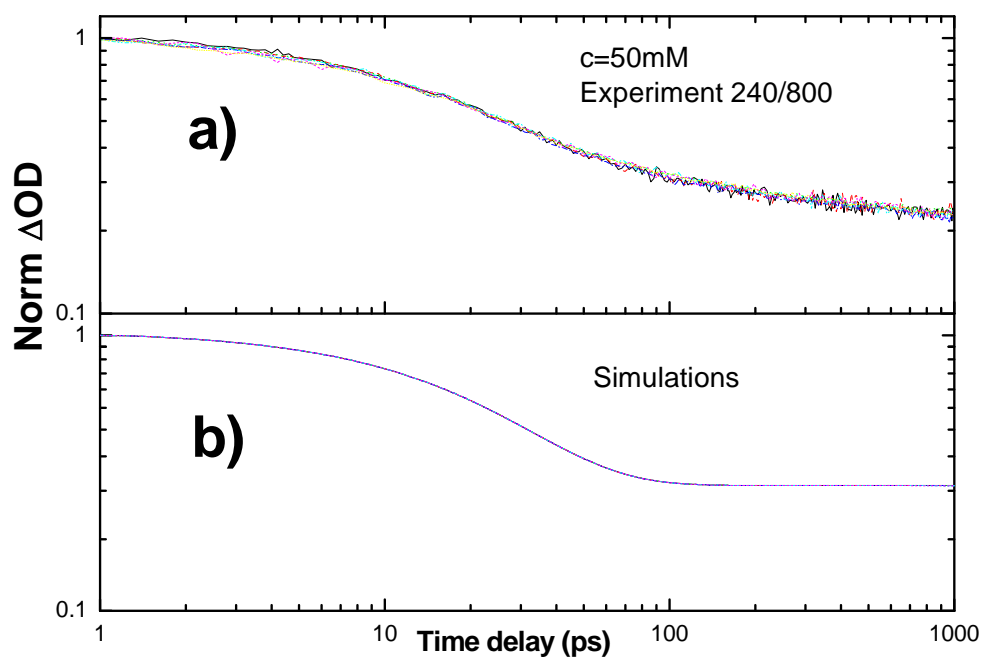


Fig. 5.4: a) Normalized transient absorption of the solvated electron for a 50 mM sample and pump fluences between of 13-75 mJ/cm². b) Theoretical solvated electron evolution of the same sample concentration at excitation yield 0.1-0.6 %, obtained by solving rate equations for reactions in Eq. 1.1-1.4 and Eq. 1.9-1.19. The data are displayed in double-logarithmic scale.



Table 5.2 Rate constants

	Rate constant (M ⁻¹ s ⁻¹)	Reference
k ₄	9.6x10 ⁹	From fit
k ₅	2.5x10 ⁹	¹⁰⁶
k ₆	1.5x10 ¹⁰	¹⁰⁷ , ¹⁰⁶
k ₇	5x10 ⁹	¹⁰⁷
K ₈	7.2x10 ²	¹⁰⁸
k ₉	9.1x10 ¹⁰	¹⁰⁹
k ₁₀	6.4x10 ⁹	¹¹⁰
k ₁₁	5x10 ¹⁰	¹¹¹
k ₁₂	3.5x10 ¹⁰	¹¹²

In order to investigate the dependence of excitation yield on the pump fluence and examine whether there is a nonlinear regime in the photodetachment, we plotted the transient absorption of the 800 nm probe at 1 ps time delay versus the pump fluence (Fig. 5.5). The yield of solvated electron is a linear function of the pump intensity. The contribution of the solvent to the signal via two-photon absorption is negligible as observed in the transient absorption of pure water at the maximum pump intensity. This excludes a scenario where Γ^- is driven beyond the CTTS state into continuum (i.e. two-photon excitation)¹³ but confirm that electron is generated when Γ^- is excited to the lowest state of CTTS band (one-photon excitation).

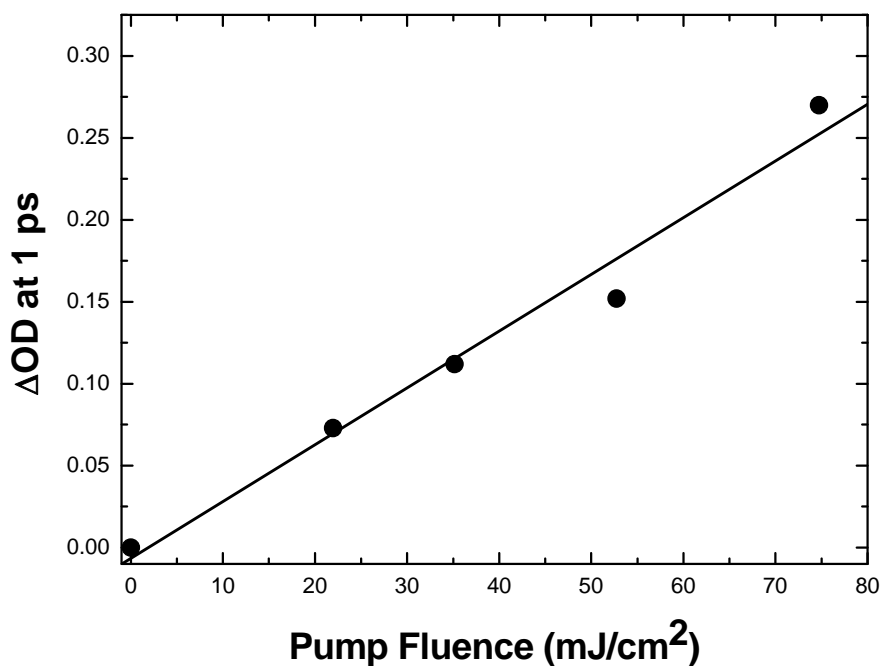


Fig. 5.5: Transient absorption of solvated electron at 1 ps as a function of pump fluence (solid circle). Solid line shows the linear fit to the data.

The decay of electron is independent of the pump intensity but it is a function of sample concentration at long time delay. As shown in Fig. 5.6a, below 100 ps the solvated electron exhibits roughly the same kinetics for a concentration ranging from 50-1000 mM. At early time after the photodetachment, the recombination rate of electrons with partners is mainly affected

by the separation between electron and iodine atom, the reaction radius of 5.8 Å obtained from the above analysis is much smaller than the iodide-iodide distance of ~12-32 Å for the corresponding concentrations 1000-50 mM. Therefore, the short-time dynamics are not influenced by sample concentration. However, when the subsequent products of the iodide detachment appear, the electron population decays faster in higher sample concentration. This is mainly due to the formation of polyiodide molecules which are the electron scavenger, as shown in Eq. 5.14-5.17. Fig. 5.6b qualitatively illustrates the sample concentration dependence of electron population.

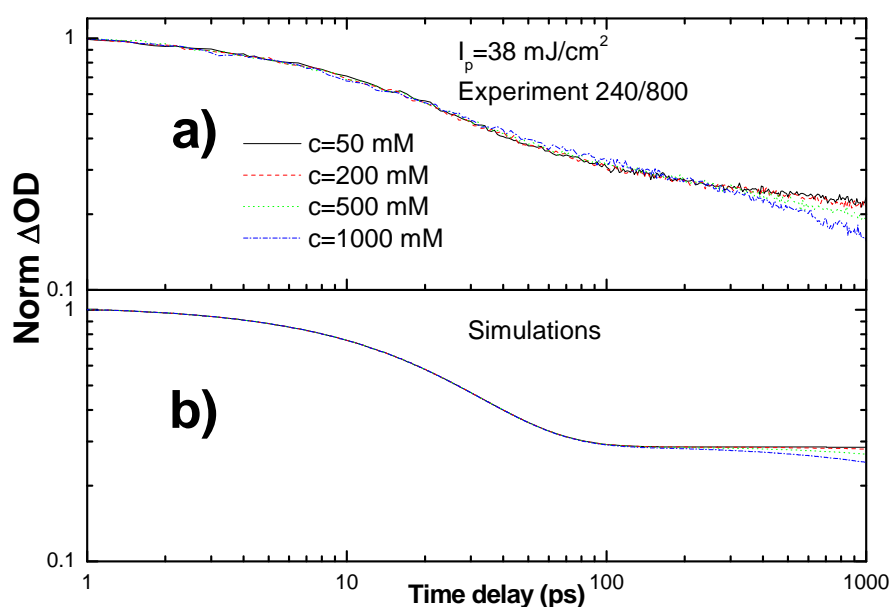


Fig. 5.6: a) Normalized transient absorption of solvated electron for sample concentrations of 50, 200, 500, 1000 mM, pump fluencies 37 mJ/cm². b) Population of solvated electron calculated for the experimental sample concentrations at excitation yield 0.6 %. The data are displayed in double-logarithmic scale.

5.3 Multiphoton excitation

5.3.1 Ultrafast kinetics of electron generated by multiphoton excitation in water

Before presenting the results of two-photon excitation in I^- , we start with the investigation of water at similar pump energies. Fig. 5.7a shows the evolution of electron probing at 800 nm upon 400 nm pump over a pump range of 292-850 mJ/cm². The spike appearing at 1 ps in all curves is from a short-lived precursor of the hydrated electron whose absorption spectrum in the near IR undergoes a rapid blue shift in the first 2 ps after photogeneration^{113,114,115,116}. The signals remain constant after the spike, the level of electron survival probability increase as a function of pump intensity. This is explained by the continuous red shift (at least till 50 ps) of the solvated electron absorption band with the increasing water temperature due to pump laser^{117,118}. From the temperature dependence of the electron spectra, Crowell *et al* parameterized the electron molar absorption as function of temperature and wavelength¹¹⁹. Using this function we calculated the electron molar absorption at 800 nm for temperature ranging from 20 to 80 °C. The curve from 20-55 °C can be approximately fit to a linear function $\varepsilon(t) = 15668 + 81 \cdot t$ with t being temperature. To estimate the temperature change in water when the pump fluence increases from 292 to 860 mJ/cm², we compare the difference of the real signal at 6.8 ps (where the electron thermalization is over) for 860 mJ/cm² pump with the signal of 292 mJ/cm² pump (rescaled to the maximum of the former curve at 1 ps) to estimate the temperature effect on the high pump intensity signal. In this treatment, we neglect the difference in the decay rate due to the different electron populations at 6.8 ps, this is acceptable because the rate constant for the electron recombination in bulk water is $3 \times 10^{10} \text{ M}^{-1} \text{ s}^{-1}$ ¹²⁰, which leads to a slow decay in the considered time scale. From the resulting molar absorption change due to temperature effect $\Delta\varepsilon \approx 1185 \text{ M}^{-1} \text{ cm}^{-1}$, we estimate a temperature change $\Delta t \approx 14.5 \text{ °C}$ from the above linear function. This is an average temperature over the 200 μm path length of the sample. In fact the temperature distribution is highly inhomogeneous along the pump path due to the multiphoton absorption. Crowell *et al* modeled the electron distribution, which has the same profile as a function of temperature, along the 400 nm pump direction, and estimated a water temperature increase of 28 °C at the surface of the sample for a pump fluence of 1.7 TW/cm² (corresponds to 528 mJ/cm²).

Fig. 5.7b shows the dependence of the signal at 1 ps on the pump intensity. A quadratic and a cubic function of pump intensity were used to fit the data. The cubic function shows a better agreement with the data than the quadratic function, with a sum of square error (SSE) for the cubic of 3.2×10^{-6} versus 1.2×10^{-5} for the quadratic one. This result indicates a three-photon excitation in water, which is in agreement with previous studies¹²⁰.

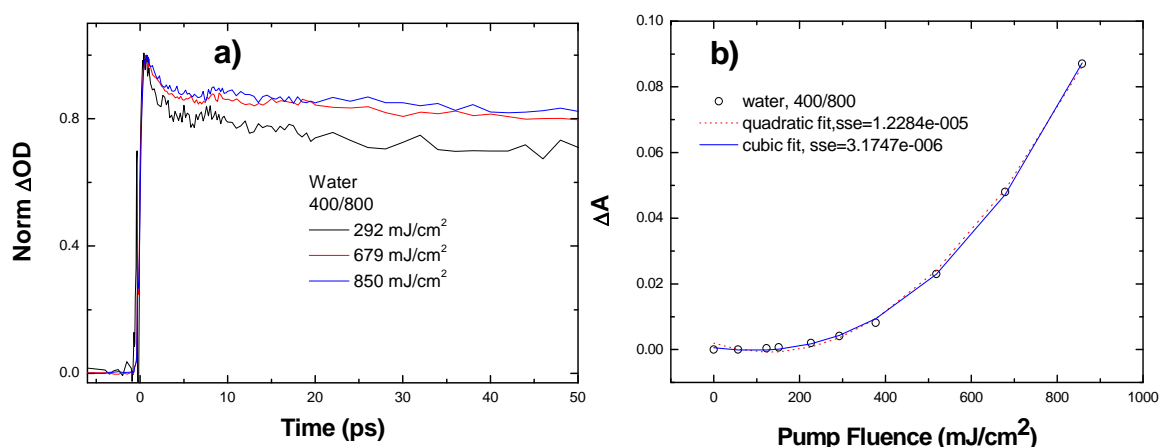


Fig. 5.7: a) Kinetics of electron in water under different pump fluences. The electron is probed at 800 nm under 400 nm laser pulse excitation. The sharp spike before time-zero is artifact. b) Pump fluence dependence of transient absorption at 1 ps, solid curve presents the fit with cubic function, dotted curve: quadratic function.

5.3.2 Ultrafast kinetics of electron generated by multiphoton excitation in aqueous iodide

Following the studies of multiphoton excitation in pure water, we present here our investigation of I^- anion in water under the similar pump conditions. Fig. 5.8a displays the electron kinetics probed at 800 nm upon 400 nm excitation of laser pulse in a range of fluence of 60-860 mJ/cm². These time traces are fitted with double-exponential decay functions. Decay times of the first and second terms are shown in Fig. 5.8b. Unlike one-photon excitation, the decay time of electron signal in this case is an increasing function of pump intensity. This finding is rather counterintuitive since a fast decay should appear in high pump power where an initially larger amount of electron is generated. One might concern that this is the result of the

initially spatial electron distribution. The larger separation between electron and iodine leads to the slower decay. However, the broadening of electron distribution is determined by the pump energy¹²¹. This happens when the number of absorbed photons increases at high pump power. The argument on the increasing electron spatial distribution is also excluded as it is evident from the pump intensity dependence of bleach I^- , presented in section 5.3.3. Temperature effect could explain the observed data. The following section discusses how temperature causes this behavior.

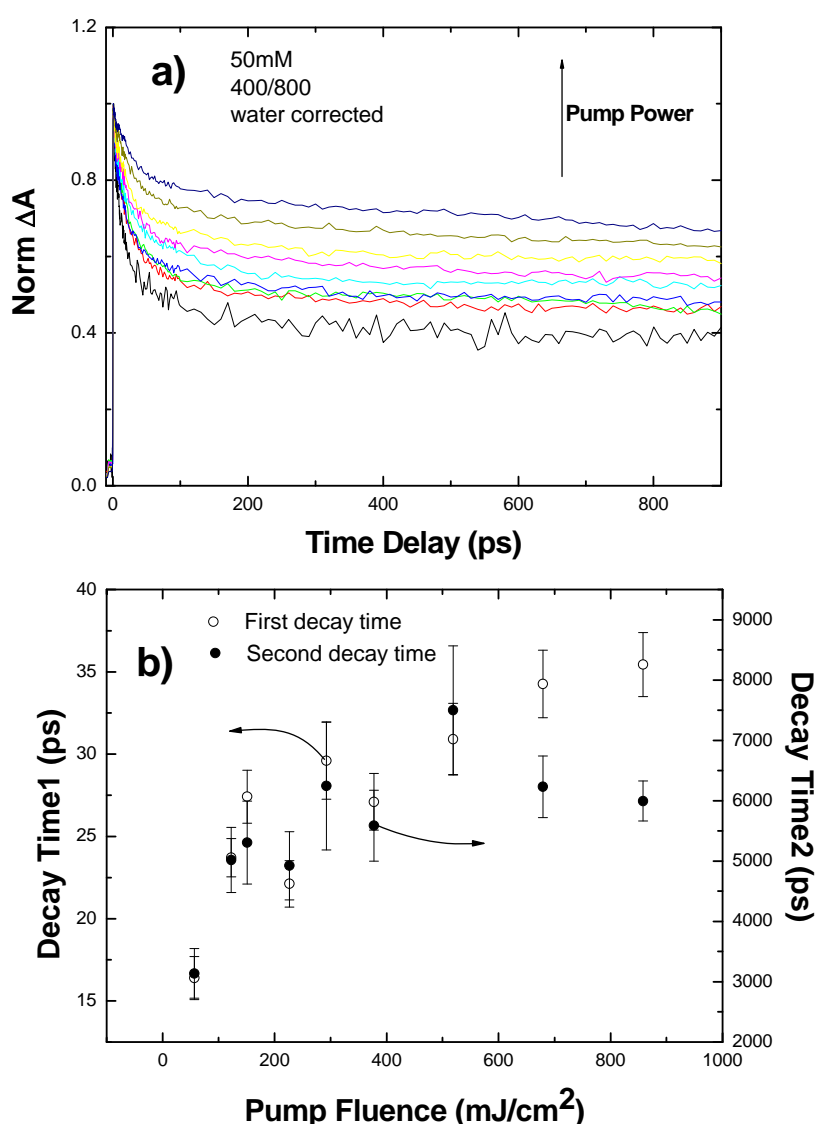


Fig. 5.8: a) decay profile of 400 nm pump 800 nm probe after correction from solvent contribution, pump intensity: 60-860 mJ/cm^2 (corresponding to the arrow) I^- concentration is 50 mM. b) decay time from double-exponential fit, open circle: first decay (left y axis) solid circle: second decay time (right y axis)

The level of remaining electron survival probability at long times is an increasing function of the pump intensity. A similar behavior was observed in one-photon excited electron signal of I^- in water, where the level of signal at long delay times is higher for the higher temperature of the solution under similar pump conditions¹⁹. It is believed that the red shift of the electron due to temperature increase is the origin of the decrease in decay rate and the high remaining signal of electron survival probability. As previously discussed, water temperature can increase by 14.5 °C when pump fluences increase from 292 to 860 mJ/cm², in the case of I^- the heat process can even be more efficient since the ejection of electron due to multiphoton absorption also releases heat into solvent bath. The finding presented in Fig. 5.8 can be qualitatively interpreted as the following: the water molecules which do not eject electron dump the pump energy as heat to the solvent bath, at the same time a multiphoton process in I^- also contributes electron and heat to the solution. After a blue shift of the pre-thermalized electron (in 2 ps) the electron absorption band is continuously shifted to the red¹²⁰, this causes a continuously increase in the electron signal compensating for the decrease due to the recombination. Even though the curves in Fig. 5.8 were corrected with the electron contribution from the solvent, we cannot correct for the temperature increase in the sample. Therefore, the higher pump intensity the slower the observed decay time. Based on the heat conductivity of water, Crowell *et al* estimated that a time needed for diffusive heat exchange to disappear is 0.3 ms in neat water. So, the temperature effect or red shift of the electron absorption remains in a sub-nanosecond measurement of the electron signal.

In order to examine the excitation mechanism, we show the transient signal of the electron at 1 ps over a range of pump intensities in Fig. 5.9. At high pump intensities the solvent considerably contributes to the signal due to three-photon process, this contribution is subtracted (presented by solid circle). The electron yield of the subtracted signal up to 520 mJ/cm² shows relatively the same fit quality between the quadratic and the cubic function of the pump fluences. At higher pump power, the yield tends to saturate, probably because of the nonuniform absorption of the 400 nm light in the jet. The high absorption of the 400 nm pump light near the jet surface could deplete the electron sources, while in the back of the jet, the pump intensity dramatically decrease generating less electrons. At this pump wavelength, it is possible that the detachment is similar to that of 312.5 nm pump, where two-photon absorption

regime is operative at low excitation intensity and three-photon absorption occurs at high pump intensity¹³. As also observed by Long and co-workers, a second rise after a first peak at early times are absent at 800 nm probe but it was seen at 625 nm probe¹³. The pump intensity dependence of the 625 nm probe time trace leads to a conclusion on the different excitation processes at high and low pump intensities in Long *et al* report. With our data is not possible to conclude whether two, three photon excitation or both processes happen in I⁻/water with 400 nm pulse laser excitation.

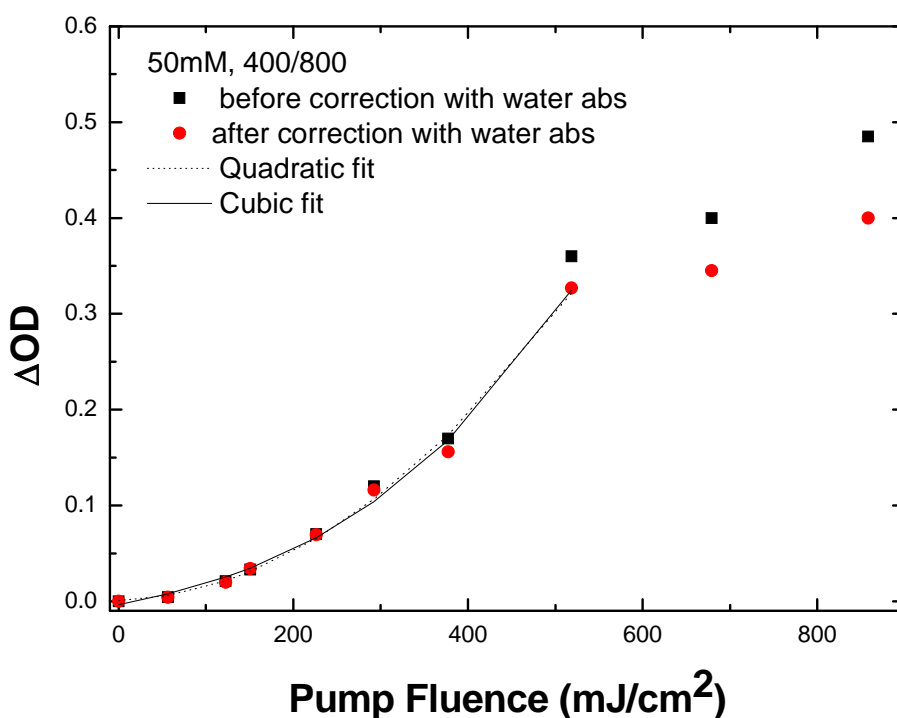


Fig. 5.9: Transient absorption at 1 ps plotted versus pump fluence. Square solid is raw data, circle solid is signal after subtracting solvent contribution. Dotted and solid curves present quadratic and cubic function fit, respectively. The fitting range is 0- 520 mJ/cm².

5.3.3 Transient bleach of aqueous iodide

One of our main goals for measuring the electron yield under 400 nm pulse laser excitation is to derive the excitation yield at the same pump condition in x-ray probe experiment. Because the electron profile shows strong thermal effect, it is not possible to get a true excitation yield at long decay times where the signal is contaminated by temperature effect induced by the pump pulse. On the other hand, even though the electron contribution from the solvent is subtracted by measuring the signal from the pure solvent, it is not guaranteed that the solvent with I^- has the same absorption cross section as the pure solvent. Another way to determine the excitation yield is to look at the bleach signal of I^- . Fig. 5.10 displays the bleach signal of the iodide anion at 240 nm on the CTTS band for 400 nm pump. The transient absorption is normalized at the maximum bleach, the double peaks near time zero are due to cross phase modulation, where pump and probe pulse overlap. The negative signal clearly indicates the loss of iodide anion due to the photodetachment. Though it is partially covered by the artifact near time zero, we found that the recovery time of the bleach signal is an increasing function of the pump intensity. The bleach signal at 240 nm is calculated using rate constant k_p , k_n and k_d for the one-photon excitation (section 5.2). The theoretical signal (dotted curve in Fig. 5.10) shows a much slower recovery time than the experiment. This behavior is a result of a red shift of the CTTS band due to the increasing temperature²³, which was observed in our UV-VIS measurement (Fig. 5.11a). In Fig. 5.11b we plot the extinction coefficient at 240 nm as a function of temperature, extracted from Moskun et al.'s data. The fact that the bleach signal recovers faster than the predicted one is a consequence of the increase in the absorption coefficient due to the laser-induced temperature increase in the sample. In principle, the higher pump intensity causes the faster recovery of the bleach but this is not the case in Fig. 5.10. In fact, this behavior originates from the inhomogeneity of pump absorption along the pump axis due to multiphoton absorption. This inhomogeneous pump absorption leads to a hot portion in the front part of the jet while a much lower temperature of the solution is present in the back of the jet. The concentration profile of photoelectrons generated by 400 nm laser pulse along the pump axis is calculated by Crowell *et al* for various pump intensity¹²⁰. For a pump intensity equivalent to 515 mJ/cm^2 , the electron concentration at the surface is 90 mM whereas the mean concentration across the $90 \text{ }\mu\text{m}$ jet is 15.5 mM. In our measurement, the pump fluences are varied from 280-1200 mJ/cm^2 , the jet thickness is $200 \text{ }\mu\text{m}$ which is larger than their value, thus

the temperature effect on the bleach signal is even more pronounced. In a qualitative explanation, at low pump intensity the measured signal, which is an averaged profile over sample depth, get more temperature effect than at high temperature. As a matter of fact, averaging the bleach signal with temperature effect over the sample thickness with temperature profile provided by Crowell *et al*¹²⁰ could explain the data in Fig. 5.10.

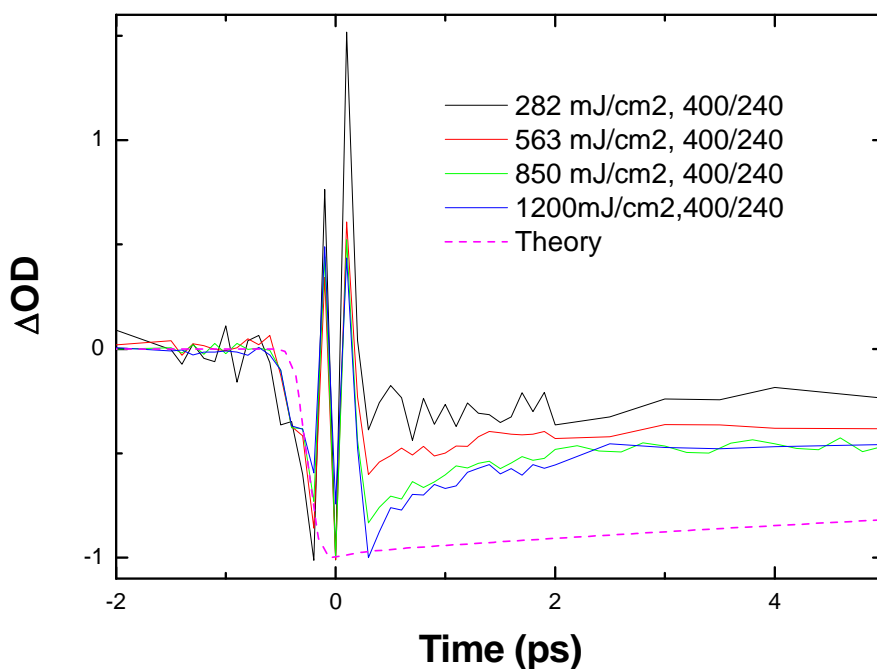


Fig. 5.10: Kinetics of I- bleach probing at 240 nm for 400 nm pump laser at various pump fluence. The double peak at time-zero is artifact due to cross phase modulation.

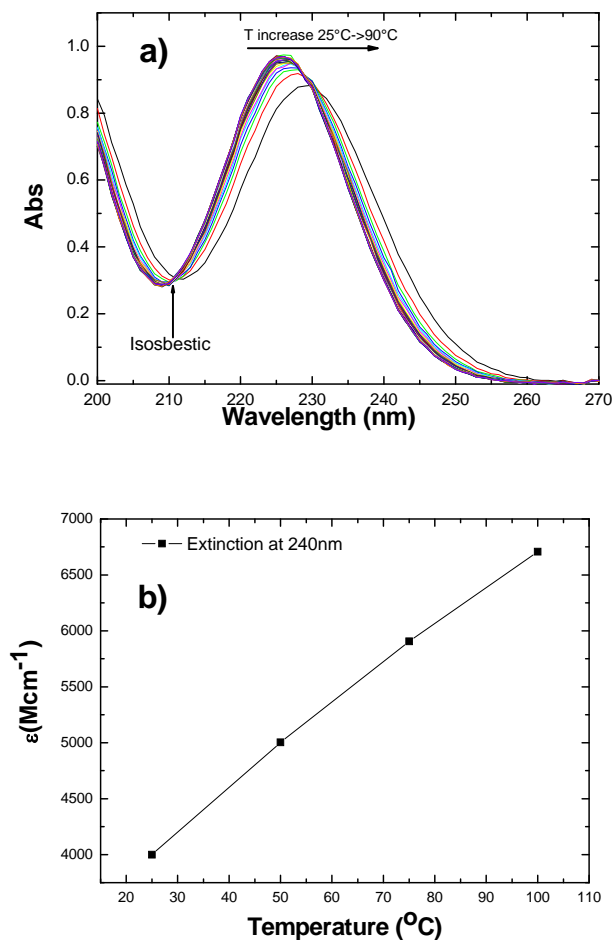


Fig. 5.11: a) absorption of CTTS band for temperature 25-90 °C. The arrow indicates the shift direction of CTTS band when the temperature increase. b) extinction at 240 nm as function of temperature (source: ²³)

From the bleach signal one can determine the portion of bleached I^- using the formula for the absorption change $\Delta OD = \varepsilon \cdot \Delta c \cdot l$, where ΔOD , ε , Δc and l are transient bleach signal, molar absorptivity, bleach concentration of I^- and sample thickness, respectively. At early times, Δc equals to the concentration of photogenerated iodine atom, the fractional excitation can be calculated by $f = \Delta c / c$ with c being the sample concentration. Fig. 5.12 displays the excitation yield at ~ 0 ps versus pump fluence, in this data the contribution of water is subtracted. At the highest pump fluence 1.2 J/cm^2 , the sample is excited by 4.5%. The curve tends to bend over at

high pump intensities, the origin of this behavior is analogous to one observed with 800 nm probe. Our aim is to find the excitation yield at 1.7 J/cm^2 , used in the x-ray experiment. However, due to the limitation of laser power the pump condition at x-ray experiment could not be reached, and we anticipate a yield close to 4.5% by extrapolation.

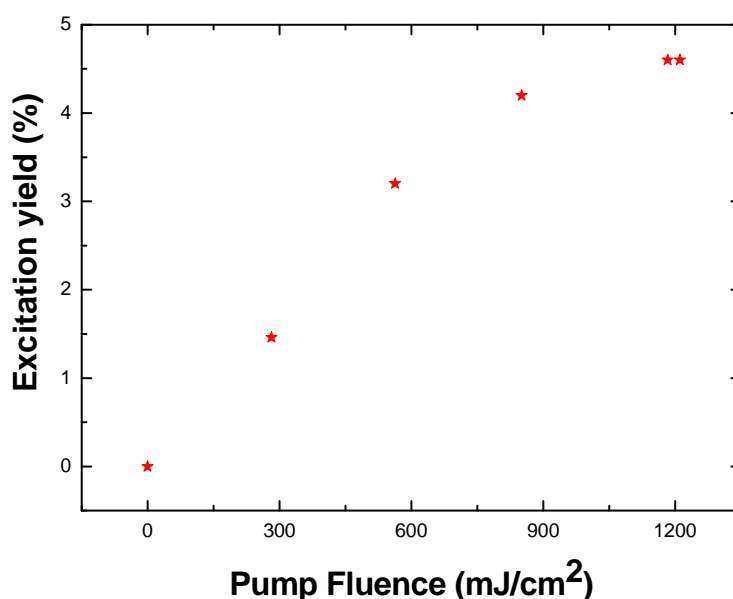


Fig. 5.12: Excitation yield derived from Fig. 1.10 (after subtracting the contribution of solvent) as function of pump fluence extracted from the I^- bleach at 240 nm for ~ 0 ps time delay.

The temperature effect at both probing wavelength is an obstacle to estimating the electron yield under multiphoton excitation. The induced-temperature not only causes a spectral shift but it also changes the diffusion properties of electron¹⁹. However, it is believed that the heat energy is not sufficient to change the ejection distance of the electron. Fig. 5.11a shows that there is an isosbestic point crossing the red-shifted CTTS band. Probing iodide bleach at this point will reveal the kinetics of iodine radical free from thermal effect. Fig. 5.13a shows the bleach signal at the isosbestic point 211 nm for pump fluencies ranging 150 – 300 mJ/cm^2 . The fact that the signal shows the same profile at different pump intensities indicates that the curves track a real population of bleached I^- , it also implies that within the excitation range, the

reaction radius between iodine and electron is the same. Fig. 5.13b shows the profiles at different sample concentrations, within 160 ps the kinetics of 10, 20 and 50 mM I⁻/water are very similar.

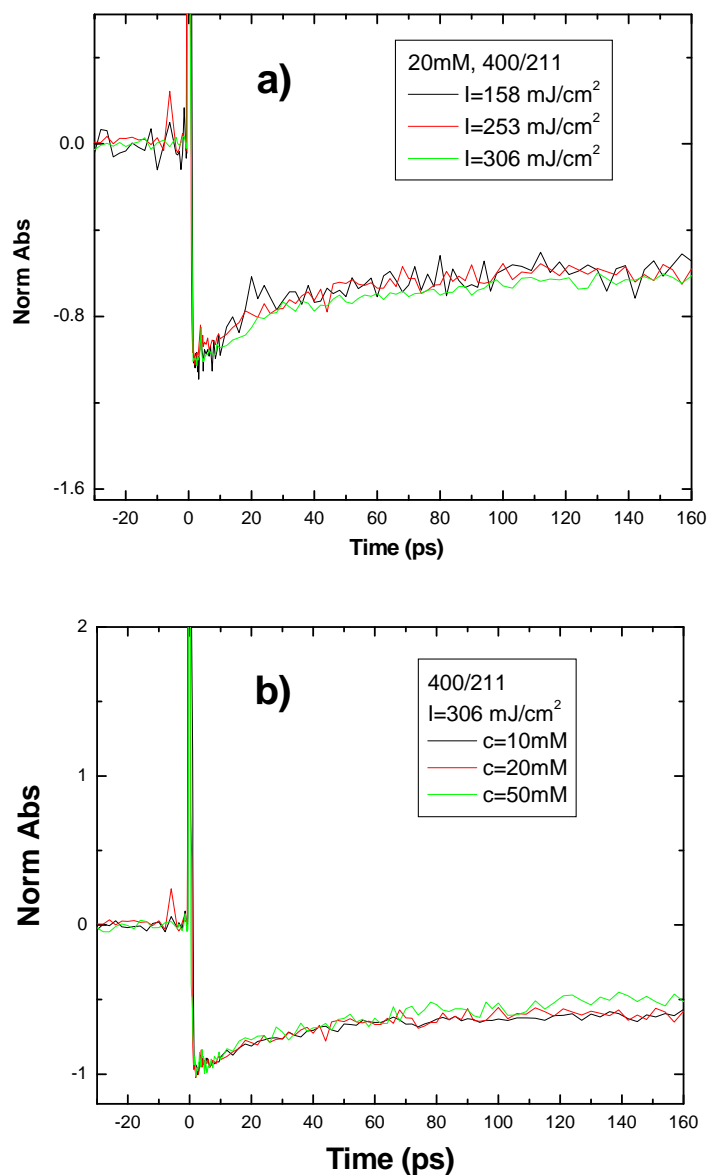


Fig. 5.13: Temporal evolution of I⁻ bleach at 211 nm upon 400 nm excitation for various pump fluences ranging 158 to 306 mJ/cm², at sample concentration of 20 mM (a), and I⁻ bleach for various sample concentrations 10-50 mM pump power ~306 mJ/cm² (b)

The I^- bleach signal of 20 mM sample is fitted using rate equation Eq. 5.5 with the fit range of 1.4-160 ps. Since the early time data is excluded (due to the time-zero artifact), we assume that the appearance time of the electron is the same for one-photon excitation where $k_p^{-1} = 200 \text{ fs}$. The fit is shown in Fig. 5.14, the resulting best fit parameters are $k_d^{-1} = 56.4 \pm 6.7 \text{ ps}$, $k_n^{-1} = 97.9 \pm 7.2 \text{ ps}$. Contrary to one-photon excitation, the non-adiabatic recombination rate is smaller than the dissociation rate, this is a consequence of a broader spatial electron distribution in multiphoton excitation²².

In order to study subsequent reaction after I^- photodetachment, we probed the I_2 population at 419 nm, which is in the middle of its first absorption band (Fig. 5.1). The time trace at 419 nm (400 nm pump) is fitted with rate equations for the full chemical reactions. I_2 is formed mainly via $I + I^- \rightarrow I_2^-$, its rate constant is a free parameter for the fit, other rate constants are taken from the resulting k_p , k_n , and k_d of I^- bleach and the reported values. The transient signal at 419 nm is contributed by the electron and I_2 . The signal is expressed by

$$S_{419}(t) = \varepsilon_{419}^e \cdot c_e(t) \cdot l + \varepsilon_{419}^{I_2^-} \cdot c_{I_2^-}(t) \cdot l \quad (5.18)$$

where ε_{419}^e , $\varepsilon_{419}^{I_2^-}$ are extinction of electron and I_2 at 419 nm, $c_e(t)$ and $c_{I_2^-}(t)$ are concentration of electron and I_2 resulted from rate equation, l is sample thickness. Fig. 5.15 shows the fit of kinetics at 419 nm, the resulting excitation yield of 0.46% is in good agreement with the value estimated from electron signal at 570 nm (in the same measurement where the transient absorption is probed by the white light continuum), the reaction rate $k_4 = 9.6 \times 10^9 \text{ M}^{-1} \text{ s}^{-1}$ for the above reaction is in good agreement with the published values, which are in a range of $8.8 \times 10^9 - 1.2 \times 10^{10} \text{ M}^{-1} \text{ s}^{-1}$ ^{107,112}.

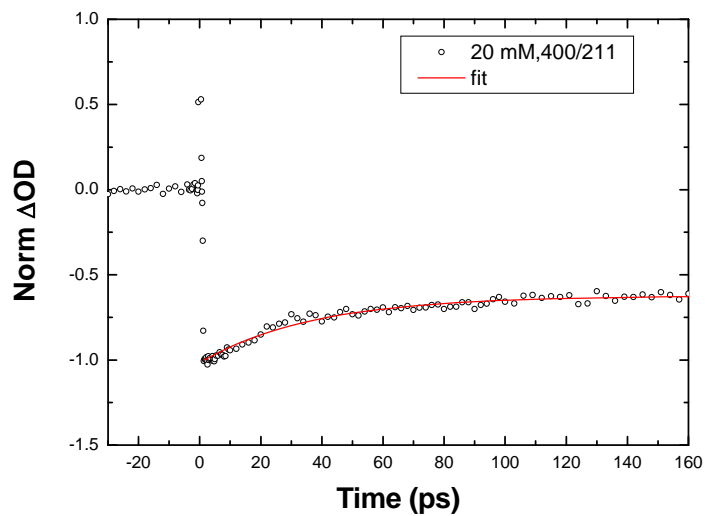


Fig. 5.14: I^- bleach signal at 211 nm upon 400 nm pump (open circle) and fit (red solid) using Staib-Borgis model .

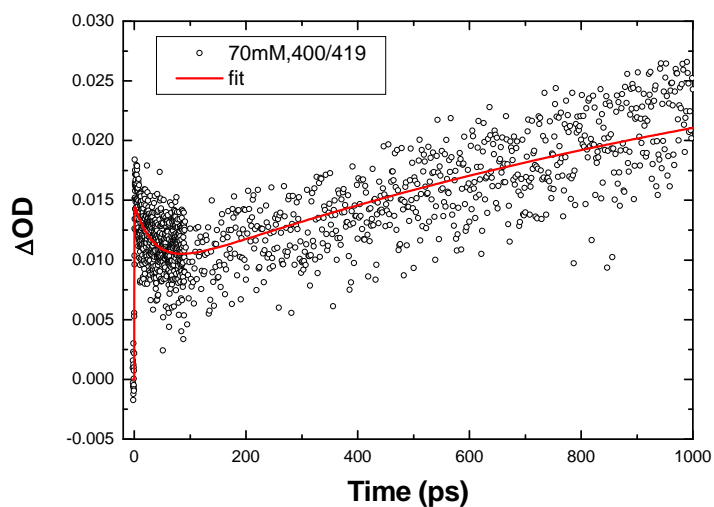


Fig. 5.15: Transient absorption at 419 nm following a 400 nm excitation (open circle) and fit using kinetics model which includes all chemical reactions.

5.4 Conclusions

We observed a similar time trace at 800 nm for one-photon 240 nm excitation to previous study¹⁵. The best fit parameters using kinetics model $1/k_p = 0.19 \pm 0.04$ ps, $1/k_n = 29.3 \pm 1.1$ ps,

$1/k_d = 76.9 \pm 3.7$ ps are comparable to previous reported values¹⁶. The MFP model delivers consistent values of reaction rate with the kinetics model. The resulting Onsager radius of 5.8 Å is larger than the reported value 4.4 Å for 225 nm pump²² but comparable to the value of Laubereau group¹⁹.

The multiphoton excitation using 400 nm pump laser induces a temperature jump in the sample. The heat shifts the electron and the CTTS bands to the red increasing the molar absorptivity making it difficult to find a real solvation dynamics. The estimated temperature increase in neat water when the pump increase from 292 to 860 mJ/cm is ~14.5 °C. A similar temperature is predicted in 50 mM I⁻/water which increase the decay time of electron transient absorption signal with pump intensity. The transient absorption at 1 ps of the timetrace at 800 nm as a function of pump intensities indicates a comparable possibility of two and three photon absorption under 400 nm pulse laser excitation (Fig. 5.9). The kinetics of bleach iodide at 240 nm probe shows different recovery times for various pump intensities. The increasing recovery time with the pump power is a consequence of the highly inhomogeneity of pump photon distribution along the pump axis. The pump fluence dependence of the transient bleach signal predicts an excitation yield close to 4.5% in the x-ray experiment at 1.7 mJ/cm². A recombination and dissociation rate of iodine and electron are found by fitting I⁻ bleach at the isosbestic point of the CTTS band 211 nm. The resulting $k_d^{-1} = 56.4 \pm 6.7$ ps, $k_n^{-1} = 97.9 \pm 7.2$ ps reflects a slower recombination than the dissociation of I:e contact pair as a result of broaden electron distribution which is in contrary with one-photon excitation. The reaction rate of iodine radical with iodide, $k_4 = 9.6 \times 10^9$ M⁻¹s⁻¹, found to be in good agreement with previous studies.

Chapter 6 Picosecond-resolved x-ray absorption spectroscopy

6.1 Introduction

In this chapter, we present our study on electronic and structural change of iodide upon multiphoton excitation with 400 nm laser pulses probed by transient x-ray absorption spectroscopy. The chapter is composed of two main sections: electronic properties at the L_1 – edge and structural properties measured at the L_3 -edge.

6.2 Electronic properties

6.2.1 Transient XANES around the Iodine L_1 edge

A main part of this thesis deals with the photogeneration of nascent iodine radicals in water, following the reaction



using 400 nm light. Since the photon energy is much lower than the lowest excitation CTTS band (see chapter 1), photogeneration of iodine atoms is a multiphoton process, with n photons. It is not easy to precisely quantify the yield of this reaction in a real experiment, since many factors contribute, including small variations in lateral pump beam profile. In addition, the iodine atom itself is hardly detectable (only in the deep UV ²³) in an optical experiment, and relying on the intense absorption of the solvated electron throughout the UV-vis offers only an upper limit of this yield, since multiphoton ionization of the neat solvent may also contribute under such excitation conditions. In Chapter 5, we have measured the photoinduced bleach signal of the iodide CTTS absorption, which – according to Eq. 6.1 – reflects the amount of photogenerated atoms, but this applies only in the absence of other absorption bands, which is often not the case. For example, the solvated electrons still absorb around 230 nm, and leading to some uncertainty in the determination of the atomic concentration from such optical measurements.

In consequence, while we can establish some boundaries for the neutral atom concentration, we cannot deliver its precise value under the pump-probe conditions used in the x-ray

experiments. This concentration, however, is vital for generating the photoproduct x-ray absorption spectrum, and therefore we employed different methods to extract its value to the highest precision possible, which are described below.

A representative set of transient absorption at various time delays at the iodine L_1 -edge is displayed in Fig. 6.1, along with static iodide XAS at the L_1 edge for comparison.

The transient spectra show positive and negative features near 5185 and 5192 eV. The positive peak arises from a resonant $2s \rightarrow 5p$ transition upon the electron ejection from the $5p$ orbital of iodide by the laser pump pulse. The transient spectra show an apparent peak shift and broadening for both transient features with increasing time. This is due to the formation of subsequent products, predominantly I_2 formation. The time dependence of the new absorption at 5184 eV is displayed in Fig. 6.2. A heuristic single-exponential fit $y = I_0 \cdot \exp(-(t - t_0) / \tau)$ of this curve delivers a time constant of ~ 1 ns, which is in line with the rate constant for reaction Eq. 6.1 for $c_0 = 100$ mM (1.04 ns). The $2s \rightarrow 5p$ transition of the solvated iodine atom disappears due to atom-electron recombination and formation of diiodide. However, diiodide has a corresponding transition $2s \rightarrow \sigma_u$, which experiences a blue shift with respect to the free atom (Fig. 6.3). This is responsible for the gradual peak shift of this transient absorption.

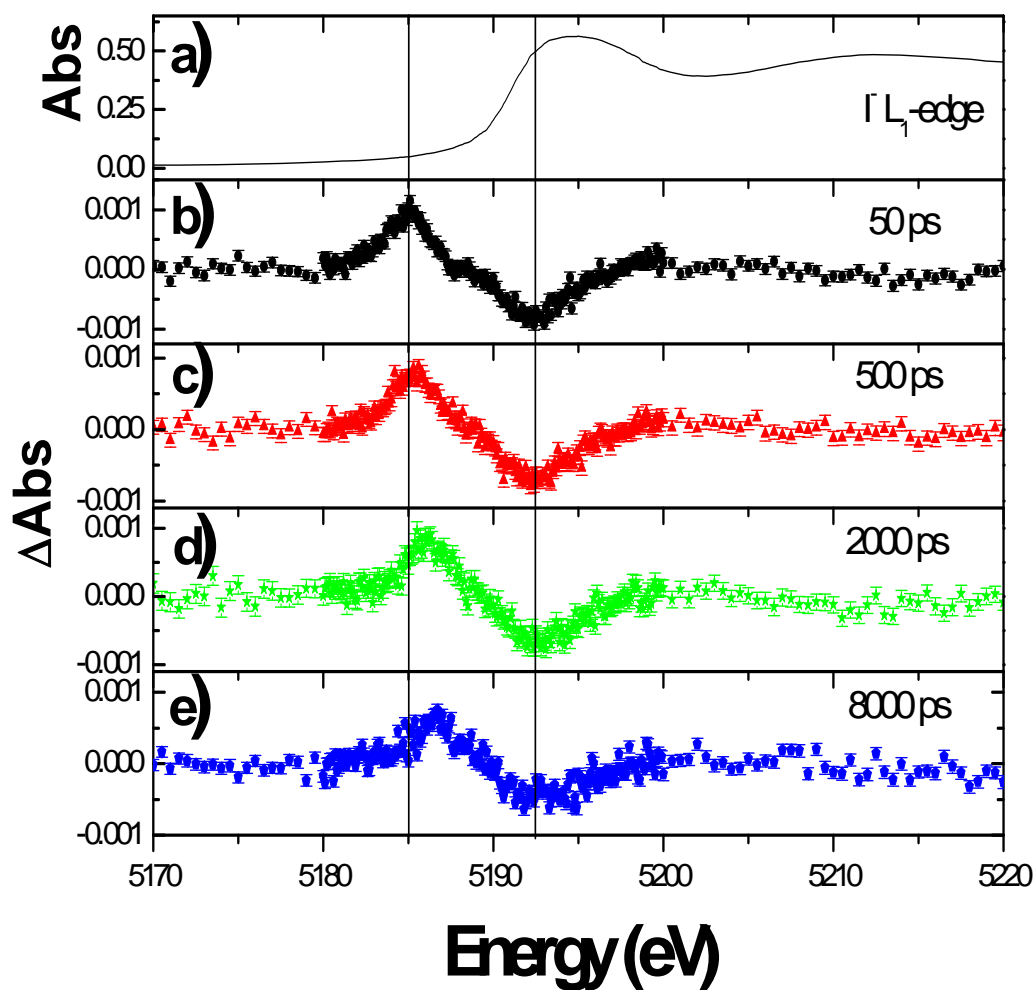


Fig. 6.1: a) static $I L_1$ -edge, b) transient absorption spectra at different time delays. The vertical lines indicate the positions of the max positive and negative peak positions for the transient at 50 ps. The transient absorption spectra are measured with a pump fluence of 1.7 J/cm^2 at 400 nm for a sample of 50 mM I^- in a free flowing jet of $\sim 280 \text{ }\mu\text{m}$ thickness.

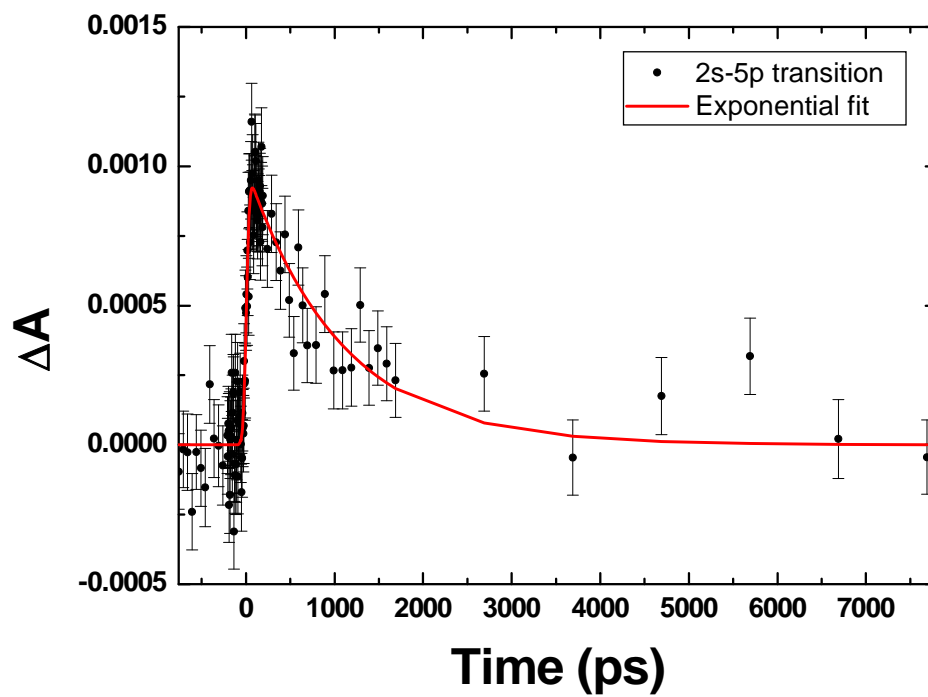


Fig. 6.2: Time trace probed at 5184 eV corresponding to 2s-5p transition of 100 mM sample, solid line shows a simple exponential fit.

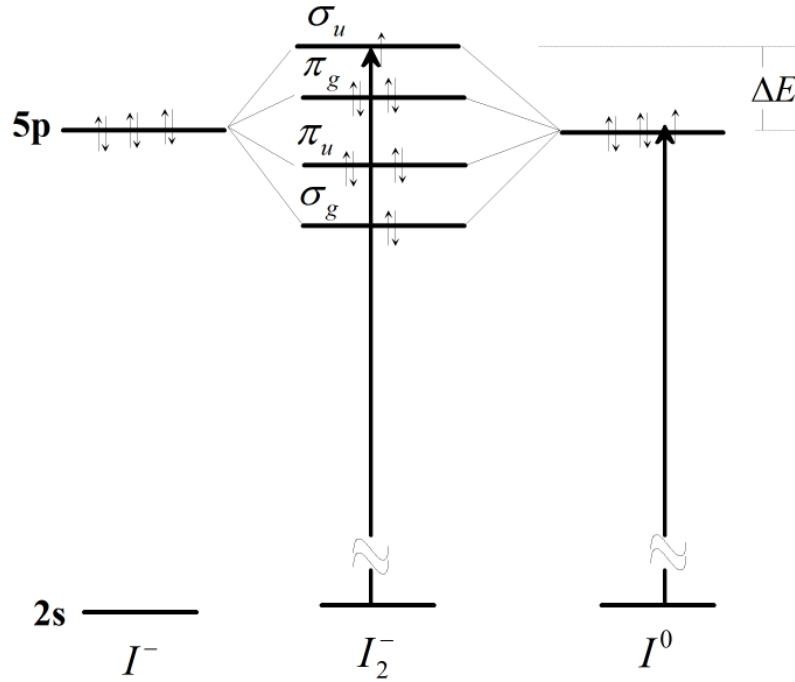


Fig. 6.3: A schematic energy diagram of I_2^- formed by the combination of six electrons of I^- and five electrons of I^0 atom.

The 400 nm pump/white light continuum probe experiments show that up to 50 ps the only photoproducts of iodide detachment are the iodine radicals and the electrons for a sample concentration of 50 mM, the subsequent product I_2 comes into play after 500 ps. The positive peak of the transient absorption at 50 ps is attributed to only I^0 , whereas at later times the peak is superimposed with contributions of I_2 and I_3 , resulting in a broadening. From this data, and knowing the absorption cross section of the species I^0 , I_2 and I_3 , we can extract the population of each species, thereby tracking their population kinetics. The transient absorption ΔA at a given time delay can be expressed as:

$$\Delta A(E, t) = (c_{I^-}(t) \cdot \varepsilon_{I^-}(E) + c_{I^0}(t) \cdot \varepsilon_{I^0}(E) + c_{I_2^-}(t) \cdot \varepsilon_{I_2^-}(E) + c_{I_3^-}(t) \cdot \varepsilon_{I_3^-}(E) - c_0 \cdot \varepsilon_{I^-}(E)) \cdot l \quad (6.2)$$

where ε_X ($X = I^-, I_2^-, I_3^-$) are the extinction coefficients of I^- , I_2^- and I_3^- , respectively. $c_X(t)$ are the time-dependent concentrations of species I^- , I_2^- and I_3^- , l and c_0 are sample thickness and reactant sample concentration, respectively. At 50 ps, the sample contains only I^- , I^0 and the solvated electron, which is silent in the x-ray domain. Equation 6.2 can be approximated as

$$\Delta A(E, 50 ps) = c_{I^0}(50 ps) \cdot (\varepsilon_{I^0}(E) - \varepsilon_{I^-}(E)) \cdot l \quad (6.3)$$

Based on this equation, one can calculate the absorption spectrum of I^0 if the concentration c_{I^0} is known. To have an idea about the shape of I^0 we depict its spectrum for three different concentrations of iodine (Fig. 6.4). Excitation yield f at time zero is calculated from c_{I^0} at 50 ps by the rate equations. As can be seen, the intensity of the resonant peak is larger for a smaller excitation yield, while the edge jump remains constant, as expected. The smaller excitation yields also cause the edge to shift slightly more to the blue, at the same time the dip between the edge and pre-edge peak become deeper, and even negative which is unrealistic. A detailed analysis on the dip values is presented in section 6.2.3. The negative feature in the transient absorption spectra (Fig. 6.1) is responsible for the blue shift and the dip in the I^0 spectrum.

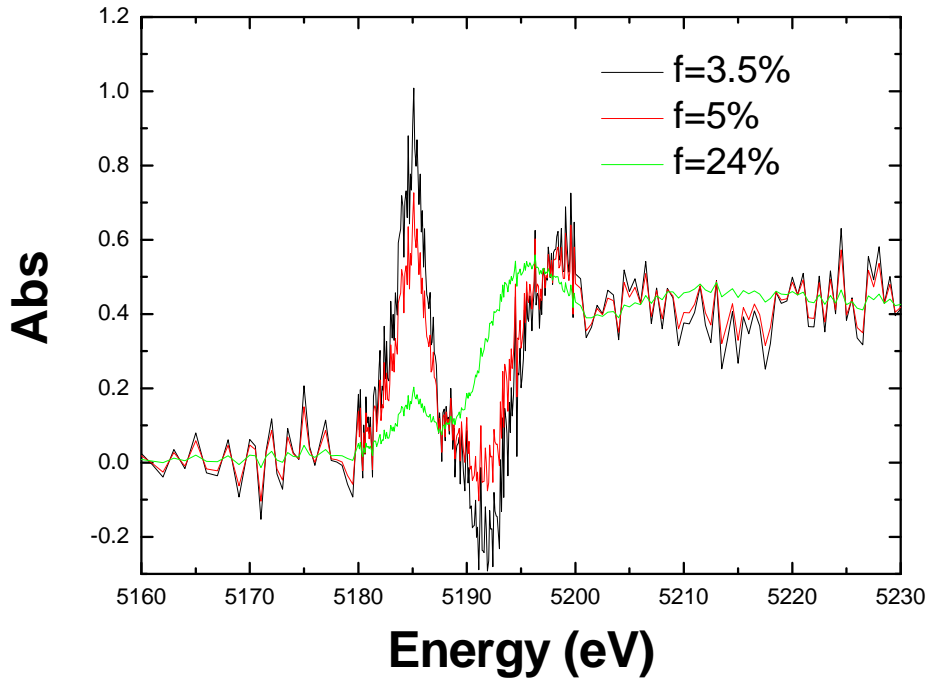


Fig. 6.4: Three possible scenarios for the I^0 spectrum for time zero excitation yield of 3.5, 5 and 24%. The black curve ($f=3.5\%$) shows a unrealistic spectrum, condition to make a reasonable spectrum is $f \geq 5\%$.

6.2.2 Simple fit procedure for determining the XANES of atomic iodine

The excitation yield is an important factor for determining the absorption cross section of I^0 . In principle, this factor could be derived from the all-optical pump-probe measurements (see chapter 5), but in our case it is unknown due to the limitations of pump power. We exploit the fact that the transient XANES after 50 ps consists of only the reactant iodide and atomic iodine atoms, and we fit the spectrum using a simple model. Hereby we assume that the iodide spectrum consists only of an edge step (lifetime broadened) and we include a Gaussian-shaped peak to mimic the first MS feature at 5194.5 eV (Fig. 6.5).

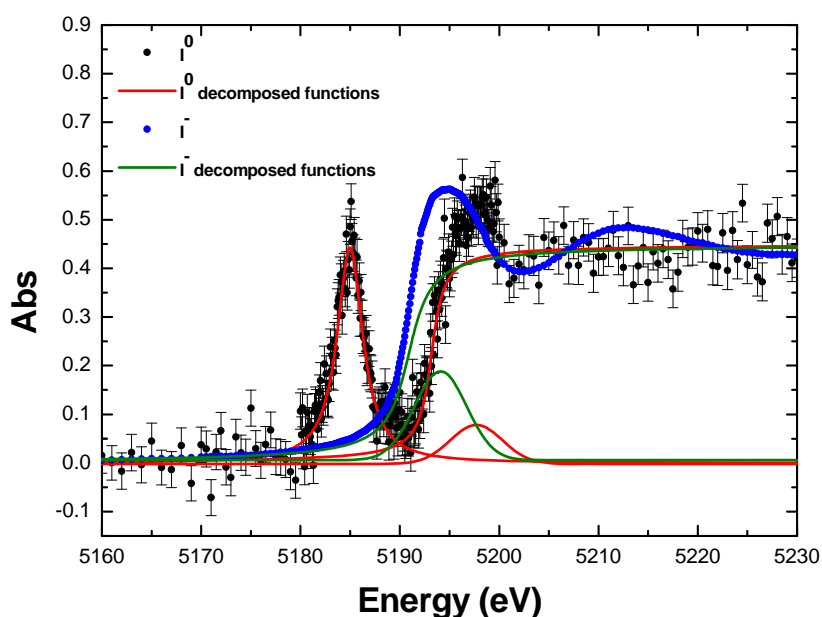


Fig. 6.5: Fit of I^0 and I^- spectra using a superposition functions. I^- (blue curve) is modeled with an Arctan and a Gaussian functions (dark green curves). I^0 (black scatter) is modeled with a superposition of a Lorentzian, an Arctan and a Gaussian functions (red curves).

For the atomic spectrum we assume a Lorentzian function for the $2s \rightarrow 5p$ transition, and a shifted edge step (arctan) and Gaussian MS feature (can shift in energy and in amplitude). Interestingly, this fit minimizes the square residuals when applying these functions to Eq. 6.3 to calculate the transient XANES (Fig. 6.6b). In this figure, the χ^2 values are calculated by varying the I^0 concentration keeping all other parameters fixed to the best fit values. The

resulting excitation yield is $f = 7 \pm 4\%$ with a confidence level of 95% (Fig. 6.6b). The best fit of the transient spectrum is shown in Fig. 6.6a. The iodine XANES spectrum, generated from the resulted best fit values is shown in Fig. 6.5.

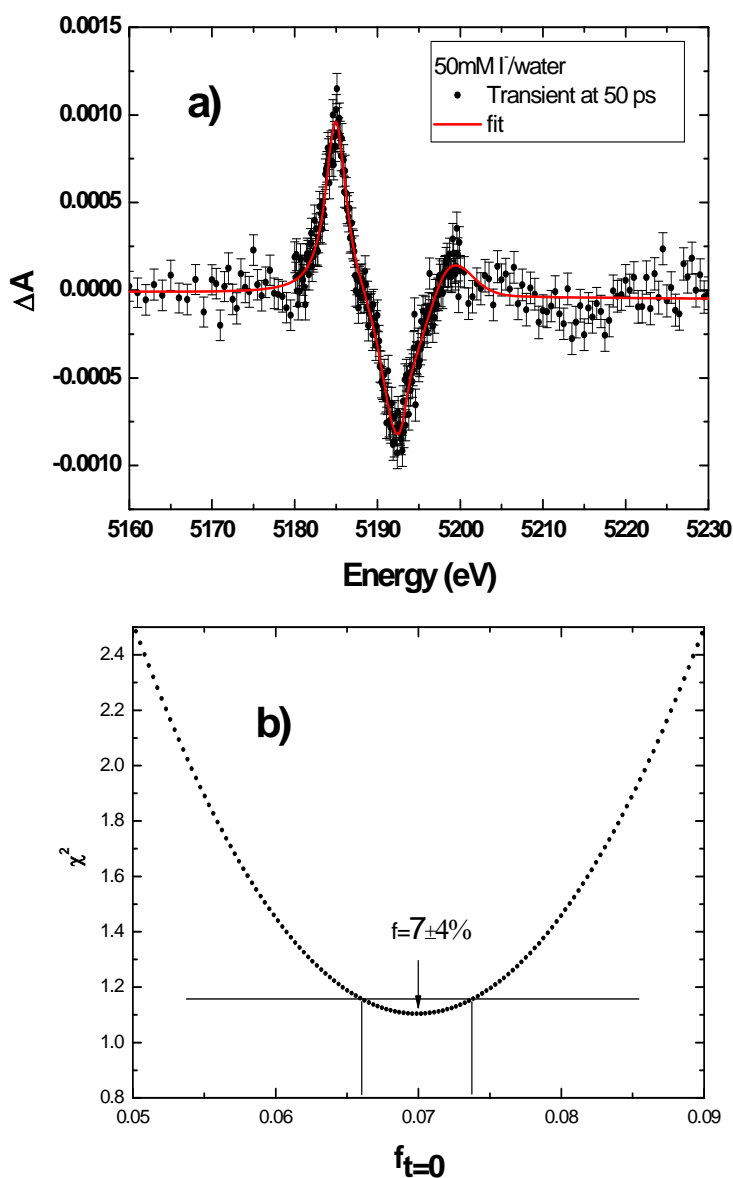


Fig. 6.6: a) Transient absorption at 50 ps and its best fit. b) dependence of χ^2 on the excitation yield.

Thus we obtain from this fit the following parameters (Table 6.1)

Table 6.1: Fit results using simple fit, the parameters are resulted from fitting I^0 spectrum (Fig. 6.5) with excitation yield obtained from Fig. 6.6b

	I^-	I_3^- ^a	I_2 ^b	I^0
Atomic peak (eV)	-	5188.4	5188.4	5184.97
Ionization potential (eV)	5190.9	5192.1	5194.3	5193.19
Area of atomic peak normalized to I_2		2.34	1	0.8
FWHM of atomic peak (eV)		3.17	3.03	3.15
FWHM of edge (eV)	1.66	1.5	1.35	0.93
Edge jump normalized to I_2	0.98	3.02	1	0.96
Binding energy of 5p orbital (eV) ^b	-	3.7	5.9	8.2

^a The spectrum of I_3^- is derived from static measurement of a solution of I_3^- and I^- , where the concentration ratio of the two species is known. ^b The I_2 spectrum is obtained from static measurement of I_2 solid mixed with BN.

^b Binding energy is determined by the difference of the edge position and the atomic peak position.

The model we used is only approximate, since it disregards the detailed origin of the XANES spectra: while the edge step and peak functions are fairly accurate, the MS features are merely heuristically taken into account. Nevertheless, the agreement is startling, and can serve as a starting point for a more thorough analysis, which we perform next.

6.2.3 Fitting the temporal evolution of the Iodine L_1 pre-edge peak

Another strategy to derive the excitation yield is based on the decay rate of the kinetic trace of Fig. 6.2 and on the solution of the rate equations to determine the initial population of photogenerated iodine radicals. The fitting strategy for the time scan is illustrated by a flowchart of Fig. 6.7. In this fit, the two free parameters are the excitation yield f and the time zero t_0 .

1. We start with an initial guess for the excitation yield of the 50 mM sample, the concentration of I^0 , c_{I^0} is then calculated from the rate equation.
2. The molar absorption of iodine, ε_{I^0} is obtained via Eq. 6.3.
3. From the ε_{I^0} and the transient absorption of 100 mM sample, we extract the concentration of I^0 generated at 50 ps in this sample, from which we determine the initial excitation yield based on rate equation. The I^0 and I_2 concentrations at 2 ns are calculated for the resulting initial excitation yield.
4. With these parameters and the transient absorption of 100 mM sample at 2 ns, the absorption cross section of I_2 is determined via Eq. 6.2, with the assumption that the I_3 concentration at 2 ns is negligible.
5. Once the absorption cross section of I^0 , I_2 and I_3 (from the static measurement) are found, the time-dependence of the signal at 5184 eV is computed via Eq. 6.2 with $c_X(t)$ obtained by solving rate equation for the initial excitation yield in 100 mM sample, which is obtained in step 3.
6. The calculated signal is compared with data via the χ^2 value. The residual is then minimized by adjusting initial guessed f and time zero.

Note that the cross correlation of 70 ps is implemented as FWHM of the propagated Gaussian pump pulse in the rate equation (see Eq. 5.5 in chapter 5).

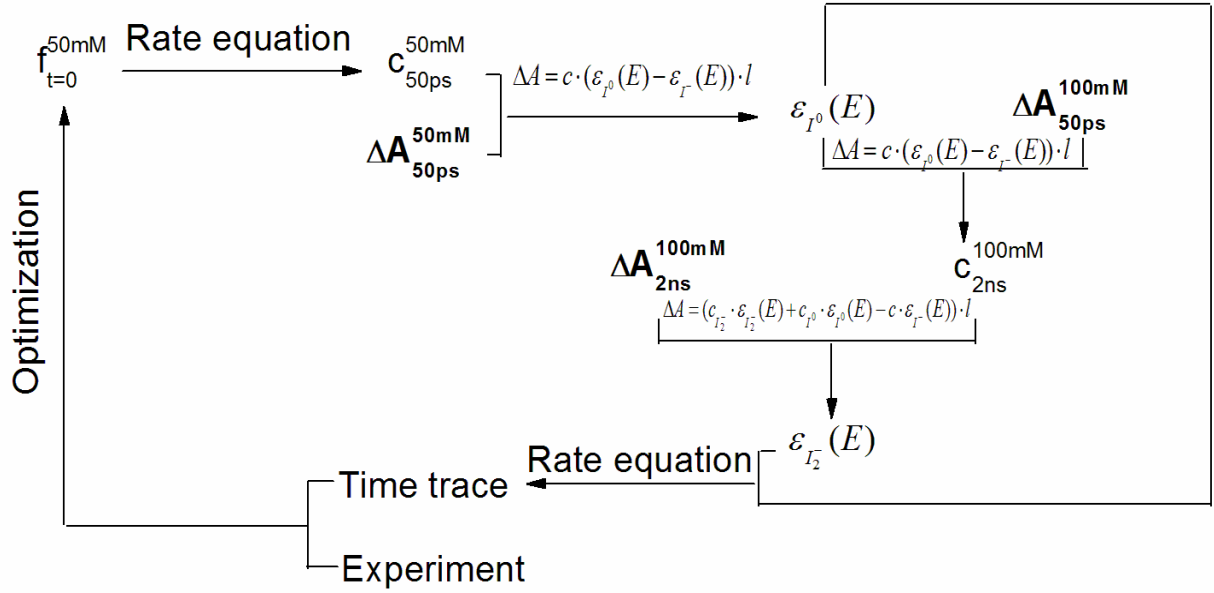


Fig. 6.7: Flowchart for fitting the time dependent of Fig. 6.2. In this procedure, transient absorption of 100 mM sample at 50 ps and 2 ns are involved.

The best fit signal is shown in Fig. 6.8, together with concentration kinetics of I^- , I_2 , I^0 and I_3 . In this approach, the main best fit parameter is excitation yield. It is reasonable that the decay profile of the time scan only depends on the initial excited concentration of iodide. With the rate equation established from the previous section, we should get a reliable f by fitting the time scan. Fig. 6.9 shows the correlation of the pair parameters f and t_0 at 3 levels of confidences 68.3%, 95.4% and 99.73%. The resulting best fit parameters are $f = 5 \pm 3\%$ and $t_0 = -11 \pm 1.54$ ps for confidence level of 99.73%. The excitation yield is comparable with the value of $\sim 4.5\%$ derived from the optical pump-probe measurement at a lower pump fluence of 1.2 J/cm^2 (Fig. 5.12). This confirms the reliability of the analysis. The uncertainty of t_0 is close to our experimental jitter time between laser and x-ray delay of 2 ps. In order to find a real range of f values, we investigate the dependence of average absorbance of the dip ranging from 5190-5193 eV in Fig. 6.4. It is obvious that the absorbance of I^0 must be positive or zero for the whole energy, so f values that lead to a negative absorbance in the dip range are unreasonable. This is a model independent method to determine lower boundary values of f . It was found that the lowest acceptable f is $\sim 5\%$ (Fig. 6.10), which is our best fit value. However, a rather high uncertainty of f values are found for a confidence level of 95.7%, the upper boundary of f in this case is 24% (Fig. 6.9), which generates the I^0 spectrum as shown in Fig. 6.4 (green curve).

Taking into account the two fitting approach (section 6.2.2 and 6.2.3), we conclude that f is within 5-24%.

From the resulting excitation yield $f=5\%$, we calculate the absorption spectra for neat I^0 and I_2 . The reconstructed spectra of transient species I^0 and I_2 are shown in Fig. 6.11, along with the static I^- and I_3^- spectra as reference. The pre-edge peak position of I_2^- , which is $2s \rightarrow \sigma_u$ transition is shifted by ~ 1.5 eV with respect to I^0 , indicating that the $I_2^- \sigma_u$ is located ~ 1.5 eV above the iodine $5p$ orbital. The peak intensity of the two spectra is comparable which is consistent with the simplified analogy that I_2^- is composed of an I^0 and an I^- , although the exact integral of the peak can be different because the orbital of I_2^- is different from that of I^0 . The edge jump of I_2^- is ~ 2 times larger than the I^0 or I^- due to the contribution of both I^0 and I^- . The edge position of I^0 is shifted by ~ 3 eV to higher energy with respect to the I^- edge. This is due to the higher electrostatic attraction for the outgoing electron to the I^0 .

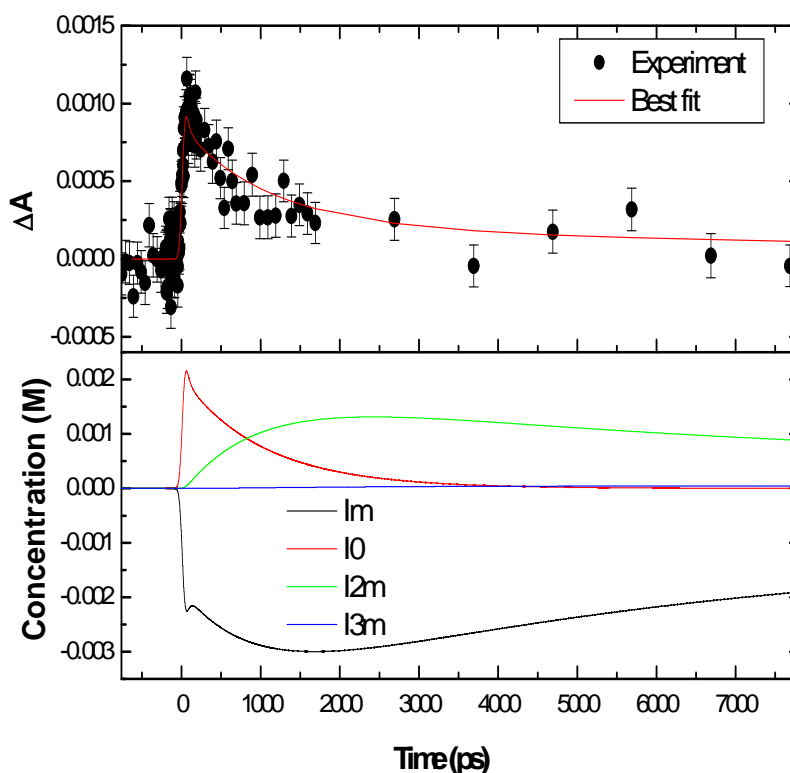


Fig. 6.8: Upper panel: temporal evolution of transient signal at 5184 eV of Fig. 6.1 and its best fit using kinetics model. Lower panel shows individual concentration of I^- (denoted as I^-), I^0 (I^0), I_2^- (I_2^-) and I_3^- (I_3^-) as a function of time.

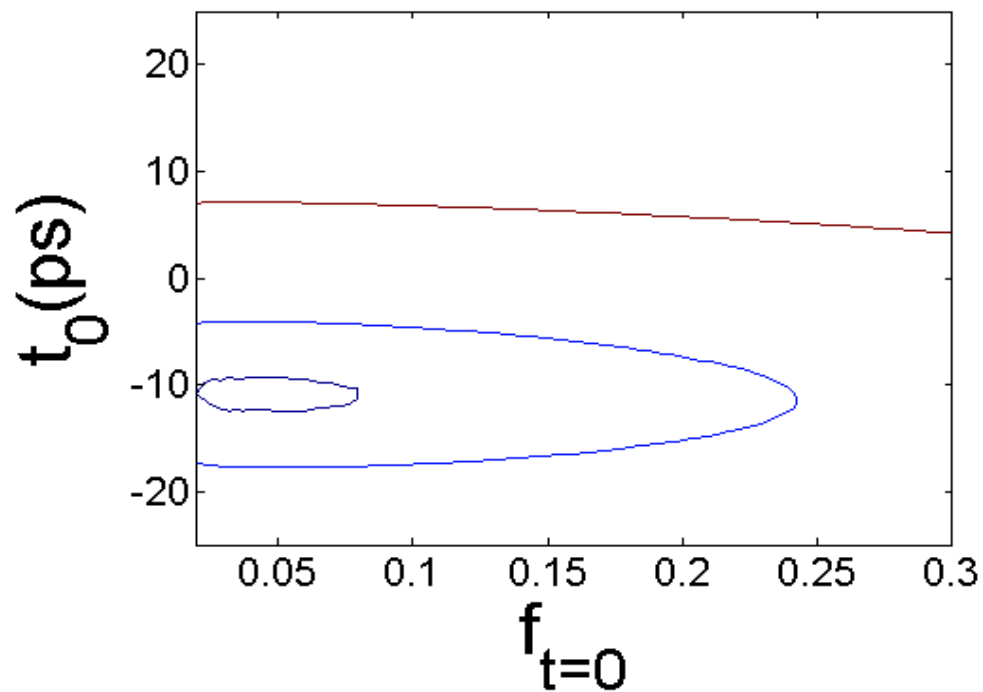


Fig. 6.9: Contour plot of f and t_0 correlation for three confidence levels of residuals 99.73% (purple), 95.4% (blue) and 68.3% (dark red).

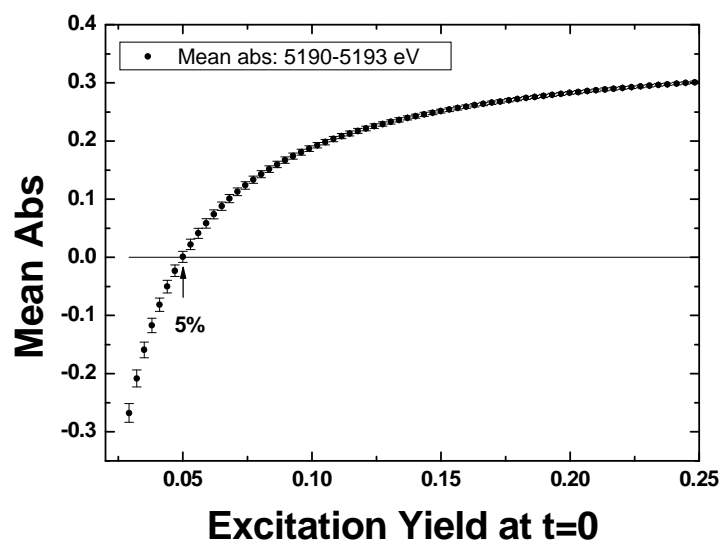


Fig. 6.10: Dependence of mean absorbance on initial excitation yield at dip feature of I^0 spectrum from 5190 to 5193 eV.

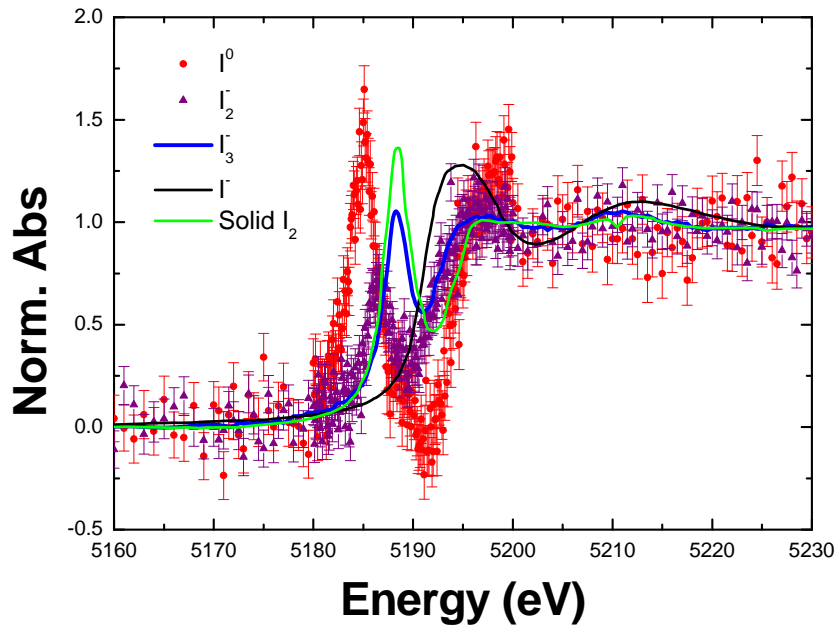


Fig. 6.11: Absorption for 1 M of I^0 , I_2^- , I^- , solid I_2 and I_3^- at a given sample thickness of 280 μm . The I^0 spectrum is generated with $f=5\%$. The I_3^- spectrum is derived from a static measurement of a solution containing $I_3^-+I^-$. The solid I_2 spectrum is also a static measurement whose edge jump is rescaled to that of I^- absorption.

The area of the resonant peak reflects the charge density of 5p orbital, by comparing intensity of this peak with neutral I_2 , Park et al. found electron transfer from $\text{Bi}_2\text{Sr}_2\text{CaCu}_2\text{O}_y$ lattice to an intercalated iodine in $I \text{ Bi}_2\text{Sr}_2\text{CaCu}_2\text{O}_y$ ¹²². Using this approach, we can determine the degree and direction of charge transfer in aqueous I^0 system. The spectra of I^0 is fitted with a Lorentzian and an Arctangen step function plus a Gaussian to model a multiple scattering (MS) feature right after the edge, where the Lorentzian is given by $f(E) = 2 \cdot L \cdot w / [\pi \cdot (4 \cdot (E - E_0)^2 + w^2)]$ with L corresponding to the area of the $2s \rightarrow 5p$ peak. The I_2 spectrum is fitted by the same function after rescaling the spectrum to the edge jump of I^0 . The ratio of best fit L values for I^0 and I_2 is $3.21(\pm 0.3)/2.73(\pm 0.17)$. A ratio of area ~ 1.18 indicates that there might be charge transfer from a nascent iodine atom to the surrounding water molecules. On the other hand, the upper boundary of f value ($f=24\%$) yields an area ratio for I^0 and I_2 of $0.85/2.73$ (≈ 0.31), indicating a reverse charge transfer from the surrounding

water molecules to the iodine atom. Table 6.2 summarizes the best fit parameters for I^- , I_2^- , I_3^- , I_2 and I^0 spectra using the above function. The resonant peak positions of poly-iodine molecules show a blue shift with respect to that of iodine atom which is the consequence of a transition from 2s to σ^* antibonding orbital located above the 5p level of iodine atom. The ionization potential (the edge position) increases with the decreasing average charge on one Iodine species, where the average charge located at the Iodine atom for I_2^- and I_3^- are $-1/2e$ and $-1/3e$, respectively. The blue shift of the edge with the decreasing average charge is a consequence of the stronger binding energy of the electron in more positively charged atoms.

Table 6.2. **Best fit parameters obtained from absorption spectra of iodine species.**

	I^-	I_2^-	I_3^-	I_2	I^0
Atomic peak(eV)	-	5186.5	5188.4	5188	5184.9
Ionization potential (eV)	5190.9	5191.7	5192.1	5193	5193.8
Area of atomic peak	-	2.59	6.4	3.05	3.21
Edge jump for 1M	0.45	0.97	1.39	0.46	0.45
Binding energy at 5p	5.5	5.2	3.7	5	8.9
Edge jump normalized	1	2	3	1	1

6.2.4 Kinetics of the photoproducts

Now that the absorption cross section of all species is known, the population of each species can be extracted from the transient absorption spectra (Fig. 6.1) via Eq. 6.2. The spectrum of each species is fitted with a superposition of a Lorentzian, arctan and a Gaussian function before passing to Eq. 6.2 for fit. The extracted concentration of I^0 , I , I_2 and I_3 at various time delays are shown in Fig. 6.12a (50 mM) and Fig. 6.12b (100 mM), together with the theoretical curves. As can be seen, the data is fairly consistent with the calculations from rate equations (solid curves). The data for the 100 mM sample is in better agreement with theory than that of the 50 mM sample. The discrepancy in the latter might arise from the uncertainty of the sample concentration due to the evaporation of the solvent by the pumping laser. The error bar of the extracted concentration in both samples are underestimated because the uncertainty of the molar extinction of the species were not included in their modeling functions.

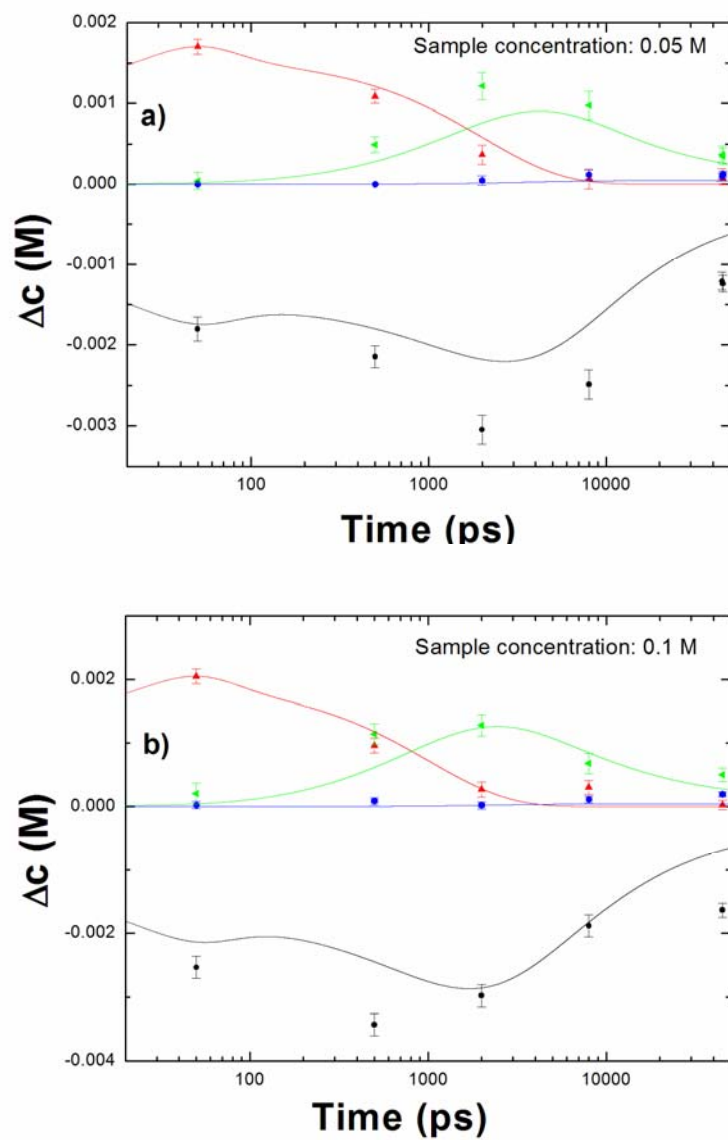


Fig. 6.12: Extracted concentration change of I^0 (red triangle), I_2 (green triangle), I_3 (blue hexagonal) and I^- (black circle) at various time delay. The solid curves show the calculations with the same color assignment.

6.3 Transient Structure of Aqueous Iodine Atoms

The reconstructed I^0 L_1 edge shows a shallower modulation above the edge compared to I^- L_1 edge (Fig. 6.11), implying structural changes. The signal to noise of the recovered I^0 spectrum is not good enough to carry a structural analysis. All structural analysis rely on the L_3 -edge data which is much more sensitive to the structure than the L_1 edge (as mentioned in section 4.1). Our transient absorption at the L_3 edge shows sufficient statistics to extract structural information (Fig. 6.13). Feature A on the rising edge of the static spectrum probably originate from multiple scatterings. Fig. 6.14 displays the reconstructed I^0 L_3 -edge spectrum for $f=3.2\%$ which is extracted from the transient L_1 edge for 100 mM sample (f for 100 mM sample is derived from the calculation for Fig. 6.12b). A blue shift of ~ 3 eV for the edge is observed, possibly reflecting both solvent shell structure and oxidation state changes of the iodine atom.

It is not realistic to do a structural analysis based on angle and bonds distance change of specific water molecules with respect to iodine due to the disordered property of the system. We implemented a proper technique similar the approach used in the EXAFS analysis for the static I^- presented in chapter 4. In this method, the radial distribution of aqueous iodine is derived from fitting the differential EXAFS signal, $\Delta\chi$. The $\Delta\chi$ is given by

$$\Delta\chi(k) = \chi_{I^0}(k) - \chi_{I^-}(k) \quad (6.4)$$

where $\chi_{I^0}(k)$ and $\chi_{I^-}(k)$ are the EXAFS spectra of I^0 and I^- , respectively. The $\Delta\chi(k)$ can be calculated directly from the transient absorption:

$$\Delta\chi(k) = \frac{\Delta A(k)}{c \cdot \Delta\mu} \quad (6.5)$$

where c is concentration of photogenerated iodine at the given time delay of the transient

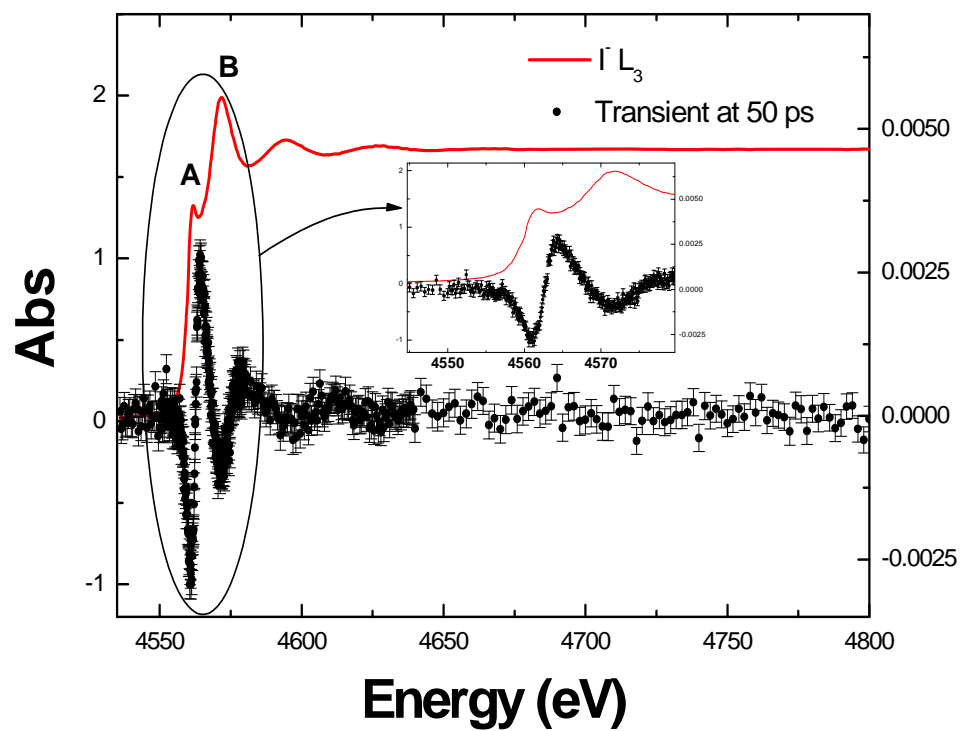


Fig. 6.13: Transient absorption at 50 ps for $I^- L_3$ in 100 mM sample (solid circle) and static I^- absorption (solid line).

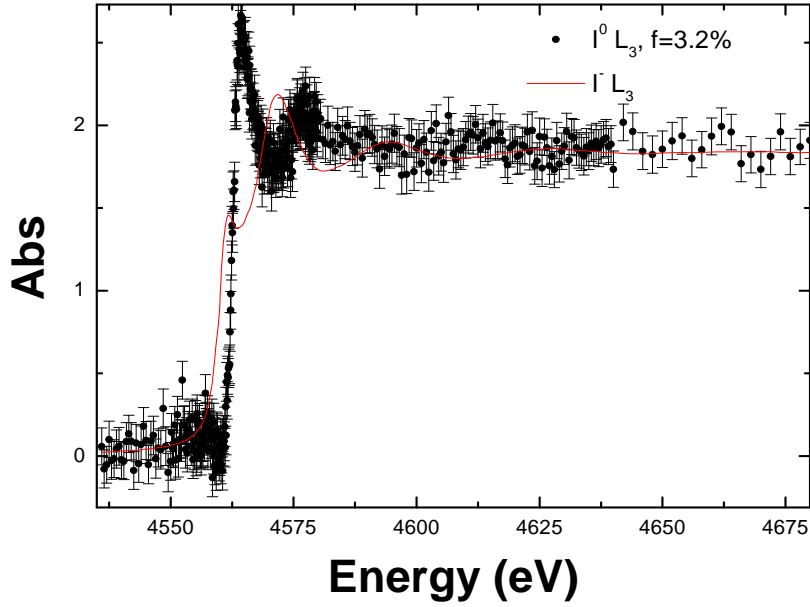


Fig. 6.14: Reconstructed $I^0 L_3$ edge for excitation yield $f=3.2\%$. The I^0 spectrum is recovered from the transient 50 ps in Fig. 6.13 of 100 mM sample.

spectrum, $\Delta A(k)$ is transient absorption spectrum in k -space, $\Delta\mu$ is the edge jump of the I static absorption. In fact, to enhance the structural sensitivity of the EXAFS spectrum, we do a k -weighing of $\Delta\chi(k)$. The $\chi_{I^0}(k)$ is calculated from an assumed $g(r)$ using the similar procedure presented in chapter 4. The $\chi_{I^-}(k)$ is the static experimental spectrum presented in Chapter 4. The shape of the I^0 -O RdF is optimized to fit the $\Delta\chi(k)$ using Eq. 6.4. The radial distribution function of I^0 -O is modeled by only one Γ -like function (Eq. 2.7). The EXAFS signal associated with hydrogen scattering is calculated from $g(r)$ of I-H derived from QM/MM simulation. The modeled $\chi_{I^0}(k)$ is shifted in energy space before being subtracted by static $\chi_{I^-}(k)$ to fit the experimental $\Delta\chi(k)$. The photogenerated iodine atom, c at 50 ps obtained from transient absorption at L_1 edge for 100 mM sample is 2.2 mM (corresponding to time zero $f=3.2\%$). In total, we have 4 parameters modeling $g(r)$ and an energy shift E_0 . The optimization is carried out in Matlab using GNXAS software for calculating EXAFS signal. The boundaries

for fitting the parameters are large enough so that the best fit values are well covered. Fig. 6.15 shows the $k\Delta\chi(k)$ and its best fit curve.

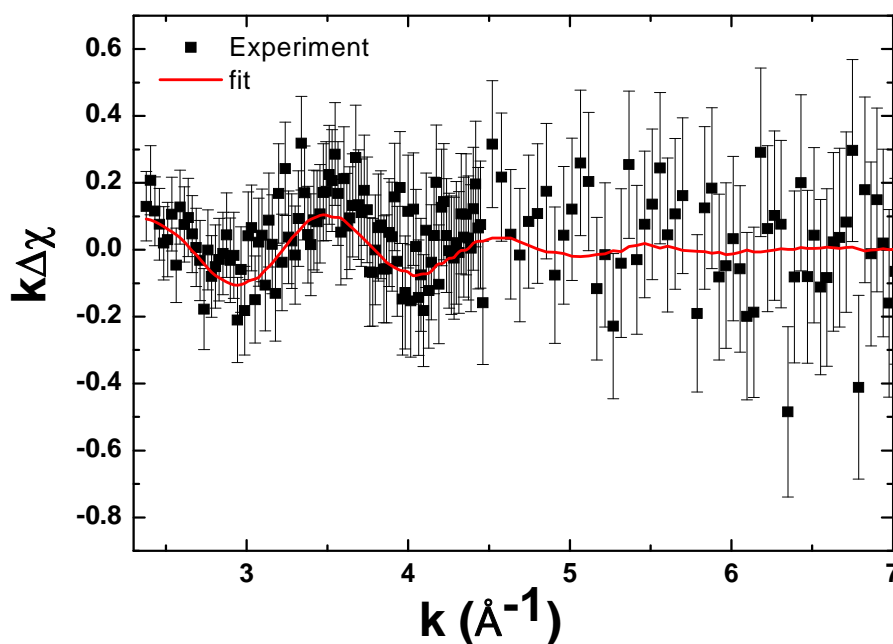


Fig. 6.15: k -weighted $\Delta\chi$ at the L_3 -edge of iodine (solid square) and its fit (solid curve). See text for details of the fit.

The reconstructed radial distribution function of I^0 is shown, along with the refined I^- $g(r)$ and the simulated $g(r)$ of I^0 -O²⁸ in Fig. 6.16. The first maximum of $g_{I^0-O}(r)$ is found to be 4.15 Å compared to 3.5 Å derived from I^- EXAFS refinement. The fact that the solvent shell of iodine is extended supports the hydrophobic property of the iodine atom in water, and this is predicted in our classical MD, QM/MM and DFT simulations, refer to the chapter 4. The iodine solvent shell is predicted to expand by 0.35 and 0.6 Å by the QM/MM and DFT simulation, specifically DFT simulation shows a small peak at 2.9 Å and a broad $g(r)$ with first maximum at ~ 4.1 Å. Koneshan et al.²⁸ found a $g_{I^0-O}(r)$ with first maximum at 4.25 Å (blue curve in Fig. 6.16), which is elongated by 0.65 Å compared to $g_{I^-O}(r)$. This elongation is in very good agreement with our value. The extracted $g_{I^0-O}(r)$ is significantly broader than that of $g_{I^-O}(r)$,

reflecting a more diffuse structure. The coordination number is important factor indicating the number of water molecules in the first solvation shell. A coordination number of oxygen for iodine hydration shell of ~ 20 is resulted from the fit (Fig. 6.15), which is larger than that of I^- with 7 (refer to chapter 4). The larger coordination number is a consequence of the larger and more disordered solvation shell. MD simulations show that the coordination number in iodine solvent shell is 27 which is not far from our value. Table 6.3 summarizes the best fit values with their boundaries. Note that R in this table is not the first maximum position but it is the position that divides the $g(r)$ into two parts with equal area.

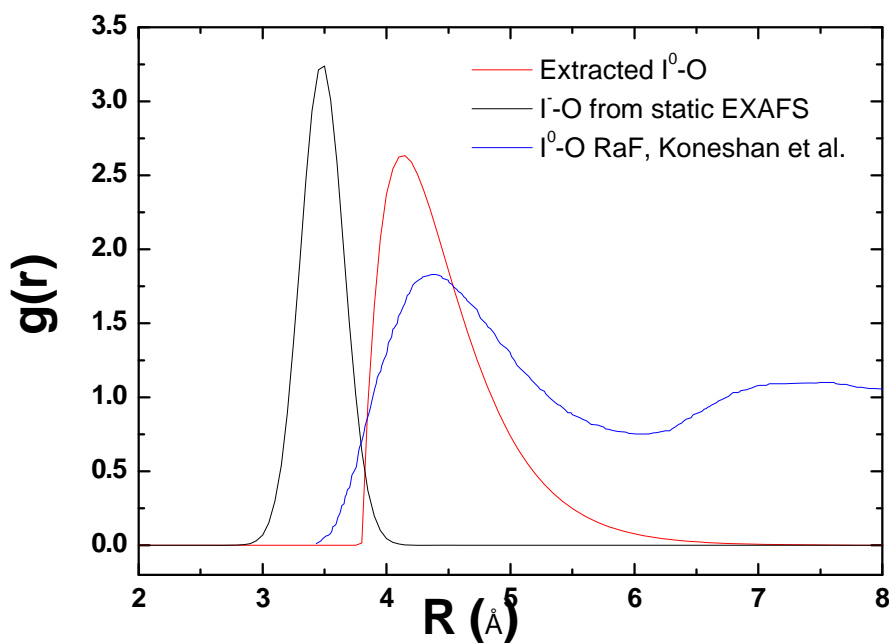


Fig. 6.16: Recovered iodine-oxygen radial distribution function is shown together with the refined I^- -O and the predicted I^0 -O²⁸ radial distribution function.

Table 6.3. Structural parameters of iodine solvent shell.

	Best fit value	Lower bound (99.7%)	Upper bound (99.7%)	Uncertainty (99.7%)
N	19.96	13.68	28.17	7.25
R(Å)	4.6	4.5	4.7	0.1
σ	0.32	0.27	0.43	0.08
β	1.42	1.22	1.65	0.22
E(eV)	3.32	2.35	6.06	1.86

The recovered EXAFS spectrum of I^0 is displayed in Fig. 6.17. The modulation amplitude of I^0 EXAFS is lower than that of I^- , which is consistent with the reconstructed L_1 edge spectrum.

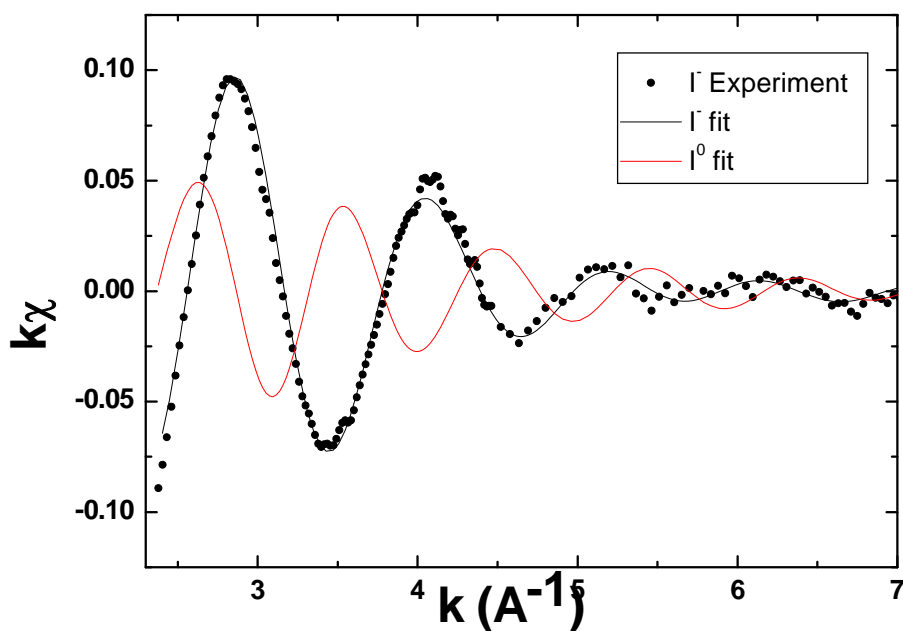


Fig. 6.17: Experimental EXAFS spectrum (solid circle) and fit (black solid line) of aqueous iodide together with the reconstructed EXAFS spectrum of iodine L_3 -edge (red curve) .

In the EXAFS analysis, the uncertainties of fit parameters are very important since they indicate the reliability of the extracted structure. The uncertainty in our analysis is performed based on a similar approach used in analyzing I⁻ EXAFS in chapter 4. Once the fit of $k\Delta\chi(k)$ has converged, we do a pair correlation test for a total 10 pair of parameters. The boundaries for best fit parameters are set for 99.7% confidence level. The contour plots for the 10 pair parameters correlation are shown in the Appendix. An uncertainty at 95% of confidence level found for R is 1.08 Å. So, an elongation of iodine solvent shell $\Delta R = 0.65 \pm 1.18$ Å is found. The uncertainty will obviously be smaller if the S/N of transient absorption is larger especially in the EXAFS region.

6.4 Conclusions

We have developed an independent way for obtaining excitation yield based on a rate equation model. The resulting excitation is consistent with the laser pump-probe data. The absorption cross section at L₁-edge of short-lived species I⁰, I₂ are revealed. The I⁰ absorption spectrum indicates that there might be charge transfer from the iodine atom to the caging water molecules. The atomic peak shift of ~1.5 eV in I₂ spectrum with respect to that of I⁰ is found, showing the energy difference between the σ_u orbital in I₂ and the 5p orbital in iodine atom. The edge positions obey the rule of the average charge residing on iodine ion. The extracted kinetics of iodine species is in agreement with calculations of kinetics reaction.

We demonstrated that structure of a disorder system can be determined by fitting the transient EXAFS. The analysis is based on the peak fitting of $g(r)$ applied for I⁻ EXAFS. The resulting $g_{I^0-O}(r)$ shows a significantly broader feature compared to $g_{I^-O}(r)$, reflecting a more disordered structure. It also indicates that the solvent shell of iodine atom is larger than that of I⁻ by $\Delta R = 0.65 \pm 1.18$ Å. This structure is responsible for the shallow modulation of the recovered I⁰ EXAFS.

The proposed time-resolved analysis approach is a promising method for analyzing disordered system such as aqueous halogen anion. The method will partly be applied for fs resolved data analysis.

Chapter 7 Femtosecond XANES study of aqueous iodide

7.1 Introduction

Now that we have learnt from I^0 L_1 -edge that at 50 ps there might be charge transfer between the iodine atom and the surrounding water molecule. In order to answer how and when this happens we need to know its dynamics at very early time. For tracking the solvation dynamics of I^- , one should probe the iodide anion itself and the neutral iodine atom by x-ray absorption, which would deliver both electronic and geometric structure during the solvation process. However, to access to early states of the process a sub-picosecond resolution is required. We employed femtosecond x-ray pulses generated by the laser slicing technique at the SLS (see section 3.5) to investigate the solvation dynamics of iodine following the photodetachment of iodide.

In the following section, we present our investigation on energy-resolved and time-resolved L_1 and L_3 edge spectra of iodine upon multiphoton excitation of 400 nm laser pulse. The energy resolution were ~ 2 eV.

7.2 Iodine XANES spectrum

Fig. 7.1a displays the L_1 edge transient absorption at 300 fs, the transient spectrum at 50 ps normalized to the maximum of the feature A of 300 fs spectrum is overlaid for reference. As can be seen, both spectra have a similar shape, except that the feature B in the spectrum at 300 fs is deeper than the 50 ps spectrum, the entire spectrum is also blue shifted by ~ 0.6 eV. The broadening of feature A (which corresponds to the $2s \rightarrow 5p$ transition) in the 300 fs spectrum is likely due to a poorer energy resolution (see section 3.7). The deeper amplitude and the blue shift of feature B indicate a stronger blue shift for the edge of I^0 spectrum at 300 fs compared to 50 ps. A shift to higher energy of the I^0 edge can be understood by the fact that at 300 fs the degree of the occupancy of $5p$ orbital is lower than that at 50 ps. Though it is not as clear as the L_1 spectrum, feature B of the L_3 spectrum shows a similar shift (Fig. 7.1b). The difference between the 50 ps and 300 fs transient spectra at L_3 edge implies different solvent shell structures between the two time delays.

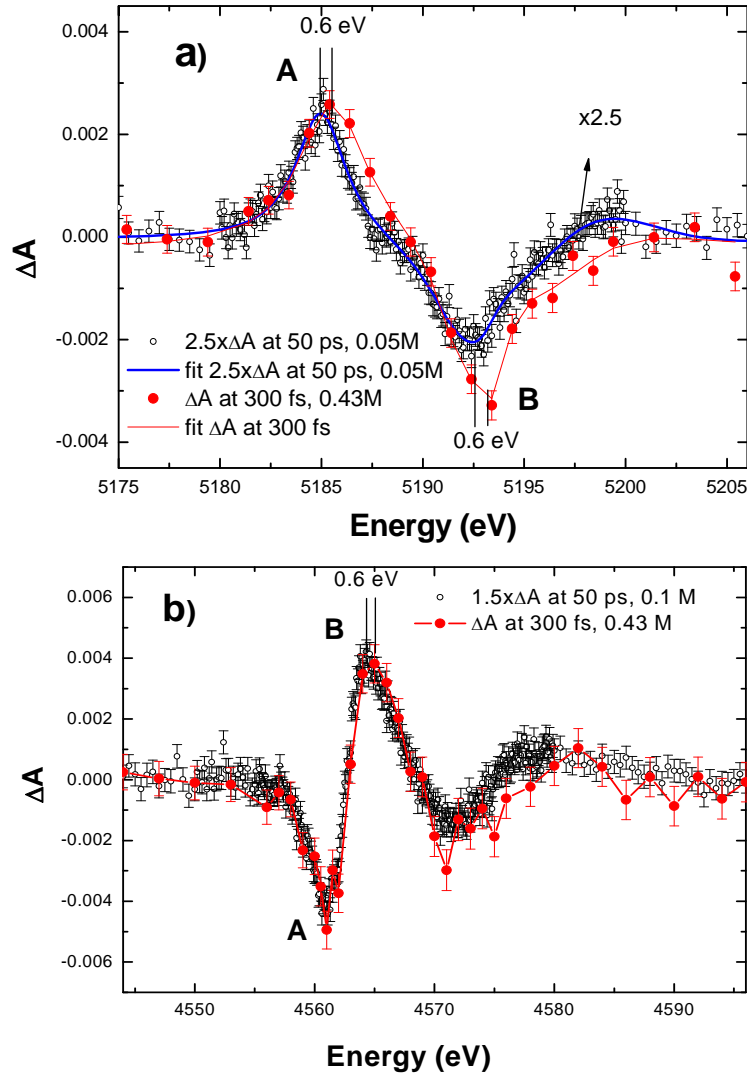


Fig. 7.1: Transient absorption at L_1 (a) and L_3 edge (b) for 430 mM sample, pumped by 0.8 J/cm^2 .

In order to examine the shape of I^0 spectrum we use the same approach applied for the I^0 spectrum at 50 ps presented in the section 6.2.2. Fig. 7.2 shows the dependence of the I^0 spectrum on the excitation yield. A similar trend to the I^0 spectrum at 50 ps is observed, a smaller f values results in a higher $2s \rightarrow 5p$ peak and the lower absorption at the feature between the peak and the edge of the spectrum (called dip).

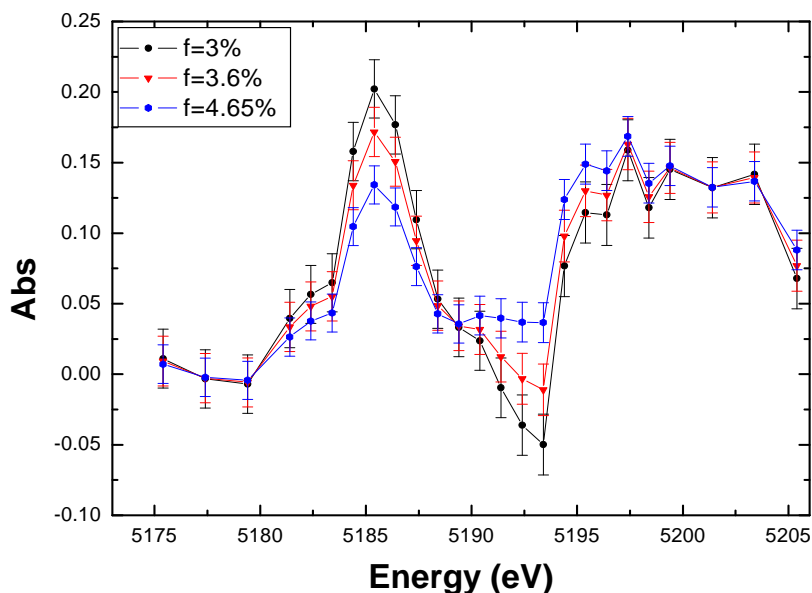


Fig. 7.2: The predicted shapes of IO XANES upon variety of excitation yields for 430 mM sample.

A lower limit for the excitation yield can be determined by plotting the dependence of the average absorbance of the dip versus the yield (Fig. 7.3b). It is found that the I^0 spectrum becomes reasonable for $f \geq 2.7\%$. The areas of the Lorentzian functions resulting from the fit of I^0 spectra are normalized with that of the spectrum of solid I_2 whose edge jump is rescaled to the edge jump of the reconstructed I^0 spectra. The area of the peak in the unit of solid I_2 peak (Fig. 7.3b) represents the occupancy of the $5p$ orbital¹²², thus hinting possible charge transfer directions (a ratio larger than unit implies a charge transfer from I^0 to solvent prior to the absorption of x-ray, a ratio smaller than unit implies the opposite). The figure is later used to determine the occupancy of the best recovered I^0 spectrum.

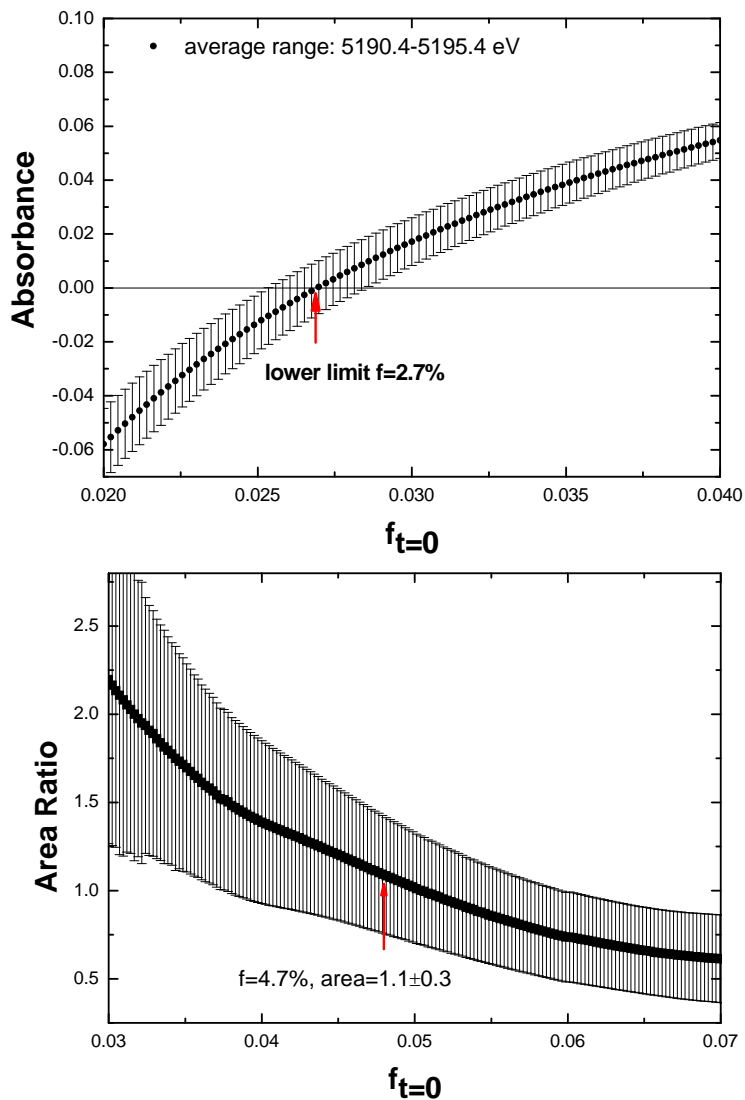


Fig. 7.3: The dependence of the averaged absorption of the dip (a) and the ratio of the 5p peak area (b) on the initial excitation yields. Sample concentration: 430 mM.

We performed a simple fit of the transient L_1 spectrum based on the procedure described in the section 6.2.2 to find the XANES of iodine. The best fit transient spectrum is presented as red curve in Fig. 7.1a. The best-fit excitation yield of 4.67% leads to a reconstructed I^0 spectrum presented in Fig. 7.4a for L_1 edge and Fig. 7.4b for L_3 edge.

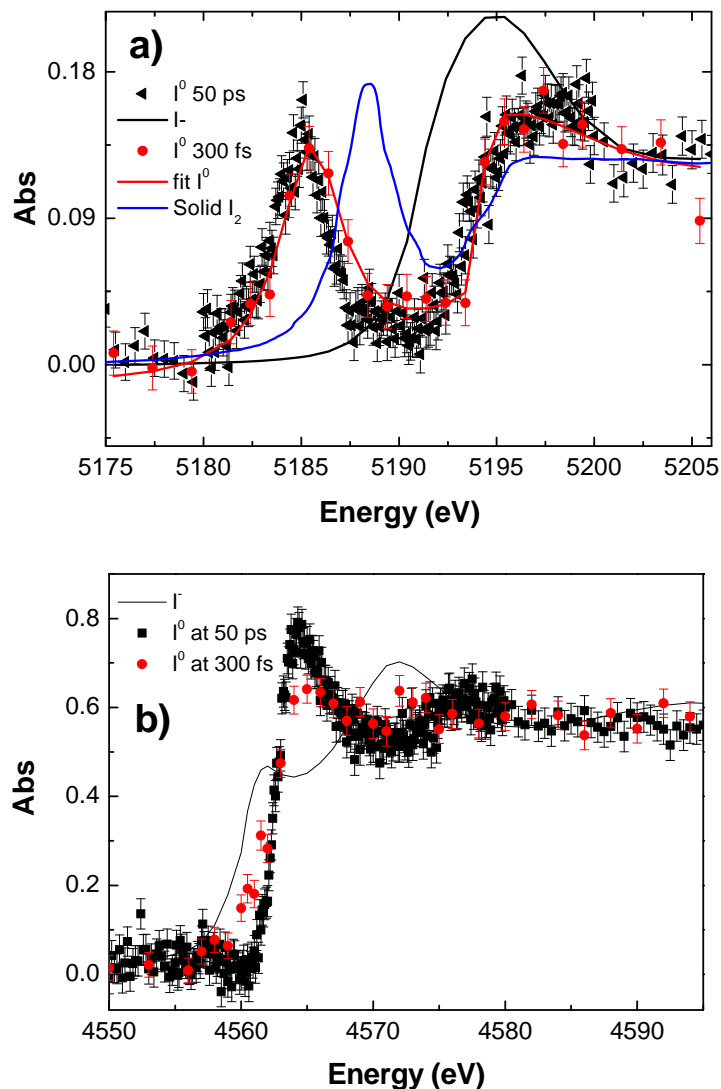


Fig. 7.4: The reconstructed I^0 XANES at L_1 (a) and L_3 edges (b).

Table 7.1 shows the best fit values for the transient L_1 edge. While the atomic peak of the I^0 spectrum at 300 fs is located 0.6 eV lower than that of the spectrum at 50 ps, its edge position is shifted by 1.2 eV with respect to the 50 ps. These imply that binding energy of the 5p electron decrease by 0.6 eV, whereas that of 2s electron decrease by 1.2 eV after 50 ps.

Table 7.1. I^0 XANES best fit parameters

	I^0 at 300 fs	I^0 at 50 ps
Atomic peak (eV)	5185.6	5184.97
Ionization potential (eV)	5194.4	5193.19
Area of atomic peak normalized to that of solid I_2	0.85/0.79 ^a	0.66/0.79 ^a
FWHM of atomic peak (eV)	3.6	3.15
Excitation yield (%)	4.7	7
Binding energy of 5p electron (eV)	8.8	8.2

^aarea of the lorentzian peak of I_2 after edge jump of the spectrum is normalized to that of the I^0 at 300 fs

The area of the $2s \rightarrow 5p$ peak is 1.1 ± 0.3 times larger than that of neutral I_2 , implying a possible charge transfer from the nascent iodine atom to water molecules occurred before the iodine atom is probed by x-ray. The peak area in the unit of I_2 atomic area is larger than the value found for I^0 XANES at 50 ps using the same analysis strategy. The decrease of the transition peak is consistent with the fact that a larger atomic peak (smaller occupancy) leads to a stronger binding of the inner electrons of iodine atom, thus resulting in a larger edge shift of the XANES at 300 fs compared to the XANES at 50 ps. It also suggests that this absorption cross section change is a result of a fast back charge transfer from the water molecules to iodine atom. The XANES L_3 edge at the early times exhibits a shallower modulation compared to that at the later time. This indicates a more diffused hydration structure of iodine atom at early time before it relaxes to a better defined structure over time. Unfortunately, a quantitative structural analysis based on the transient L_3 edge at 300 fs is not possible due to the poor quality of the spectrum.

7.3 Conclusions

The femtosecond x-ray transient data shows interesting features that could provide new insights in the electronic structure of the iodine atom. Using a simple fitting procedure for the transient absorption we extracted the XANES spectrum of iodine atom at 300 fs. The reconstructed L_1 edge spectrum shows that the binding energies of the $5p$ and $2s$ states increase

by ~ 0.6 eV and ~ 1.2 eV, respectively with respect to those at 50 ps. An increase in the $2s \rightarrow 5p$ transition probability is consistent with the increase of the ionization energy of iodine atom at 300 fs compared to 50 ps. The $2s \rightarrow 5p$ transition probability is found to decrease by ~ 1.1 times from 300 fs to 50 ps, suggesting a possible back charge transfer from water molecule to iodine atom. Further studies are underway to have a full picture of the electronic change and the reaction path way of iodine atom.

Chapter 8 Conclusions and Outlook

8.1 Conclusions

Ultrafast optical and x-ray spectroscopies were applied to study solvation dynamics in the case of an atomic solute in water, aqueous iodide, upon impulsive photoionization. We succeeded in observing the photogenerated iodine atom by x-ray absorption for the first time. Previous studies using ultrafast optical spectroscopy were capable of tracking the kinetics of electron¹⁶ and the transient states of iodide CTTS¹³ but did not deliver the rearrangement of water molecules upon photoexcitation of aqueous iodide. Using picoseconds and femtosecond x-ray pulse we are able to capture not only the solvent structure but also the electronic state of photogenerated iodine after the excitation by femtosecond laser pulse.

Though the initial purpose of our all-optical pump-probe measurements was to determine the fractional yield of excited species, for pump conditions identical to those of the laser pump/x-ray probe experiment, the multiphoton excitation reveals new insights into the solvation process. A strong temperature effect is observed in the kinetics of electron due to the red shift of the solvated electron absorption band after a blue shift of pre-thermalized electron. The increase temperature is due to the pump laser depositing heat in the solvent bath. The continuous red shift of electron absorption band changes the true electron dynamics, thus hiding the real solvation dynamics. Probing the iodide bleach in CTTS band is supposed to avoid the temperature effect on the electron, thus finding the iodine kinetics according to a stoichiometric reaction (Eq. 6.1). However, the CTTS band experiences a red shift with increasing temperature as well. The effect appears as the dependence of recovery time on pump fluences. Fortunately, the CTTS band has an isosbestic point, which is not affected by temperature. For the first time, we find the mere real kinetics of electron under multiphoton excitation using a rate model. The resulting $k_d^{-1} = 56.4 \pm 6.7$ ps, $k_n^{-1} = 97.9 \pm 7.2$ ps reflects a slower recombination than the dissociation of I:e contact pair as a result of broaden electron distribution which is in contrary with one-photon excitation¹⁶. Pumping the sample with one photon at 240 nm reproduces the previously reported electron kinetics¹⁵. The electron kinetics is well modeled with by the mean force potential (MFP) theory and the rate equation using the concept of iodine-electron contact pair.

Structural analysis of the iodide static solvent shell shows that quantum mechanics/molecular mechanics (QM/MM) simulation provides the better description of the shell than classical molecular dynamics (CMD) and density functional theory (DFT) simulation. This is a consequence of a better description of water-water interaction in the QM/MM simulation.

The analysis of time-resolved XAS data demonstrates new methods for estimate excitation yields of a photodetachment process, which is vital information to reconstruct absorption spectra of photoproducts, without *a priori* knowledge on the excitation conditions. Time-resolved XAS yields the XANES spectra of short-lived photoproducts from 300 fs to several nanoseconds. These absorption cross-sections are used to reproduce the population kinetics of photoproducts.

The solvent structure of hydrated iodine after 50 ps is discovered for a first time using a new analyzing approach based on $g(r)$ refinement. The finding shows that the solvation shell of iodine is expanded by ~ 0.6 Å, compared to that of I^- . Its structure is also more diffuse, thus less rigid, than I^- .

Femtosecond XANES study found that binding energy of 5p and 2s electron decrease by ~ 0.6 eV and 1.2 eV, respectively when the time increases from 300 fs to 50 ps. Simultaneously, the strength of the $2s \rightarrow 5p$ transition decreases by ~ 1.1 times. This hints a possible absorption cross section change due to charge transfer from water to iodine atom.

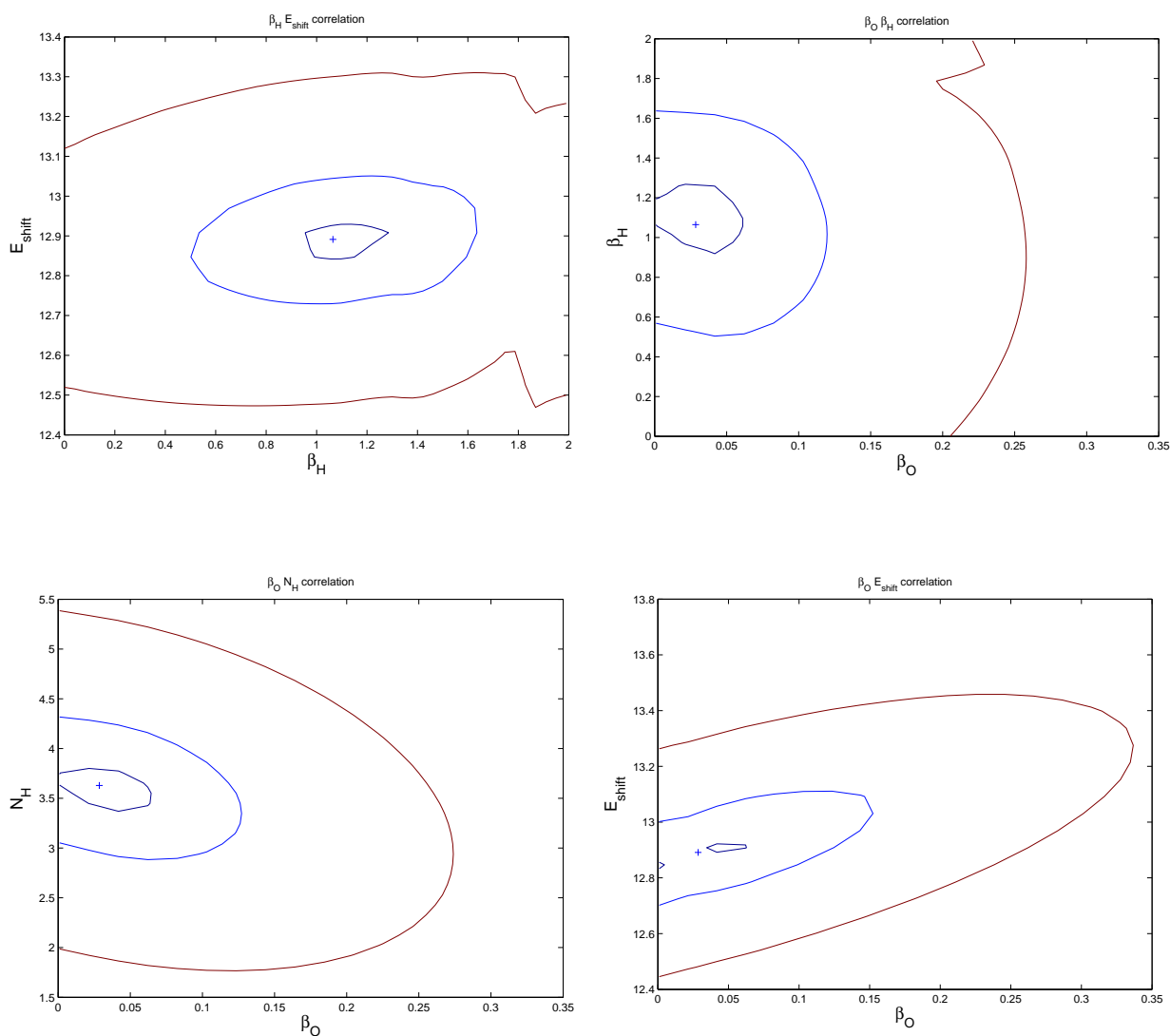
8.2 Outlooks

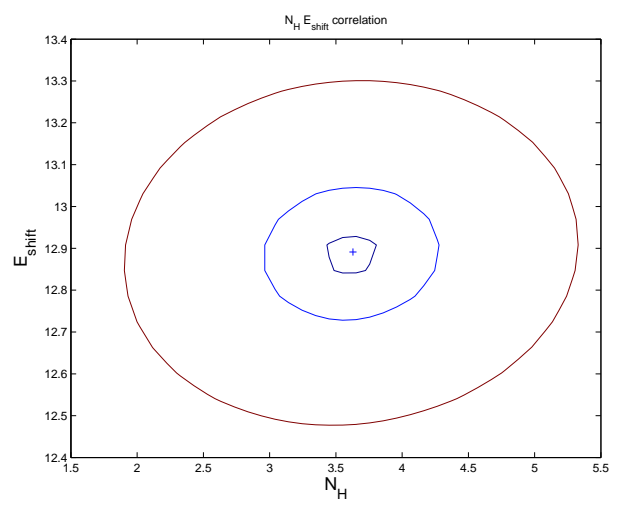
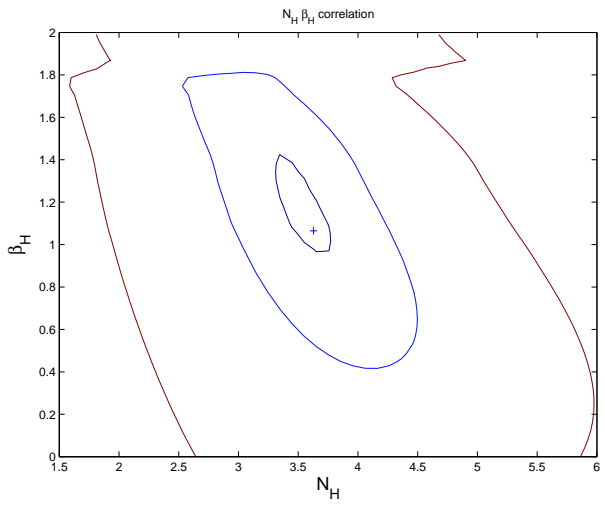
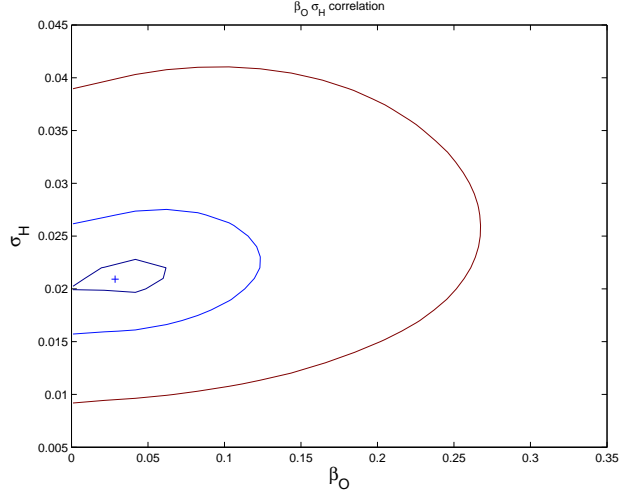
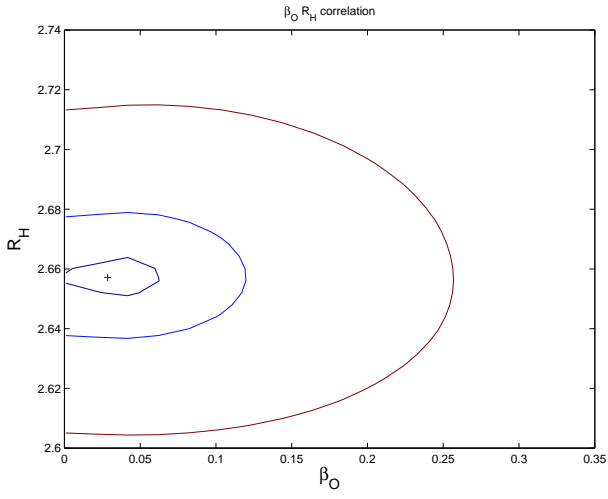
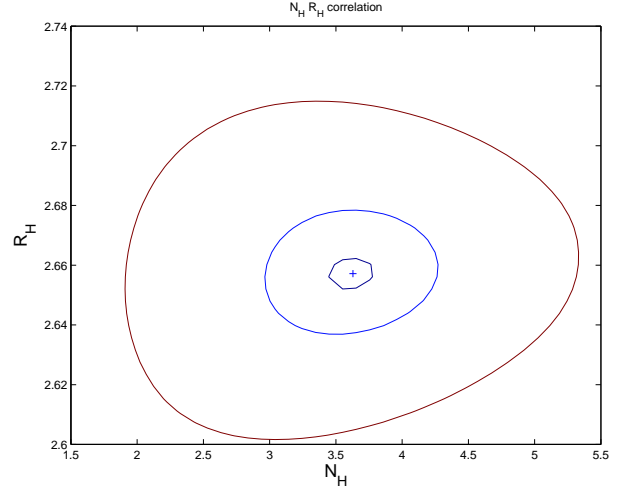
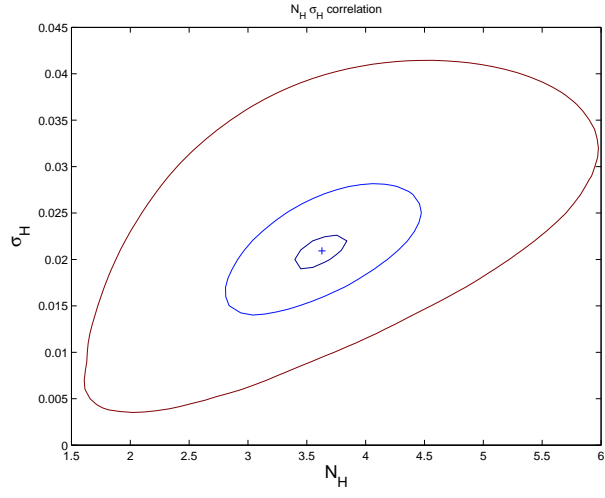
Although the solvation shell of iodine has been found, its uncertainty is rather large. This originates from the small signal-to-noise transient EXAFS data, as well as in the nature of the solvent shell itself: the hydrophobic iodine radical leads to a larger cage size, which in return is filled with much more cage water molecules, which are less attached to the radical, thus leading to this rather diffuse cage. However, we can nevertheless imagine that this can be better determined with better statistics, thus at advanced new free x-ray electron laser sources.

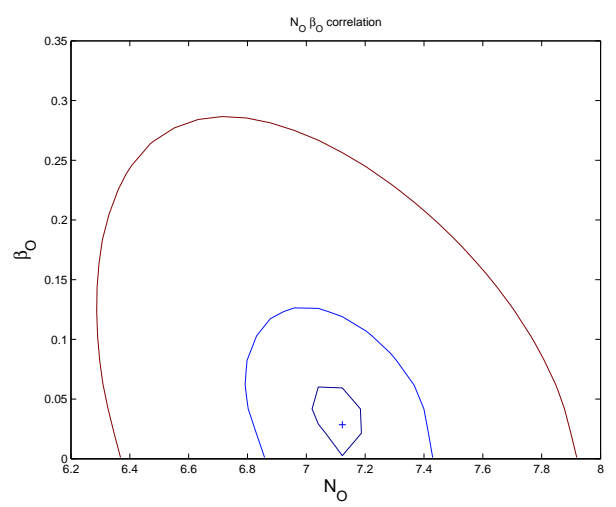
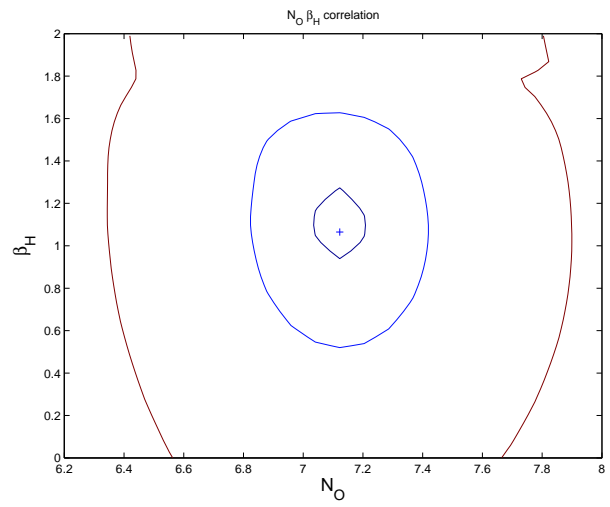
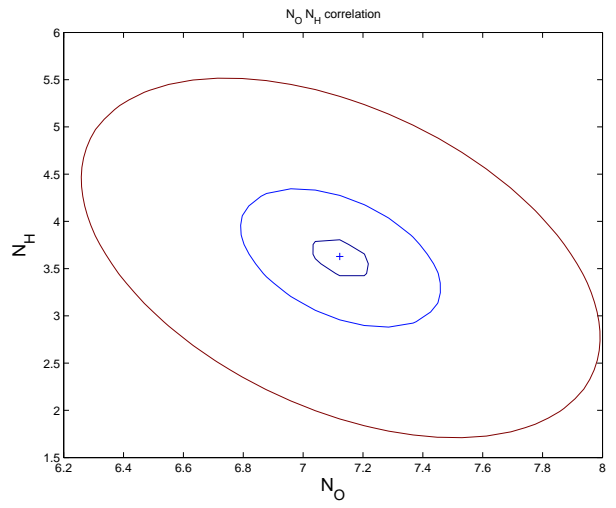
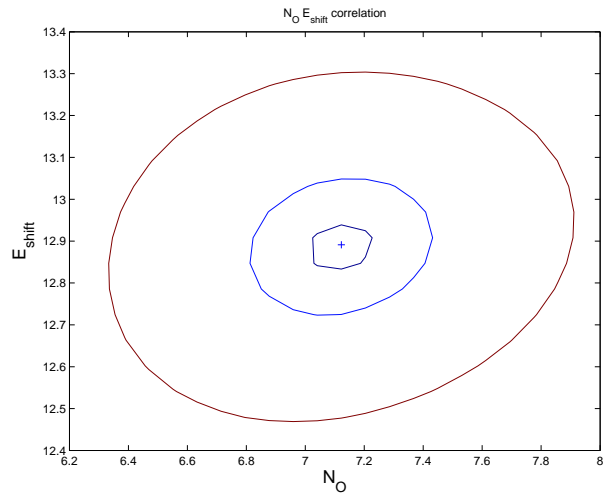
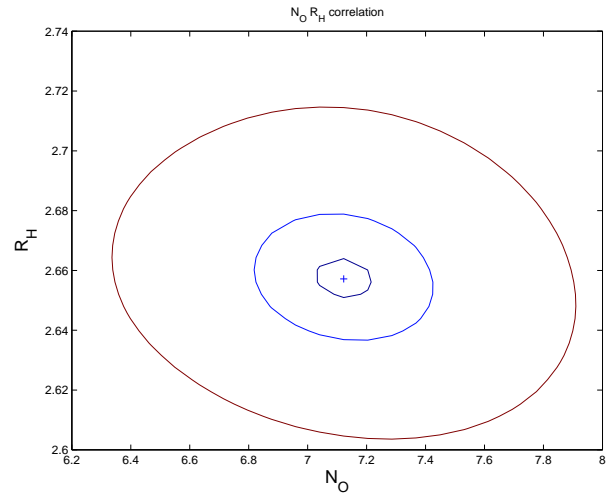
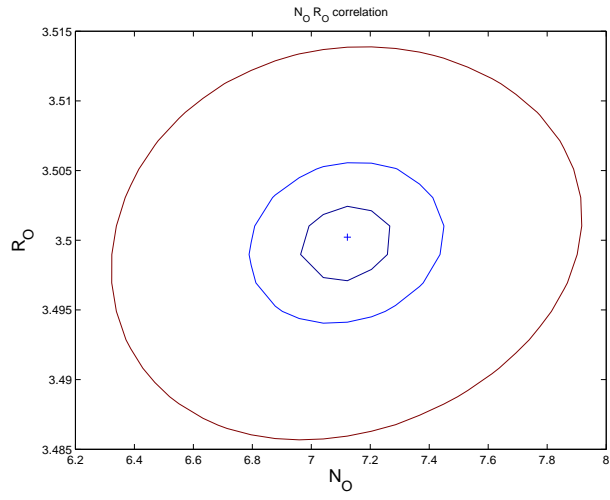
The interesting femtosecond XANES data needs to be further analyzed. The data could provide totally new insights in the solvation dynamics of iodide under multiphoton excitation. Further studies of this data are undergoing.

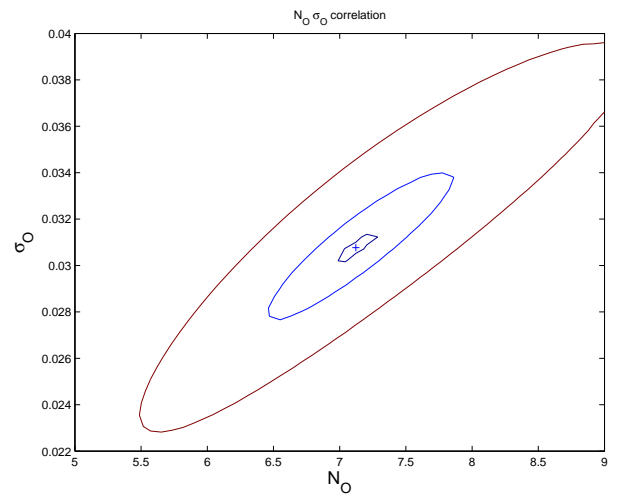
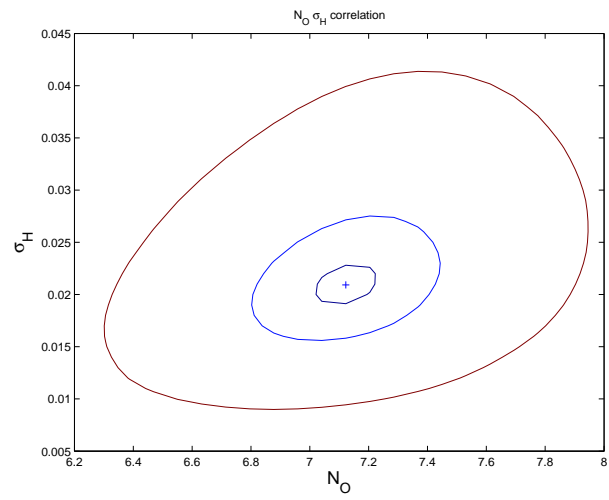
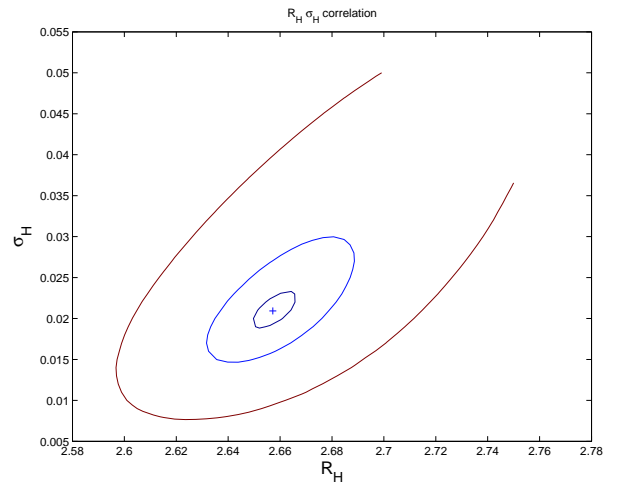
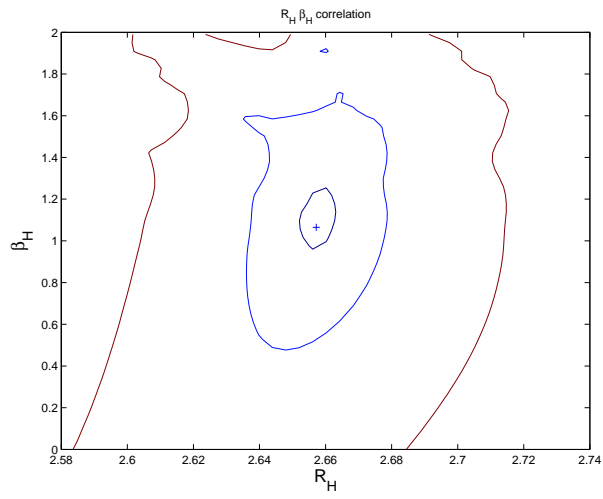
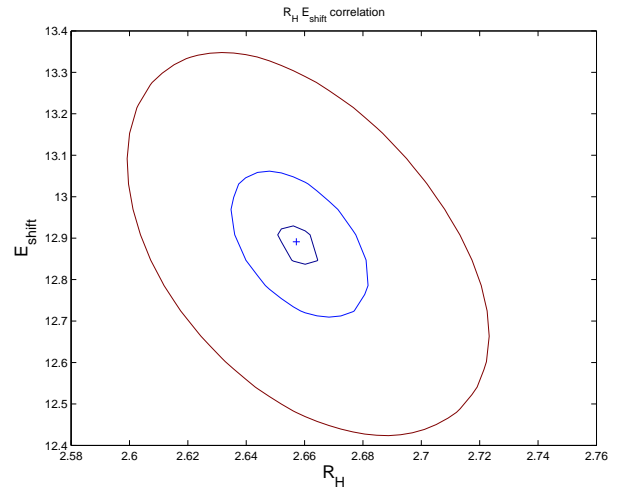
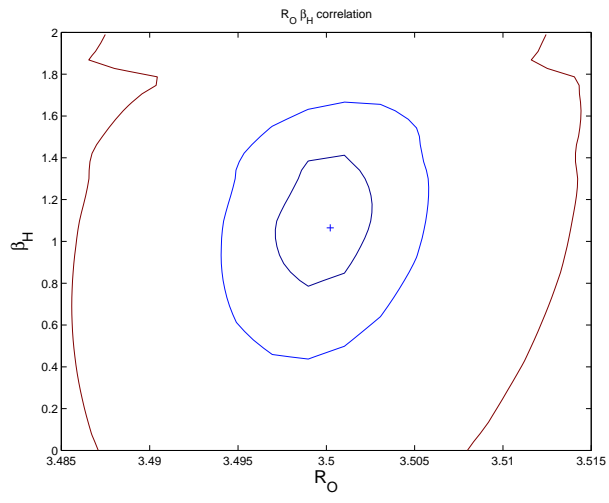
Appendix A Determination for uncertainties of the parameters of iodide static solvation shell

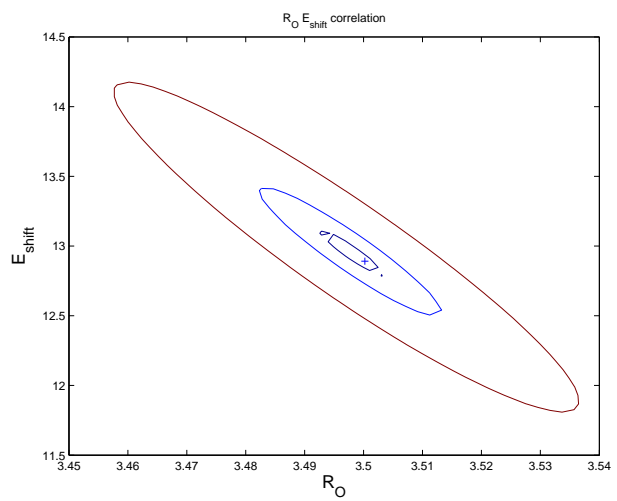
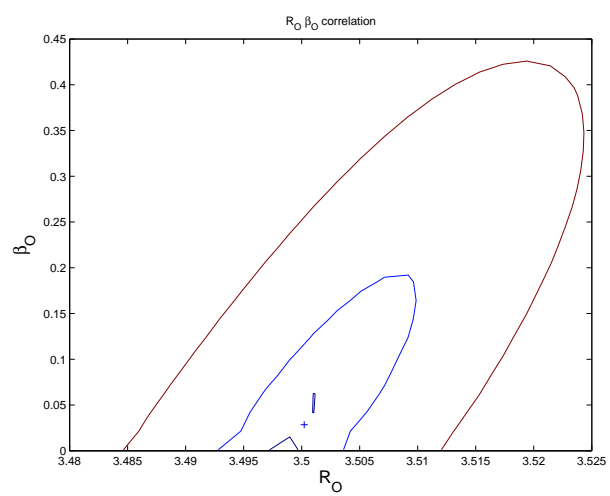
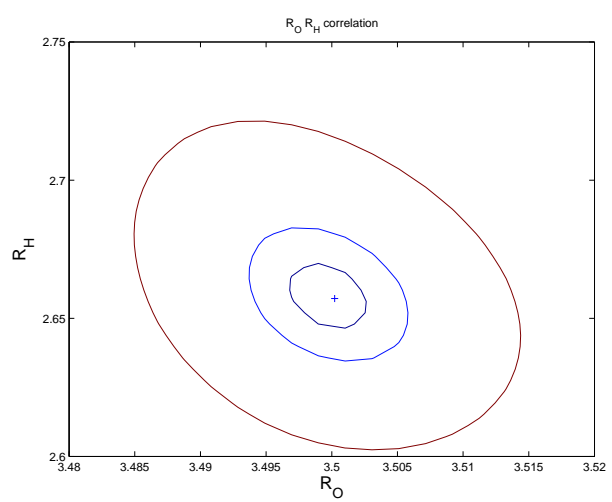
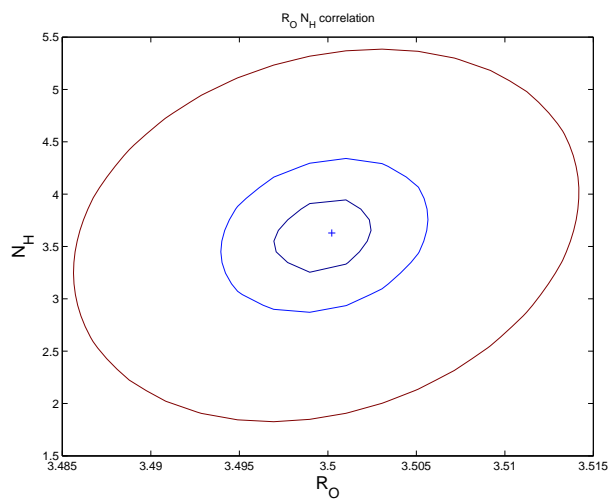
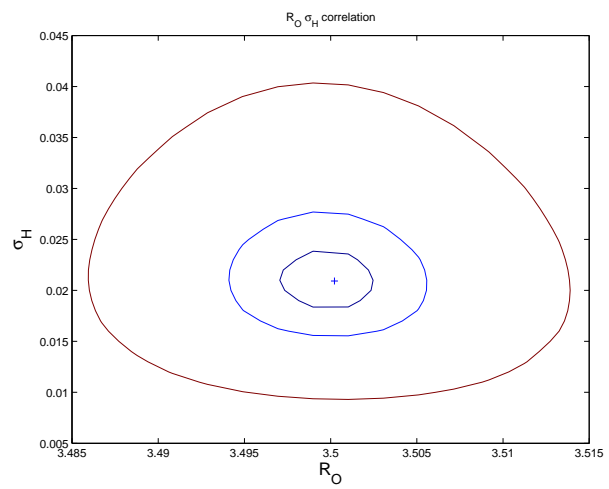
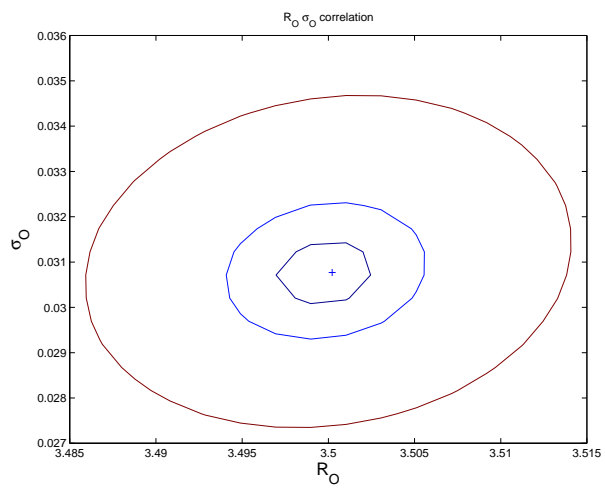
Parameters that define iodide solvation shell are: N_X , R_X , σ_X , β_X , E ($X=O$: oxygen, H : hydrogen) which are coordination number, averaged distance from the anion, dimensional less skewness and energy shift, respectively.











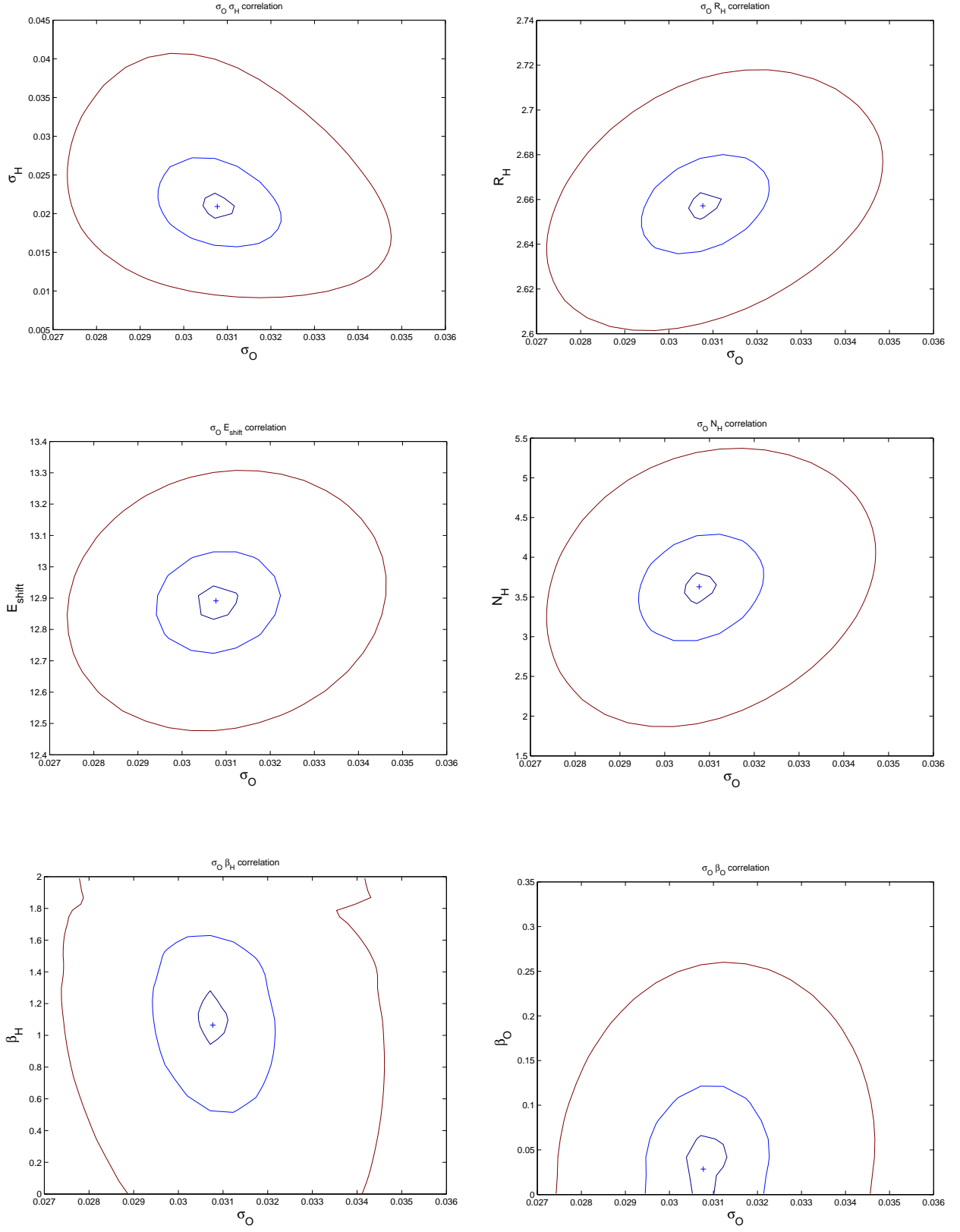
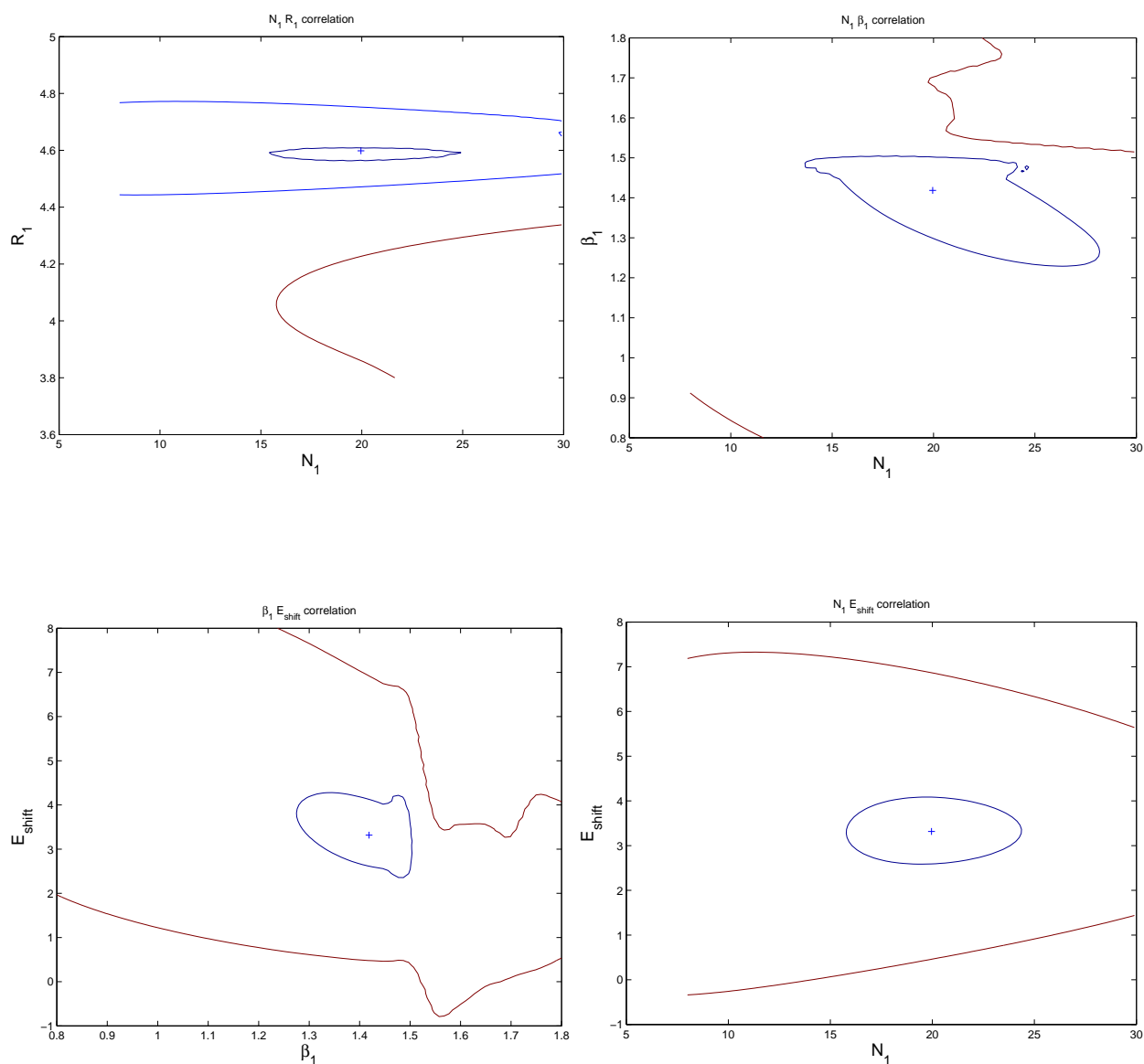


Fig. A.1: Correlation maps for all possible combination of the pair parameters. The three circles correspond to three confidence levels 68.3% (dark red), 95.4% (blue), and 99.73% (purple). The uncertainties presented in section 4.3 are yielded from 95.4% of confidence level. The blue cross shows the best fit values.

Appendix B Determination for uncertainties of iodine solvation shell at 50 ps

Only first solvation shell of $g_{I-O}(r)$ is fitted. Parameters that define the shell are: N_O , R_O , σ_O , β_O , E which are coordination number of oxygen, averaged distance from the anion to oxygen, dimensional less skewness and energy shift, respectively.



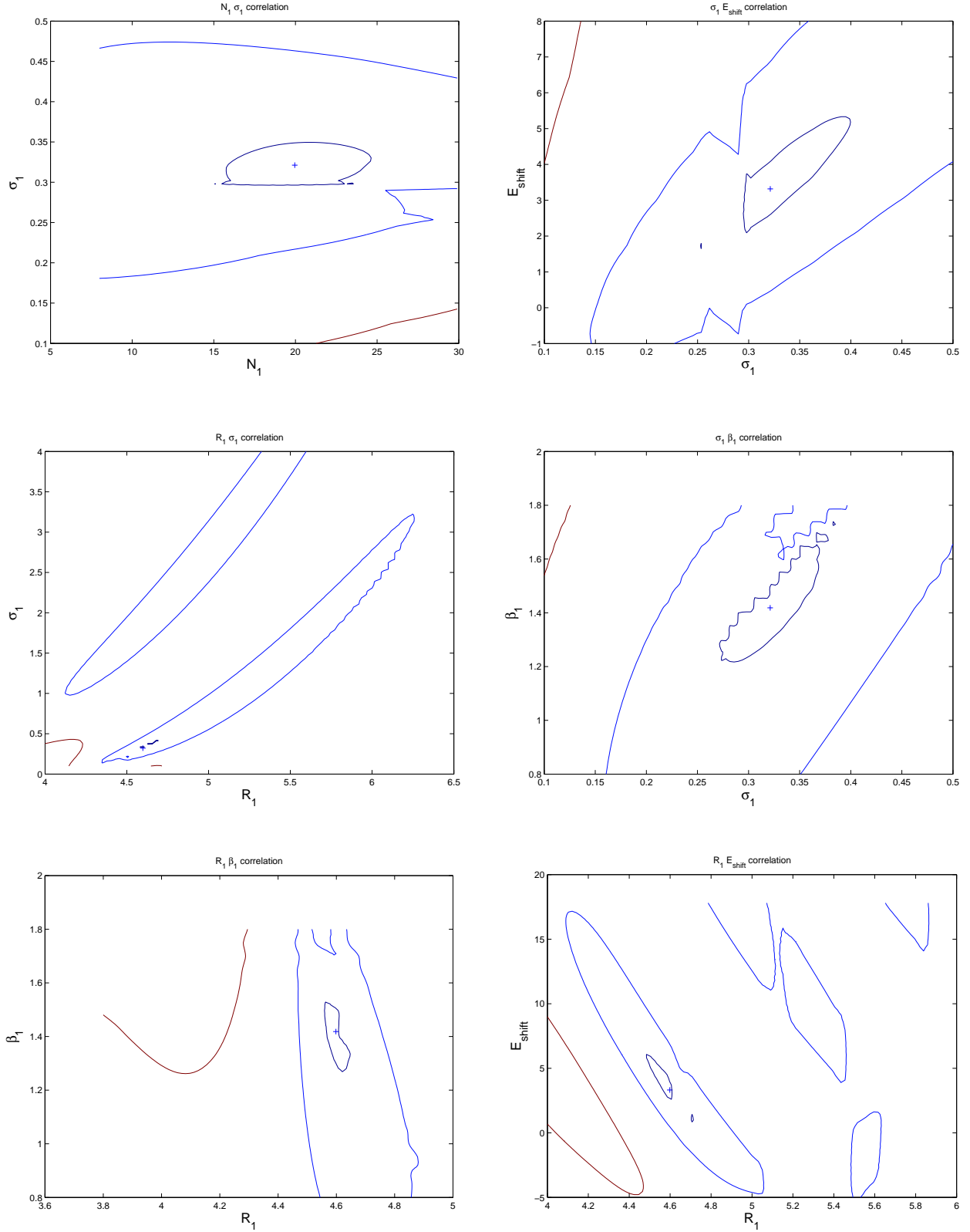


Fig. B.1: : Correlation maps for all possible combination of pair parameters. The three circles correspond to three confidence levels 68.3% (dark red), 95.4% (blue), and 99.73% (purple). Because the uncertainties corresponding to 68.3 and 95.4% are out of calculating range, most of the uncertainties given in section 6.3 are those at 99.7% confidence level except for that of R which is at 95.4% of confidence level. The blue cross displays the best fit values.

Acknowledgements

I would like to acknowledge people who have helped and shared the difficulties and happiness with me during the past 4 years and 8 months of my PhD study.

The first person I would like to express my great gratitude to is my supervisor, Prof. Majed Chergui. Majed has brought me to Switzerland and given me the chance to learn from world leading scientists and approach advanced knowledge. His guidance and encourage have created great motivations in my study. I am thankful for his warm and generous mind not only to me but also to the entire group.

The second person who has made great impacts in my works is my co-supervisor, Prof. Christian Bressler. My research would not be running well without Christian's supervision. Looking back to the beginning of my doctoral study, I deeply appreciate how enormously patient Christian was in teaching me. I would not have such patience to teach a student with almost zero knowledge in x-ray science like me that time. My knowledge in ultrafast science has been enriched thanks to the discussions with Christian. I have learnt a lot from Christian with his German style in science where the accuracy and logicalness is paramount.

I would like to acknowledge all members of the doctoral committee for assessing my work. I am grateful to Prof. Paola D'Angelo and Prof. Alfred Laubereau for traveling abroad despite of their busy working schedules. I am also thankful to Prof. Lothar Helm and Prof. Gérard Gremaud for their acceptance to be members of the jury and their interests in my work.

The X-ray group involves many members residing in Lausanne and Villigen. I am glad that I had time to work and interact with them. I am thankful to Dr. Wojciech Gawelda, the former Ph.D student in our group who has guided me since I started. Working with Wojciech is a real pleasure, he turned hard moments of beamtimes to easy and fun times thanks to his special ability of uniting people, which is vital for any success. I would like to thank Dr. Chris Milne for leading many beamtimes that I was involved. I am thankful to Chris for being a good friend and a mirror of a professional scientist. I am grateful to Renske for her enthusiastic help, as well as for being one of the most active members in all beamtimes. I would like to thank Amal

and Fred for their help and our discussions. The former and present post-docs in the group Dr. Maik Kaiser, Dr. Yuri Zaushitsyn, Dr. Helge Brands, Dr. Dimali Vithanage have been very helpful and I would like to thank all of them. I am grateful to my successor: Marco Reinhard with whom I have the pleasure to work and share my experiences.

I would like to acknowledge scientists responsible for the micro-XAS beamline: Dr. Daniel Grolimund, Dr. Camelia Borca, Dr. Rafael Abela and the technician: Mr. Beat Meyer, Mr. Markus Willmann. Our collaborators FEMTO team has been of great help to us. I am thankful to Dr. Gerhard Ingold, Dr. Paul Beaud and special thank to Dr. Steve Johnson. Steve is one of the most knowledgeable people in experimental x-ray science I have ever worked with. I appreciate his guidance during 4 months when I worked in Villigen.

I would like to thank all colleagues in Lausanne that I have chance to interact with: Dr. Frank van Mourik, Dr. Andrea Cannizzo, Dr. Andreas Tortschanoff, Dr. Gerald Auböck, Ajdarzadeh Oskouei Ahmad, Olivier Braem, Cristina Consani, Ahmad Odeh, Dr. Fabrizio Carbone, Hannelore Rittmann-Frank Mercedes. I acknowledge Dr. Ivano Tavernelli for his help in simulations. Thanks to Mr. Michel Kessou for his computer support, Mrs. Ariane Cordonier, Mrs. Monique Grin Celka, Mrs. von arx Esther for paper work, Monsieur Moser and Monsieur Ritter for their mechanical and electronic equipments.

I would like to thank friends and family who have supported me: con cảm ơn bố mẹ và em Bình đã luôn quan tâm động viên con, mặc dù bố đã không thể nhìn thấy con khi con học xong nhưng hình ảnh bố sẽ luôn ở bên con. Xin cảm ơn tất cả các anh chị em trong cộng đồng sinh viên Việt Nam ở Lausanne, vnlausanne, vì những động viên và chia sẻ trong cuộc sống.

Curriculum Vitae

Name: Van-Thai PHAM
Nationality: Vietnamese
Date of birth: October 27th, 1979
Place of birth: Hanoi, Vietnam
Address: Room CH H1 555
Laboratory of Ultrafast Spectroscopy,
Swiss Federal Institute of Technology Lausanne,
CH-1015 Lausanne
Switzerland
Tel. +41 21 693 0368
Email: vanthai.pham@epfl.ch

QUALIFICATION PROFILE

Five years research in time-resolved x-ray and laser absorption spectroscopies, Ultrafast Laser Techniques, Synchrotron Radiation Instrumentation, Instrument Control, Data Acquisition and Analysis, X-ray Spectroscopy (EXAFS, XANES), Programming Language Matlab, Python, Various X-ray Data Analysis Softwares (e.g., FEFF, MXAN, GNXAS), Molecular Graphic Viewer (VMD), Usual Text and Graphing Programs, Physical Chemistry, Condensed Phase Dynamics, Light-induced Spin Crossover ...

EDUCATION

03/2010 (expected) Ph.D in Physical Chemistry “Picosecond X-ray absorption studies of solvation dynamics” supervised by Prof. Dr. Ch. Bressler and Prof. Dr. M. Chergui
Swiss Federal Institute of Technology Lausanne, Switzerland

08/2003 Master of Science in Optical Spectroscopy “Photovoltaic and photorefractive effects in Pr: LiNbO₃” supervised by Prof. Dr. Ki-Soo Lim
Chungbuk National University, South Korea

07/2001 Bachelor of Science (Physics),
Hanoi University of Science, Vietnam

TEACHING EXPERIENCE

- 2006-2007 Tutorials and assistant to “Atomes et Rayonnement” for 3rd year students in physics, lectured by Prof. Dr. Christian Bressler, Swiss Federal Institute of Technology (EPFL), Lausanne, Switzerland.
- 2003-2004 Teaching assistant to laboratory course in optics for students in physics department of Chungbuk National University, South Korea.

PREVIOUS POSITIONS

- 3/2005 – present Research Assistant, Laboratoire de Spectroscopie Ultrarapide, Dept. of Chemistry, EPF Lausanne, Switzerland
- 9/2001 – 3/2005 Research Assistant, Dept. of Physics, Chungbuk National University, South Korea
- 7/2001 – 09/2001 Research Assistant, Center for Quantum Electronics, Vietnam Institute of Physics, Vietnam National Center for Natural Science and Technology, Vietnam
- 9/1997-7/2001 Undergraduate student, Dept. of Physics, Hanoi University of Science, Vietnam

RESEARCH VISITS AND GRADUATE SCHOOLS

- 06/2008 “Ultrafast X-ray Summer School”, Stanford Linear Accelerator (SLAC), Menlo Park, USA.
- 06/2008 Visit/talk at the Advanced Light Source, Lawrence Berkeley Lab., Berkeley, USA
- 04/2007 Advanced analysis of transient XAS data via MXAN (1 week), Collaboration with Laboratori Nazionali di Frascati Rome, Italy.
- 06/2005 “International School of Atomic and Molecular Spectroscopy”, Poster: “Transient Local Structure of Solvated Transition Metal Complexes Probed by Picosecond Time-Resolved XAFS”. Erice, Italy.

11/2005-03/2006 Five months as research assistant at the FEMTO group, PSI Villigen, Switzerland, in a collaboration for picosecond x-ray absorption and diffraction studies in solids, and preparations for fs-sliced experiments.

PRIZES AND AWARDS

2001 Scholarship for Master student in Chungbuk National University, South Korea.

2004 KOSEF scholarship for excellent PhD student in Chungbuk National University, South Korea.

2006 Best Poster Prize, Swiss Light Source User's Meeting 2006: "Picosecond XAFS of Photoionized Aqueous Halides"

2006 Best Poster Prize, Swiss Chemical Society Annual Meeting, University of Zurich, Zurich, Switzerland, 2006 (shared with Dr. Wojciech Gawelda): "Light-Induced Spin Crossover Probed via Picosecond XAFS"

PROFESSIONAL MEMBERSHIPS

Korean Physical Society, Swiss Physical Society, Swiss Chemical Society.

PUBLICATIONS

- 1. The solvent shell structure of aqueous iodide: X-ray absorption spectroscopy and classical, semi-classical and quantum molecular dynamics**
V.-T. Pham, I. Tavernelli, C. Milne, R. van der Veen, P. D'Angelo, Ch. Bressler and M. Chergui
Submitted
- 2. Time-resolved x-ray absorption spectroscopy: Watching atoms dance**
Chris J. Milne, Van-Thai Pham, Wojciech Gawelda, Renske M. van der Veen, Amal El Nahhas, Steven L. Johnson, Paul Beaud, Gerhard Ingold, Frederico Lima, Dimali A. Vithanage, Maurizio Benfatto, Daniel Grolimund, Camelia Borca, Maik Kaiser, Andreas Hauser, Rafael Abela, Christian Bressler, and Majed Chergui
Journal of Physics: Conference Series, 190, 012052 (2009)
- 3. Retrieving photochemically active structures by time-resolved EXAFS spectroscopy**
Renske M. van der Veen, Christian Bressler, Chris J. Milne, Van-Thai Pham, Amal El Nahhas, Frederico A. Lima, Wojciech Gawelda, Camelia N. Borca, Rafael Abela and Majed Chergui
Journal of Physics: Conference Series, 190, 012054 (2009)
- 4. Structural Analysis of ultrafast EXAFS with sub-picometer spatial resolution : application to solvated spin cross-over complexes**
W. Gawelda, V.-T. Pham, R. Van der Veen, D. Grolimund, R. Abela, M. Chergui, C. Bressler
Journal of Chemical Physics, 130, 124530 (2009)
- 5. Structural Determination of a Photochemically Active Diplatinum Molecule by Time-Resolved EXAFS Spectroscopy**
Renske M. van der Veen, Chris J. Milne, Amal El Nahhas, Frederico A. Lima, Van-Thai Pham, Jonathan Best, Julia A. Weinstein, Camelia N. Borca, Rafael Abela, Christian Bressler, and Majed Chergui
Angewandte Chemie International Edition, 48, 2711 (2009)
- 6. Femtosecond XANES study of structural dynamics in solutions: the light-induced spin cross-over in an Iron(II)-complex**
Ch. Bressler, C. Milne, V.-T. Pham, A. ElNahhas, R. van der Veen, W. Gawelda, S. Johnson, P. Beaud, D. Grolimund, C. Borca, G. Ingold, R. Abela, M. Chergui
Science, 323, 489 (2009)
- 7. Driving Atoms With Light**
G. Ingold, S. Johnson, P. Beaud, F. Krasniqi, E. Vorobeve, R. Abela, C. Borca, D. Grolimund, Research C. Milne, V.-Thai Pham, A. El Nahhas, R. van der Veen, W. Gawelda, C. Bressler, M. Chergui
Paul Scherrer Institut (PSI) Scientific Report 2007, (in press, 2008)
- 8. EXAFS Structural Determination of the $\text{Pt}_2(\text{P}_2\text{O}_5\text{H}_2)_4^{4-}$ Anion in Solution**

- van der Veen, Renske M.; Milne, Christopher J.; Pham, Van-Thai; El Nahhas, Amal; Weinstein, Julia A.; Best, Jonathan; Borca, Camelia N.; Bressler, Christian; Chergui, Majed
Chimia, 62, 287-290 (2008)
9. **Structural determination of a short-lived Iron(II) Complex by Picosecond X-ray Absorption Spectroscopy**
W. Gawelda, V.-T. Pham, M. Benfatto, Y. Zaushytsin, M. Kaiser, D. Grolimund, S. Johnson, R. Abela, A. Hauser, Ch. Bressler and M. Chergui
Physical Review Letters, 98, 057401 (2007)
 10. **Observation of the solvent shell reorganisation around electronically excited atomic solutes by picosecond X-ray absorption spectroscopy**
Van-Thai Pham, Wojciech Gawelda, Yuri Zaushitsyn, Maik Kaiser, Daniel Grolimund, Steven L. Johnson, Rafael Abela, Christian Bressler and Majed Chergui
J. Am. Chem. Soc. 129, 1530-1531 (2007)
 11. **Capturing Transient Electronic and Molecular Structures in Liquids by Picosecond X-Ray Absorption Spectroscopy**
W. Gawelda, V.T. Pham, A. El Nahhas, M. Kaiser, Y. Zaushitsyn, S.L. Johnson, D. Grolimund, R. Abela, A. Hauser, Ch. Bressler and M. Chergui
AIP Conference Proceedings, 882, 31 (2007)
 12. **Ultrafast X-ray spectroscopy for structural dynamics studies in chemistry and biology**
Gawelda, W., Pham, V.T., El Nahhas, A., Johnson, S.L., Grolimund, D., Kaiser, M., Abela, R., Chergui, M., Bressler, C.
Proceedings of SPIE - The International Society for Optical Engineering, 6727, 67271P (2007)
 13. **Ultrafast Nonadiabatic Dynamics of $[\text{FeII}(\text{bpy})_3]^{2+}$ in Solution**
Wojciech Gawelda, Andrea Cannizzo, Van-Thai Pham, Frank van Mourik, Christian Bressler, and Majed Chergui
J. Am. Chem. Soc. 129, 8199 -8206 (2007)
 14. **Light-induced spin crossover probed by ultrafast optical and X-ray spectroscopies**
Gawelda, W., Cannizzo, A., Pham, V.-T., El Nahhas, A., Milne, C.J., Van Der Veen, R., Bressler, C., Chergui, M.
Chimia, 61, 179-183 (2007)
 15. **Ultrafast X-Ray Absorption Spectroscopy at the swiss Light Source**
W. Gawelda, S. Johnson, D. Grolimund, R. Abela, M. Kaiser, W. Gawelda, V. T. Pham, Y. Zaushitsyn, B. Verbrugge, M. Chergui, C. Bressler, M. Cascella, I. Tavernelli, A. Hauser
Paul Scherrer Institut (PSI) Scientific Report 2005, Vol. 1, 12 (2006)
 16. **Light-induced absorption and holographic recording in Pr:LiNbO_3**
Pham, V.-T., Lee, S.-K., Trinh, M.-T., Lim, K.-S., Hamilton, D.S.
J. Korean Phys. Soc. 49, 533-537 (2006)
 17. **Nonvolatile two-color holographic recording in Tm-doped near-stoichiometric LiNbO_3**

- Pham, V.-T., Lee, S.-K., Trinh, M.-T., Lim, K.-S., Hamilton, D.S., Polgár, K. Opt. Comm. 248, 89-96 (2005)
- 18. Change of optical band gap and magnetization with Mn concentration in Mn-doped AlN films**
Song, Y.-Y., Quang, P.H., Pham, V.-T., Lee, K.W., Yu, S.-C.
J. M. M. M. Volume 290-291 PART 2, 1375-1378 (2005)
- 19. Optical spectroscopy of thulium-doped oxyfluoroborate glass**
Lim, K.-S., Babu, P., Jayasankar, C.K., Lee, S.-K., Pham, V.-T., Seo, H.-J.
J. Alloys Compd. 385, 12-18 (2004)
- 20. Large magnetic entropy change in a $\text{La}_{0.8}\text{Ca}_{0.2}\text{MnO}_3$ single crystal**
Phan, M.H., Pham, V.T., Yu, S.C., Rhee, J.R., Hur, N.H.
J. M. M. M. Volume 272-276, Issue III, 2337-2339 (2004)
- 21. Characteristics of two-color holographic recording in lithium niobate doped with thulium**
Ki-Soo Lim, Van-Thai Pham, Sun-Kyun Lee, Minh-Tuan Trinh, Douglas Hamilton, Katalin Polgar
Proceedings of SPIE- Volume 5560, Photorefractive Fiber and Crystal Devices: Materials, Optical Properties, and Applications IX, Francis T. S. Yu, Ruyan Guo, Shizhuo Yin, 1-8 (2004)
- 22. Photorefractive and Spectroscopic Properties of $\text{Pr}:\text{LiNbO}_3$**
Lim, K.-S., Pham, V.-T., Lee, S.-K., Trinh, M.-T., Hesselink, L., Neurgaonkar, R.R.
Proceedings of SPIE - The International Society for Optical Engineering, 5206, 45-54 (2003)
- 23. Infrared to visible up-conversion in thulium and holmium doped lutetium aluminum garnet**
Lim, K.-S., Babu, P., Lee, S.-K., Pham, V.-T., Hamilton, D.S.
J. Lumin. 102-103, 737-743 (2003)
- 24. Photoluminescence of terbium ions in near-stoichiometric lithium niobate**
Lee, M., Lim, K.-S., Lee, S.-K., Pham, V.-T., Kitamura, K., Takekawa, S.
J. Lumin. 102-103, 644-650 (2003)

CONFERENCE PRESENTATIONS

1. Talk: "Solvation Dynamics Studies using femtosecond X-ray", Annual Ski Meeting, Ovornnaz, Switzerland, March 2009
2. Poster: "Nascent iodine radicals studied by ultrafast laser and X-ray absorption spectroscopies", Swiss Physical Society, University of Geneva, 2008.
3. Poster: "Observation of Photogenerated Nascent Aqueous Iodine Radicals via X-Ray Absorption Spectroscopy", Swiss Chemical Society Fall Meeting, EPFL, 2007
4. Poster: "Solvation Dynamics Studies on Photoexcited Aqueous Iodide using Time-resolved X-ray Absorption Spectroscopy" Femtochemistry 8, Oxford, England, 2007
5. Poster: "Observation of Photogenerated Nascent Aqueous Iodine Radicals via X-Ray Absorption Spectroscopy" Swiss Physical Society Annual Conference, University of Zurich, 2007
6. Talk : "Time-resolved XAS and Optical Experiments on Iodide in Water", Colloquium of the Laboratoire de Spectroscopie Ultrarapide, EPFL, 2007
7. Poster: "Light-Induced Spin Crossover Probed via Picosecond XAFS", Swiss Chemical Society Annual Meeting, University of Zurich, Zurich, Switzerland, 2006
8. Poster: "Light-Induced Spin Crossover Probed via Picosecond XAFS", Swiss Light Source User's Meeting 2006
9. Poster: "Picosecond XAFS of Photoionized Aqueous Halides", Swiss Light Source User's Meeting 2006
10. Poster: "Direct Observation of I^0 Atoms in Aqueous I^- using Ultrafast Time-resolved Absorption Spectroscopy", Swiss Physical Society Annual Meeting, EPFL, Lausanne, Switzerland, 2005
11. Poster: "Ultrafast Structural Dynamics Research at the Swiss Light Source", Swiss Light Source User's Meeting 2005
12. Talk & Poster: "Photoionization Dynamics of Aqueous I^- using Ultrafast Optical Pump-Probe and X-ray Absorption Spectroscopies" Swiss Chemical Society Annual Meeting, EPFL, Lausanne, Switzerland, 2005
13. Poster: "Transient Local Structure of Solvated Transition Metal Complexes Probed by Picosecond Time-Resolved XAFS", International School of Atomic and Molecular Spectroscopy, Erice-Sicily, Italy, June 2005.
14. Poster: "Two-color holographic recording in Tm-doped $LiNbO_3$ ", Proceedings of the Optical Society of Korea Annual Meeting 2004, February 12-13, 2004, Chonnam University, Korea.
15. Poster: "Photorefractive properties of $Pr:LiNbO_3$ in open and short circuits", Korean Physical Society Meeting, April 25 2003, Yonsei University, Korea.
16. Talk: "Thulium doped near-stoichiometric $LiNbO_3$ material for holographic data

- storage”, Korean Physical Society Meeting, October 24-25 2003, Kyungbuk University, Korea.
17. Poster: “Three-dimensional bit memory in photopolymers by two-photon absorption”, The Photonics Conference 2003 November 12-14, 2003, Jeju, Korea
 18. Poster: “Photorefractive effect and two-color holographic recording in Tm-doped LiNbO₃”, The Photonics Conference 2003 November 12-14, 2003, Jeju, Korea.
 19. *Infrared to blue upconversion in Tm-doped Oxyfluoroborate glasses*
P.Babu, 이선균, Van-Thai Pham, 임기수, 서효진, C.K.Jayasanka
Proceedings of the Optical society of Korea summer meeting 2002, An Myeon-do, July 15-16, 2002.
 20. *Growth of Mn, Ce:LiTaO₃ and two-color holographic recording.*
이선균, Van-Thai Pham, 임기수, 주기태
Proceedings of the Optical society of Korea summer meeting 2002, An Myeon-do, July 15-16

Bibliography

1. J. Franck, E. R., *Trans. Faraday Soc.* **1934**, 30, 120.
2. Rabinowitch, E., *Trans. Faraday Soc.* **1937**, 33, 1225.
3. Platzman R., F. J., *Z. Phys. A* **1954**, 138, 411.
4. Blandamer M., F. M., *Chem. Rev.* **1970**, 70, 59.
5. Fox M.F., H. E., *J. Chem. Soc. Faraday Trans. 1* **1977**, 73, 1003.
6. Markovich G, P. S., Giniger R, Cheshnovsky O., *J. Chem. Phys.* **1994**, 101, 9344.
7. Sheu W.S., L. Y. T., *Chem. Phys. Lett.* **2003**, 374, 620.
8. Weber R, W. B., Schmidt PM, Widdra W, Hertel IV, *J. Phys. Chem. B* **2004**, 108, 4729.
9. Winter B, W. R., Hertel IV, Faubel M, Jungwirth P, *J. Am. Chem. Soc.* **2005**, 127, 7203.
10. W.S. Sheu, P. J. R., *Chem. Phys. Lett.* **1993**, 213, 233.
11. Fox, M. F., *Q. Rev. Chem. Soc.* **1970**, 24, 565.
12. Baltuska A, E. M., Pshenichnikov MS, Wiersma DA., *J. Phys. Chem. A* **1999**, 103, 10065.
13. F. H. Long, X. S., H. Lu, K. B. Eisenthal, *J. Phys. Chem.* **1994**, 98, 7252.
14. J.A. Kloepfer, V. H. V., V.A. Lenchenkov, S.E. Bradforth, *Chem. Phys. Lett.* **1998**, 298, 120.
15. J.A. Kloepfer, V. H. V., V.A. Lenchenkov, A.C. Germaine, S.E. Bradforth, *J. Chem. Phys.* **2000**, 113, 6288.
16. J.A. Kloepfer, V. H. V., V.A. Lenchenkov, X. Chen, S.E. Bradforth, *J. Chem. Phys.* **2002**, 117, 766.
17. D. Borgis, A. S., *J. Chem. Phys.* **1996**, 104, 4776.
18. A. Staib, D. B., *J. Chem. Phys.* **1996**, 104, 9027.
19. H. Iglev, A. T., A. Thaller, I. Buchvarov, T. Fiebig, A. Laubereau, *Chem. Phys. Lett.* **2005**, 403, 198.
20. Lehr L, Z. M., Frischkorn C, Weinkauf R, Neumark DM., *Science* **1999**, 284, 635.
21. M. C. Sauer, R. A. C., I. A. Shkrob, *J. Phys. Chem. A* **2004**, 108, 5490.
22. R. Lian, D. A. O., R. A. Crowell, I. A. Shkrob, X. Chen, S. E. Bradforth, *J. Phys. Chem. A* **2006**, 110, 9071.
23. A. C. Moskun, S. E. B., J. Thøgersen, S. Keiding, *J. Phys. Chem. A* **2006**, 110, 10947.
24. R. M. Lawrence, R. F. K., *J. Chem. Phys.* **1967**, 47, 4758.
25. H. Tanida, I. W., *Bull. Chem. Soc. Jpn.* **2000**, 73, 2747.
26. G. Markovich, R. G., M. Levin, and O. Cheshnovsky, *J. Chem. Phys.* **1991**, 95, 9416.
27. J. E. Enderby, G. W. N., *Water a Comprehensive Treatise*. New York, 1979; Vol. 1.
28. S. Koneshan, J. C. R., R. M. Lynden-Bell, and S. H. Lee, *J. Phys. Chem. B* **1998**, 102, 4193.
29. E. Brodskaya, A. P. L., and A. Laaksonen, *J. Chem. Phys.* **2002**, 116 (18), 7879.
30. B. Hribar, N. T. S., V. Vlachy, and K. A. Dill, *J. Am. Chem. Soc.* **2002**, 124 (41), 12302.
31. J. M. Heuft, E. J. M., *J. Chem. Phys.* **2005**, 123, 094506.
32. Berendsen, H. J. C. G., J. R.; Straatsma, T. P., *J. Phys. Chem.* **1987**, 91, 6269.
33. E. A. Stern, S. M. H., North-Holland: Amsterdam, 1983; Vol. 1, pp 955-1014.
34. Koningsberger, D. C., *X-ray Absorption Principles, Applications, Techniques of EXAFS, SEXAFS and XANES*. Wiley: New York, 1988.
35. J. J. Rehr, R. C. A., *Reviews of Modern Physics* **2000**, 72, 621.
36. Shankar, R., *Principles of Quantum Mechanics*. Plenum Press: New York,, 1994.
37. P. A. Lee, J. B. P., *Phys. Rev. B* **1975**, 11, 2795.

38. P. A. Lee, P. H. C., P. Eisenberger, B. M. Kincaid, *Reviews of Modern Physics* **1981**, 53, 769.
39. Bianconi, A. In *EXAFS and Near-Edge structure*, Proceedings of the International Conference Frascati, Springer: 1983.
40. Bianconi, A., *XANES spectroscopy*. Wiley: New York, 1988.
41. A. Bianconi, S. D., and D. Lublin, *Chem. Phys. Lett.* **1978**, 59, 121.
42. Bianconi, A., *Surface Science* **1980**, 99, 76.
43. al., M. B. e., *Solid State Commun.* **1980**, 35, 355.
44. Stern, E. A., *Phys. Rev. B* **1974**, 10, 3027.
45. al, T. E. W. e., *J. Am. Chem. Soc.* **1997**, 119, 6297.
46. A. H. de Vries, L. H., and R. Broer, *Int. J. Quantum Chem.* **2003**, 91, 57.
47. J. Wong, F. W. L., R. P. Messmer, D. H. Maylotte, *Phys. Rev. B* **1984**, 30, 5596.
48. C. Mande, V. B. S., Chemical Shifts in X-Ray Absorption Spectra. In *Advances in X-Ray Spectroscopy*, Mande, C. B. a. C., Ed. Pergamon Press: New York, 1982; pp 287-301.
49. Kunzl, V., *Collect. Czech. Chem. Comm.* **1932**, 4, 213.
50. Lindgren, I., *Journal of Electron Spectroscopy and Related Phenomena* **2004**, 137-140, 59.
51. Meisel, A., Chemical Shifts and Changes in Shape of X-Ray Emission Lines in Solids. In *Advances in X-Ray Spectroscopy*, Pergamon Press: New York, 1982; pp 302-337.
52. A. Bianconi, E. F., G. Calas, J. Petiau, *Phys. Rev. B* **1985**, 32, 4292.
53. W. Gawelda, V.-T. P., M. Benfatto, Y. Zaushitsyn, M. Kaiser, D. Grolimund, S. L. Johnson, R. Abela, A. Hauser, Ch. Bressler, M. Chergui, *Phys. Rev. Lett.* **2007**, 98, 057401.
54. V. Briois, C. C. D. M., P. Saintavit, C. Brouder, A. M. Flank, *J. Am. Chem. Soc.* **1995**, 117, 1019.
55. V. Briois, P. S., G. J. Long, and F. Grandjean, *Inorganic Chemistry* **2001**, 40, 912.
56. M. Wilke, F. F., P. E. Petit, G. E. Brown, and F. Martin, *American Mineralogist* **2001**, 86, 714.
57. M. Benfatto, P. D. A., S. Della Longa, and N. V. Pavel, *Phys. Rev. B* **2002**, 65, 1742051.
58. al., T. A. F. e., *Phys. Rev. A* **1986**, 34, 1916.
59. H. Nakamatsu, T. M., H. Adachi, *J. Chem. Phys.* **1991**, 95, 3167.
60. F. Sette, J. S., A. P. Hitchcock, *J. Chem. Phys.* **1984**, 81, 4906.
61. F. Sette, J. S., and A. P. Hitchcock, *Chem. Phys. Lett.* **1984**, 110, 517.
62. Stöhr, J., *NEXAFS Spectroscopy*. Springer: Berlin, 1992.
63. Stern, E. A., Theory of EXAFS. In *X-ray Absorption Principles, Applications, Techniques of EXAFS, SEXAFS and XANES*, Wiley: New York, 1988; p 3.
64. D. E. Sayers, E. A. S., and F. W. Lytle, *Phys. Rev. Lett.* **1971**, 27, 1204.
65. al., J. J. L. e., *J. Am. Chem. Soc.* **2000**, 122, 5742.
66. E. A. Stern, D. E. S., F. W. Lytle, *Phys. Rev. B* **1975**, 11, 4836.
67. F. W. Lytle, D. E. S., E. A. Stern, *Phys. Rev. B* **1975**, 11, 4825.
68. L. Campbell, L. H., J. J. Rehr, W. Bardyszewski, *Phys. Rev. B* **2002**, 65.
69. Filipponi, A., *Journal of Physics Condensed Matter* **2001**, 13 (7), R23.
70. Hayes T. M., B. J. B., *J. Phys. C: Solid State Phys.* **1980**, 13, L731.
71. D'Angelo P, D. N. A., Filipponi A, Pavel N V, Roccatano D, *J. Chem. Phys.* **1994**, 100, 985.
72. Palmer B J, P. D. M. a. F. J. L., *J. Phys. Chem.* **1996**, 100, 13393.
73. P. D'Angelo, A. D. N., M. Mangoni, N.V. Pavel, *J. Chem. Phys.* **1996**, 104, 1779.
74. Filipponi, A., *J. Phys.: Condens. Matter* **1994**, 6 (41), 8415.
75. Filipponi, A., Di Cicco, A., *Phys. Rev. B* **1995**, 51, 12322.
76. Di Cicco, A. D., Filipponi, A., *J. Non-Cryst. Solids* **1996**, 205-207 (1), 304.
77. S. I. Zabinsky, J. J. R., A. Ankudinov, R. C. Albers, M. J. Eller, *Phys. Rev. B* **1995**, 52, 2995.
78. J. Mustre, Y. Y., E. A. Stern, and J. J. Rehr, *Phys. Rev. B* **1990**, 42, 10843.
79. Ravel, B., *Journal of Alloys and Compounds* **2005**, 401, 118.
80. G. A. Crosby, R. J. W., D. H. Carstens, *Science* **1970**, 170, 1195.

81. Cowan, R. D. The Theory of Atomic Structure and Spectra. The University of California Berkeley, Berkeley, 1981.
82. Rehr, J. J., Albers, R. C., *Phys. Rev. B* **1990**, *41*, 8139.
83. Beeby, J. L. Proceedings of the Royal Society of London Series A-Mathematical and Physical Sciences, 1967; p 113.
84. P. Lloyd, P. V. S., *Advances in Physics* **1972**, *21*, 69.
85. C. Bernardini, G. F. C., G. Di Giugno, G. Ghigo, R. Querzoli, B. Touschek, Lifetime and beam size in a storage ring. *Physcal Review Letters* **1963**, *10* (9), 407.
86. Margaritondo, G., Synchrotron light in a nutshell. *Surface Review and Letters* **2000**, *7* (4), 379.
87. Krinsky, S., *Fundamentals of hard x-ray synchrotron radiation sources*. John Wiley and Son, Inc.: New York, 2002.
88. Gawelda, W. Time-resolved x-ray absorption spectroscopy of transition metal complexes. Ecole polytechnique fédérale de Lausanne, Lausanne, 2006.
89. A. Lüdeke, M. M., Top-up operation experience at the Swiss Light Source. In *European particle accelerator conference.*, La Villette-Paris, France, 2002.
90. ESRF <http://www.esrf.eu/UsersAndScience/Experiments/TBS/SciSoft/xop2.3>.
91. program, D. f. H. <http://cars9.uchicago.edu/~ravel/software/doc/Athena/html/hephaestus.html>.
92. A. A. Zholents, M. S. Z., Femtosecond x-ray pulses of synchrotron radiation. *Physcal Review Letters* **1996**, *76* (6), 912.
93. Schoenlein, R. W., Generation of femtosecond pulses of synchrotron radiation. *Science* **2000**, *287*, 2237.
94. A. Amir, Y. G., Three-dimensional theory of the free-electron laser. I. Gain and evolution of optical modes. *Physcal Review A* **1986**, *34*, 4809.
95. P. Beaud, et al., *Phys. Rev. Lett.* **2007**, *99*, 174801
96. S. Khan, K. H., T. Kachel, R. Mitzner, T. Quast, Femtosecond Undulator Radiation from Sliced Electron Bunches. *Physcal Review Letters* **2006**, *97*, 074801.
97. Johnson, S. L. Ultrafast x-ray absorption spectroscopy: properties of liquid silicon and carbon. University of California Berkeley, Berkeley, 2002.
98. Taylor, J. R., *An introduction to error analysis the study of uncertainties in physical measurements*. University science books: Mill Valley, 1982.
99. A. Filipponi, A. D. C., and C. R. Natoli, *Phys. Rev. B* **1995**, *52*, 15122.
100. A. Tenderholt, B. H., K. O. Hodgson 13th International Conference On X-Ray Absorption Fine Structure, 2006.
101. W. H. Press, S. A. T., W. T. Vetterling, and B. P. Flannery, Numerical Recipes. Cambridge University: Cambridge, 1992; p 689.
102. Shushin, A. I., *J. Chem. Phys.* **1992**, *97*, 1954.
103. K.H. Schmidt, P. H., D. M. Bartels, *J. Phys. Chem.* **1995**, *99*, 10530.
104. W.-S. Sheu, P. J. R., *J. Phys. Chem.* **1996**, *100*, 1295.
105. C. G. Elles, I. A. S., R. A. Crowell, D. A. Arms, E. C. Landahl, *J. Chem. Phys.* **2008**, *128*, 061102.
106. Ishigure, K., Shiraishi, H., Okuda, H. , *Radiat. Phys. Chem.* **1988**, *32*, 593.
107. Elliot, A. J., *Can. J. Chem.* **1992**, *70*, 1658.
108. L. I. Grossweiner, M. S. M., *J. Phys. Chem.* **1957**, *61*, 1089.
109. Lee, J. Y. B., J.F.; Grossweiner, L.I. , *Photochem. Photobiol.* **1979**, *29*, 867.
110. K.H. Schmidt, D. M. B., *Chem. Phys.* **1995**, *190*, 145.
111. Milosavljevic, B. H. M., O.I. , *J. Phys. Chem.* **1978**, *82*, 1359.
112. Schwarz, H. A. G., P.S., *J. Phys. Chem.* **1977**, *81*, 22.
113. Pepin, C. G., T.; Houde, D.; Jay-Gerin, J.-P., *J. Phys. Chem. A* **1997**, *101*, 4351.

114. Gauduel, Y., *Ultrafast Dynamics of Chemical Systems*. Simon, J. D., Ed.; Kluwer, Ed. Amsterdam, 1994; pp 81-136.
115. Vilchiz, V. H. K., J. A.; Germaine, A. C.; Lenchenkov, V. A.; Bradforth, S. E., *J. Phys. Chem. A* **2001**, *105*, 1711.
116. Keszei, E. M., T. H.; Rossky, P. J., *J. Phys. Chem.* **1995**, *99*, 22.
117. Jou, F.-Y. F., G. R., *Can. J. Chem.* **1979**, *57*, 591.
118. Hart, E. J. A., M., *The Hydrated Electron*. Wiley-Interscience: New York, 1970.
119. Materials, S., *J. Phys. Chem. A* **2004**, *108*, 9105.
120. R. A. Crowell, R. L., I. A. Shkrob, J. Qian, D. A. Oulianov, S. Pommeret, *J. Phys. Chem.* **2004**, *108*, 9105.
121. C. G. Elles, A. E. J., R. A. Crowell, S. E. Bradforth, *J. Chem. Phys.* **2006**, *125*, 044515.
122. N.-G. Park, S.-W. C., S.-K. Kim, K.-H. Choy, *Chem. Mater.* **1996**, *8*, 324.
123. Chen X., Bradforth. S. E., *Annu. Rev. Phys. Chem.* **2008**, *59*, 203.
124. Ch. Bressler, M. C., *Chem. Rev.* **2004**, *104*, 1781.
125. Newville, M. http://xafs.org/Tutorials?action=AttachFile&do=view&target=Newville_Intro.pdf
126. Australian Synchrotron. <http://www.synchrotron.org.au/index.php/about-us/operations/syn-light-source>
127. Winick, H., *Synchrotron radiation sources: a primer*. World science: Vol. 1.
128. B. Kalantari, V. S., T. Korhonen In *Bunch pattern control in top-up mode at the swiss light source*, Proceedings of EPAC 2004, Lucerne, Switzerland, Lucerne, Switzerland, 2004.
129. G. Ingold, P. B., S. Johnson, A. Streun, T. Schmidt, R. Abela, A. Al-Adwan, D. Abramsohn, M. Böge, D. Grolimund, A. Keller, F. Krasniqi, L. Rivkin, M. Rohrer, T. Schilcher, T. Schmidt, V. Schlott, L. Schulz, F. van der Veen, D. Zimoch, *AIP Conf. Proc.* **2007**, *879*, 1198.
130. U.S. department of commerce and National bureau of standards, *Optical spectra of nonmetallic inorganic transient species in aqueous solution*.
131. P. D'Angelo, *Private Communication*.
132. M. F. Kropman, H. J. Bakker, *Science* **2001**, *291*, 2118.